Intrinsic decoherence in superconducting quantum circuits

Zur Erlangung des akademischen Grades eines

DOKTORS DER NATURWISSENSCHAFTEN (DR. RER. NAT.)

von der KIT-Fakultät für Physik des
Karlsruher Instituts für Technologie (KIT)

genehmigte

Dissertation

von

M.Sc. Steffen Schlör

Tag der mündlichen Prüfung:	20. Dezember 2019
Referent:	Prof. Dr. Alexey V. Ustinov
Korreferent:	Prof. Dr. Martin Weides

Abstract

Decoherence and parameter fluctuations are two of the mayor obstacles for solid-state quantum computing. In this work, decoherence in superconducting qubits of the transmon type is investigated. For this purpose, a time-multiplexed measurement protocol was developed and applied in long-term measurements. The resulting simultaneous measurement of the qubit's relaxation and dephasing rate, as well as its resonance frequency enables analysis of correlations between these parameters. A spectral noise analysis complements these measurements. Together, the results agree well with the interacting defect model of two-level-systems [1] and yield information about the microscopic origin of the intrinsic decoherence mechanisms in Josephson qubits.

Our measurements show inherent correlations between dephasing and fluctuations in qubit frequency on the timescale of seconds to days, which is attributed to the influence of individual defects, located close to conductor edges. Cross-correlation and spectral noise analysis confirm this interpretation and ascribe the source of fluctuation to interactions between thermal fluctuators and surface defects. Single defects reducing the coherence of qubits by up to one order of magnitude are a major challenge for future quantum computers.

Non-tunable qubits are intrinsically insensitive to some decoherence channels and thus ideal for this fundamental analysis. However, to widen the focus and contrast the results of different material systems, we pursue the fabrication of voltage controlled gatemon qubits. In the course of this work, the theoretical foundation and technical implementation of transmon qubits based on regular Josephson weak links, and semiconducting nanowires is given. The experimental design and measurement setup are explained in detail.

Our findings make continuous re-calibration a necessity in today's solid-state qubits, although new materials or processing techniques might mitigate the problem. However, the results of this work imply that fundamental improvements of qubit parameter stability are necessary in order to realize scalable and coherent qubit circuits.

Contents

1 Introduction

Few inventions in the history of mankind had an impact on our everyday lives, as large as the computer. Its basic building blocks, that realize Alan Turing's idea of an abstract computational machine [2], are simple electrical switches. The creators of the first transistor and its field-effect counterpart [3] did presumably never imagine, that billions of their inventions are carried around in the form of smartphones today.

At first, the possibility to control a current with a smaller one or a gate voltage may seem inconspicuous. However, the ensuing digital revolution led to the evolution of production and business techniques, harnessing an exponential growth of information storage and transmission. It opened the field of computational simulation, which is now an integral part of the scientific method and an active field of research. Today, mathematical modeling and simulation of more and more realistic and thus complex aspects of nature are possible:

Today's supercomputers are capable of approximating molecular dynamics of ribosomes [4] or the behavior of black holes [5]. However, accurate predictions on the dynamics of even smaller molecules' dynamics are currently intractable on classical computers. The reason lies in the quantum mechanical nature of the problem, the computational cost grows exponentially with the dimension of the related Hilbert space [6]. A potential solution to this fundamental problem was formulated by Richard Feynman. He proposed to use a 'universal quantum simulator', which itself behaves quantum mechanically [7]. Such a machine may theoretically satisfy the Church–Turing–Deutsch principle, stating that every physical process can be simulated by a universal computing device [8]. The benefit of a universal quantum computer would be tremendous. Its applications include quantum chemistry [9], for instance in the design of drugs or the development of enhanced chemical processes in fertilizer production. Further, Shor's factoring algorithm is exponentially faster than any known classical procedure at factorization into prime numbers [10], which underlies much of modern cryptography, such as RSA encryption. Quantum systems have the intriguing ability to exist in a superposition of several states, which has no classical analog. For quantum memory, this results in so-called quantum parallelism, the possibility to perform operations on several states at once. Grover's search method uses this feature and provides a speed-up to the ubiquitous procedure of searching an unsorted database [11].

In regard of these traits it is not surprising that large computing companies put great efforts into building a quantum processor, to unlock new computational territory. Despite extensive investments, in both cost and time, the innovative concept of a universal quantum processor still remains fictional. The problem lies in the conflicting demands of a highly isolated quantum system on one side, and fast manipulation and readout on the other. Industrial and academic research strive to find a hardware platform that renders fault tolerant quantum computation possible [12, 13]. Currently, the most promising candidates are, trapped ions [14], nitrogen-vacancy center in diamond [15], and superconducting solid-state qubits [16]. Today's state of the art quantum circuits may be considered 'noisy intermediate-scale quantum' devices [17]. These systems can already be used to study fundamental quantum mechanics such as the quantum zeno effect [18]. In a recently published work, Google demonstrated the quantum supremacy of a 53 qubit processor over a classical supercomputer in a cross-entropy benchmark - however, only at a task tailored to the strengths of their device [19]. Ultimately, the fidelity of two-qubit gates, on-chip crosstalk, and parameter fluctuations [20–22] are still problems, that are limiting present-day quantum circuits. Just like the transistor, the fabrication of a quantum bit, suitable as basic building block for a scalable quantum computer, would be game-changing.

In this work, we focus on superconducting qubits and the factors limiting their implementation in the form of a quantum computer. An intuitive metric in this regard is the ratio between coherence time and the operation, or gate time of a qubit. Today's multi qubit chips, based on the so-called 'transmon' [23] architecture are already capable of finding the electronic ground state of small molecules [24]. However, the error probability due to random parameter fluctuations scales exponentially with the number of qubits, rendering the calibration of many-qubit systems difficult. The demand on stability and coherence of scaled-up quantum systems widens the focus of current research towards new decoherence mechanisms and qubit parameter stability on the time scale of seconds to days.

In this work we investigate the time-stability of a highly coherent fixed-frequency transmon qubit. These devices belongs to the least sensitive of today's superconducting qubits, regarding external noise. For this purpose we devise a time-multiplexed measurement protocol, which allows us to acquire all qubit parameters simultaneously. Further, we present our recent progress toward building voltage controlled transmon qubits, based on semiconducting nanowires. Their strongly localized gate effect could mitigate scaling challenges, by reducing inter-qubit crosstalk.

Here, we discuss our observation of strong fluctuations in the qubit's relaxation and dephasing rate, as well as its resonance frequency. Correlation analysis reveals a connection between noise at mHz frequencies and qubit dephasing. We attribute our findings to spurious two-level-systems and locate them close to edges of the superconducting films.

These defects constitute an intrinsic noise source in many microscopic circuits and call the feasibility of coherent many-qubit systems into question.

In this thesis, I first introduce the general concept of qubits and their dynamics. In the following, the principles of superconductivity and the physical implementation of our qubits are discussed. Further, microwave circuits, and the basics of manipulation and readout of transmon qubits are presented. The subsequent chapter briefly introduces the physics of semiconducting nanowires and explains our fabrication method. In the next chapter, the experimental setup, including the cryostat, the microwave electronics, the sample design, and the measurement procedure are presented. Thereafter, the experimental results and derived noise model are discussed. Finally, I summarize the results and conclude with possible future experiments, and suggestions to mitigate or exploit the observed effects.

2 Superconducting Quantum Devices

In this chapter, the main building blocks for superconducting quantum circuits are introduced, providing the basis for the following discussion of decoherence and parameter fluctuation in superconducting quantum bits. Analogous to the transistor in classical microprocessors, the fundamental active element of quantum circuits is the qubit. In the following, the quantum mechanical description of qubits, and their dynamics are discussed. Two-level-systems, which play an important part in the qubits decoherence, are introduced. The manipulation of a qubit state, necessary for quantum information processing is discussed and visualized. Further, the basic concepts of superconductivity and the related Josephson effect, which provides the basis for most quantum circuits, are described. Finally, two physical qubit implementations, the "transmon" and the "gatemon" are discussed.

2.1 Bits and Quantum Bits

The bit, short for "binary digit" is the commonly used unit of information in computing and digital communication. One bit carries the information of a single fair coin toss, or the answer to a "yes" or "no" question. The maximum amount of information a system with N possible states can contain is proportional to $\log_b N$. For bits, b is 2, but it is possible to use different bases to encode and measure information, e.g. $b = 3$ is called a "trit". The most dense information medium known to mankind is our own DNA [25], which uses a base $b = 4$.

The reason for the predominant use of bits as computational basis in today's computers is its physical implementation. A bit can be represented by any system that exhibits two distinct states. Over time, many different realizations emerged, e.g. holes in the paper of punch cards, the direction of magnetization in hard discs or magnetic tape, the two stable states of a latching circuit or simply the state of an electric switch. Today, complementary metal–oxide–semiconductor (CMOS) technology is used in most

microprocessors, intrinsically providing two stable states with about 171 million transistors per square millimeter as of 2019.

These classical Turing machines provide the basis for virtually all computing today. The demand for efficient simulation of quantum mechanical systems, however, drives the development of a quantum mechanical analog to the Turing machine [26]. As stated in the introduction, a universal quantum computer may be able to solve important problems intractable for its classical counterpart [9].

2.2 Qubits and the Bloch Sphere Representation

As with classical bits, any quantum mechanical two-level system may be used as a quantum bit or "qubit". And likewise, the physical implementation can vary greatly. Natural examples are the spin of a spin-1/2 particle like the electron, or the polarization of a single photon. It is common, to use two distinct states of a more complex quantum system featuring many states, if the states in question are isolated enough to approximate a two-level system. Possible physical realizations are discussed in section 2.8.

When measured, both bit and qubit give one of two values, usually called "0" and "1". The crucial difference is, that the state $|\psi\rangle$ of a qubit prior to measurement is described by a coherent superposition of its energy eigenstates $|0\rangle$ and $|1\rangle$[1] as

$$|\psi\rangle = \alpha\,|0\rangle + \beta\,|1\rangle\,. \tag{2.1}$$

The complex coefficients α and β satisfy $|\alpha|^2 + |\beta|^2 = 1$ for normalization, the equation of a circle. If we also consider the relative phase degree of freedom, it is intuitive to represent all possible pure states as the surface of a sphere, the so-called Bloch-sphere [27]. Qubit states are now accurately described by the two Euler angles [28] θ and ϕ (see Fig.2.1)

$$|\psi\rangle = e^{i\xi}\cos\left(\frac{\theta}{2}\right)|0\rangle + e^{i(\xi+\phi)}\sin\left(\frac{\theta}{2}\right)|1\rangle\,. \tag{2.2}$$

The last degree of freedom, the global phase factor $e^{i\xi}$ of the qubit state, has no physical meaning and can thus be chosen to be $\xi = 0$. We can understand the computational basis $|0\rangle$ and $|1\rangle$ as eigenvectors to the Pauli matrix σ_z,

$$|0\rangle = \begin{pmatrix} 0 \\ 1 \end{pmatrix}, \qquad |1\rangle = \begin{pmatrix} 1 \\ 0 \end{pmatrix} \tag{2.3}$$

[1] The notation $|0\rangle$, $|1\rangle$ is synonymous with $|g\rangle$, $|e\rangle$ or $|\downarrow\rangle$ and $|\uparrow\rangle$ and may change to avoid confusion with excitation numbers $|n\rangle$

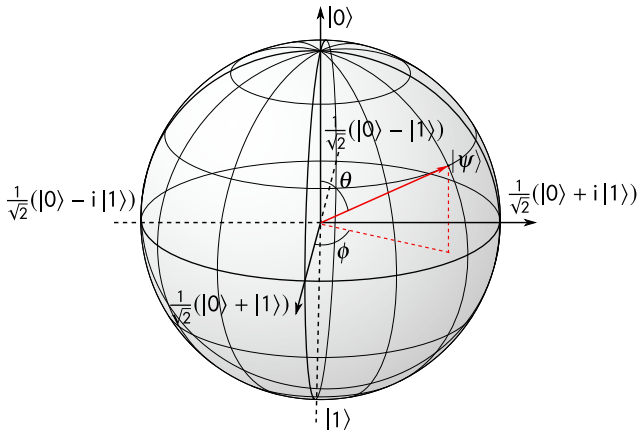

Figure 2.1: Bloch sphere representation of a qubit state. North and south pole denote ground and excited state of the qubit, while any other point on the sphere describes a superposition of these states. An arbitrary state $|\psi\rangle$ can be described by the polar angle θ and azimuthal angle ϕ. Mean values of ensembles of qubits or mixed states in general are visualized as Bloch vectors inside the sphere.

In contrast to the classical bit, measuring the state of a qubit collapses the coherent superposition onto one of its eigenstates $\sigma_z|0\rangle = -1|0\rangle$ or $\sigma_z|1\rangle = +1|1\rangle$ and thus generally changes the state. The probability to collapse into the $|0\rangle$ ($|1\rangle$) state is given by $|\alpha|^2$ ($|\beta|^2$), respectively. In experiments it is often necessary to repeat a measurement many times in order to extract a meaningful result. This is deeply rooted in the probabilistic nature of projective measurements but also used to increase the signal-to-noise ratio. This statistical ensemble of measurements, referred to as a mixed state can also be represented by the Bloch-sphere. Mixed states are non-unitary vectors inside the sphere, with coordinates describing the corresponding ensemble averages. They can be expressed by the density operator $\hat{\rho}$ also called density matrix

$$\hat{\rho} = \sum_j p_j |\psi_j\rangle \langle\psi_j|, \tag{2.4}$$

with the probability p_j to find the ensemble in the respective pure state $|\psi_j\rangle$ [29]. The probability distribution may either represent an ensemble of similar two-level systems, or an ensemble of identically prepared measurements of a single qubit. The corresponding expectation value along the axis k is given by $\langle\sigma_k\rangle = \mathrm{tr}(\hat{\rho}\sigma_k)$.

2.3 Qubit Dynamics and Decoherence

The time evolution of an isolated pure qubit state as stated in Eq. (2.2) is given by

$$|\psi(t)\rangle = \exp\left(\frac{-i\hat{H}(t-t_0)}{\hbar}\right)|\psi(t_0)\rangle \tag{2.5}$$

with the time-independent Hamiltonian of the system

$$\hat{H} = \hbar\frac{\omega_\mathrm{q}}{2}\sigma_z \tag{2.6}$$

it follows

$$|\psi(t)\rangle = \cos\left(\frac{\theta}{2}\right)|0\rangle + e^{i(\phi-\omega_\mathrm{q}t)}\sin\left(\frac{\theta}{2}\right)|1\rangle\,, \tag{2.7}$$

describing a rotation of the Bloch vector around the z-axis at the angular frequency ω_q. In the representation of the qubit state, this precession is often neglected, implicitly referring to a rotating frame of the same angular velocity ω_q. In this frame, the Bloch vector is resting.

In any physical implementation there will be some form of interaction with the environment and thus decoherence. It is therefore important, to describe the time evolution of a mixed state in order to predict the dynamics of any real qubit, which is subject to decoherence. In general this is done by the von Neumann equation

$$\frac{\partial}{\partial t}\hat{\rho} = -\frac{i}{\hbar}\left[\hat{H},\hat{\rho}\right]. \tag{2.8}$$

To incorporate the dissipative environment, one would need to know the Hamiltonian and density operator of the complete system consisting of qubit and environment. This approach is not feasible due to the (usually infinite) size of the related Hilbert space. However, this problem can be mitigated by explicitly adding a dissipation term for incoherent interactions with the environment. The resulting equation for the time evolution of the density operator $\hat{\rho}$ is the so-called Lindblad master equation [30, 31] (in diagonal form)

$$\frac{\mathrm{d}}{\mathrm{d}t}\hat{\rho} = -\frac{i}{\hbar}\left[\hat{H},\hat{\rho}\right] + \sum_{k=1}\Gamma_k\left(\hat{L}_k^\dagger\hat{\rho}\hat{L}_k - \frac{1}{2}\left\{\hat{L}_k^\dagger\hat{L}_k,\hat{\rho}\right\}\right). \tag{2.9}$$

With the anticommutator $\{a,b\} = ab + ba$, the orthonormal Lindblad or jump operators $\hat{L}_k$ describing the exchange of single quanta with the environment, and the respective interaction rate Γ_k for decoherence channel "k" [32].

For our case, the possible decoherence channels are energy relaxation, namely loosing the qubit excitation to the environment, and dephasing resulting from changes in the splitting energy ω_q. Energy relaxation is encoded in the operator $\hat{L}_1 = 1/2(\hat{\sigma}_x - i\hat{\sigma}_y) = \hat{\sigma}_-$, with

the Pauli operators $\hat{\sigma}_x$ and $\hat{\sigma}_y$ and the corresponding transition rate Γ_1. The dephasing is represented by $\hat{L}_2 = \hat{\sigma}_z/\sqrt{2}$, with the rate Γ_2 called pure dephasing rate or Γ_ϕ.

The third part of the sum $k = 3$ contains the excitation of the qubit by the environment, which is thermally suppressed by the Boltzmann factor $\exp(-\hbar\omega_\mathrm{q}/k_\mathrm{B}T)$. Thus the thermal excitation is on the order of 10^{-7} for our experiments[2] and can theoretically be neglected. However, measurements usually show a residual excited-state population on the order of few percent. Therefore we sometimes refer to swaps between $|0\rangle$ and $|1\rangle$ as state inversion.

Since the definition of the density operator ensures $\mathrm{tr}\hat{\rho} = 1$, the density matrix of our system can be written as

$$\hat{\rho} = \begin{pmatrix} \rho_{00} & \rho_{01} \\ \rho_{10}^* & 1-\rho_{00} \end{pmatrix}. \tag{2.10}$$

Inserting into the Lindblad equation (2.9) yields

$$\frac{\mathrm{d}}{\mathrm{d}t}\begin{pmatrix} \rho_{00} & \rho_{01} \\ \rho_{10}^* & 1-\rho_{00} \end{pmatrix} = -\frac{i}{\hbar}\left[\hat{H},\hat{\rho}\right] + \begin{pmatrix} -\Gamma_1\rho_{00} & -(\Gamma_1/2+\Gamma_\phi)\rho_{01} \\ -(\Gamma_1/2+\Gamma_\phi)\rho_{10}^* & \Gamma_1\rho_{11} \end{pmatrix}, \tag{2.11}$$

the off-diagonal rates are also abbreviated as $-\Gamma_2$ with

$$\Gamma_2 = \frac{1}{T_2} = \frac{\Gamma_1}{2} + \Gamma_\phi. \tag{2.12}$$

This already indicates that without pure dephasing ($\Gamma_\phi = 0$), the dephasing rate is limited by relaxation

$$T_2^* = \frac{1}{\Gamma_2} = \frac{2}{\Gamma_1} = 2T_1. \tag{2.13}$$

We can now incorporate the energy relaxation and dephasing into the qubit time evolution. As the Bloch vector is constantly evolving around the z-axis, it is useful to transform the Hamiltonian (2.6) into the precessing frame with angular velocity ω_f.

$$\hat{H}_\mathrm{rot} = \hbar\frac{\omega_\mathrm{q}-\omega_\mathrm{f}}{2}\sigma_z = \hbar\frac{\Delta\omega}{2}\sigma_z \tag{2.14}$$

the time evolution of the density matrix can be derived from Eq. (2.11) as

$$\hat{\rho}(t) = \begin{pmatrix} a_0 e^{-\Gamma_1 t} & a_1 e^{-\Gamma_2 t} e^{-i\Delta\omega t} \\ a_1^* e^{-\Gamma_2 t} e^{i\Delta\omega t} & 1-a_0 e^{-\Gamma_1 t} \end{pmatrix} \tag{2.15}$$

with the frequency shift $\Delta\omega$ between the rotating frame and the qubit frequency and the integration constants $a_{0,1}$. We can directly see that the qubit state for large times $\Gamma t \gg 1$,

[2] The usual sample temperature is below 20 mK and typical qubit frequencies are 5–10 GHz

the system will be in the ground state $|0\rangle$ with $\rho_{11} = 1$. If the initial state is $|1\rangle$ ($\rho_{00} = 1$), it decays at the rate Γ_1 to the ground state. In addition, for a state on the equator, the phase oscillates at the frequency $\Delta\omega$ while decaying at the rate Γ_2, these oscillations are called Ramsey fringes. For a rotating frame in sync with the qubit frequency $\Delta\omega = 0$, the phase angle ϕ of the Bloch vector should be stationary. For a real qubit however, the qubit frequency constantly changes and thus the phase evolution $\phi(t) = \omega_q(t)t$ changes over time. If we average over an ensemble of Bloch vectors, some of which rotate faster, others slower, the length of the averaged Bloch vector decreases. This is called pure dephasing, see Fig. 2.3(f) in Sec. 2.6 for an illustration of the different single states (blue) and the ensemble average (red).

In a projective measurement we can only access the state with respect to the quantization axis. In order to measure the dephasing and energy relaxation rates of the qubit in question, we need to be able to change its state in a predictable manner, as shown in Fig. 2.3. This is done by an external electromagnetic drive using defined pulses. The dynamics of a qubit in the presence of an external drive is subject of section 2.5. Commonly used techniques of decoherence measurements are discussed in section 5.2.3.

2.4 Two-Level-Systems (TLS)

Besides extrinsic effects leading to dephasing and relaxation, like coupling to electromagnetic fields or variation in temperature, also local decoherence channels exist. One of these loss channels are microscopic defects in the amorphous parts of the quantum circuit, manifesting as two-levels-systems.

TLS are believed to be responsible for the almost universal anomalous low temperature behavior of glasses, displaying a linear, temperature-dependent term in the specific heat below about 1 K [33]. This observation can be explained in terms of the so-called standard tunneling model (STM) [33–35], which assumes TLS to have two distinct energy states modeled by a double-well potential when limited to low energies. Illustrations of the related potential and common TLS configurations are shown in Fig. 2.2, based on the extensive review of Müller *et al.* [1].

Qubits which are well protected from the surrounding electromagnetic spectrum, and other external influences, as for example in 3D cavities, show a great reduction in radiative decay and dephasing induced by external fields [36]. For such highly coherent qubits, the influence of microscopic TLS in the circuit materials may become the dominant decoherence mechanism, as is discussed in chapter 6. There are several candidates for these elusive defects, such as tunneling atoms, hydrogen rotors or dangling bonds.

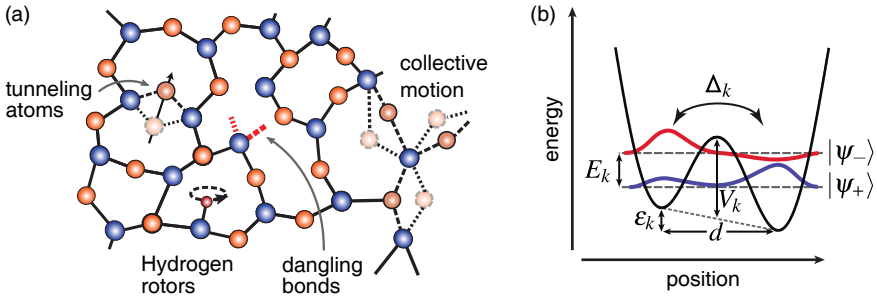

Figure 2.2: (a) Illustration of different candidates for microscopic two-level-systems in an amorphous material, like the insulating layer in a Josephson junction. Those are atoms tunneling between different sites, collective motion of atomic groups, dangling bonds and hydrogen defects. (b) Generic double-well potential modeling the eigenstates $|\psi_\pm\rangle$ of TLS$_k$ in real space. The difference between the energy eigenstates is E_k the tunneling rate between the wells is Δ_k and the asymmetry energy is ε_k. Both illustrations are based on [1].

While the nature of TLS is still a matter of debate, they can be described by a model Hamiltonian for a particle of effective mass m in an asymmetric double well potential of two identical wells, shifted in space and energy. For a single TLS with index k, its Hamiltonian is

$$\hat{H}_{\mathrm{TLS},k} = \frac{\hbar}{2}\begin{pmatrix} \varepsilon_k & \Delta_k \\ \Delta_k & -\varepsilon_k \end{pmatrix} = \frac{\hbar}{2}(\varepsilon_k \sigma_\mathrm{z} + \Delta_k \sigma_\mathrm{x}), \tag{2.16}$$

with the energy difference between the lower and the higher state $\hbar\varepsilon_k$ and the coupling energy $\hbar\Delta_k$. The coupling energy can be approximated to arise from the overlap of two harmonic potential wells, even if the exact shape of the potential is uncertain in amorphous materials. The coupling energy depends exponentially on the barrier height V_k and the distance d, see Fig. 2.2(b)

$$\Delta_k = \omega_{0,k} e^{-\lambda_k}, \tag{2.17}$$

with the tunneling parameter

$$\lambda_k = \sqrt{\frac{2mV_k}{\hbar^2}}d. \tag{2.18}$$

Here, $\omega_{0,k}$ is approximately the mean oscillation frequency of both wells [35]. Further the STM assumes that TLS couple to electric or strain fields such that transitions between the states can be driven. The asymmetry energy and barrier heights are assumed to be independent and uniformly distributed, causing the related tunneling rate to follow a log uniform distribution. This assumption can be intuitively motivated by the broad distribution of asymmetry energies up to the glass transition temperature on the order of 1000 K. Thus,

we can expect the distribution $P(\varepsilon_k, \lambda_k)\mathrm{d}\varepsilon\mathrm{d}\lambda = P_0\mathrm{d}\varepsilon\mathrm{d}\lambda$, where P_0 is a constant. Thus, the distribution of TLS can be expressed as

$$P(E,\Delta)\,\mathrm{d}\Delta\mathrm{d}E = P_0\frac{E}{\Delta\sqrt{E^2-\Delta^2}}\,\mathrm{d}\Delta\mathrm{d}E. \tag{2.19}$$

Integration over Δ_k yields the density of states (DOS)

$$D(E) = \int_{\Delta_{\min}}^{E} P(E,\Delta)\,\mathrm{d}\Delta = P_0\ln\left(\frac{2E}{\Delta_{\min}}\right) \approx D_0, \tag{2.20}$$

which is usually approximated as constant over the relevant energy range. Here, $\Delta_{\min}$ is the low energy cutoff, where the tunneling probability becomes negligible on the relevant experimental timescale. An ensemble of TLS with homogeneous distributed tunneling parameters produces noise of the spectral form $1/f^{\alpha}$ with $\alpha \approx 1$, which is almost omnipresent in physical systems [37]. For high frequencies $hf \gg k_{\mathrm{B}}T$ however, Johnson-Nyquist noise is usually proportional to f^{α}. Shnirman *et al.* [38] showed that a distribution of the form

$$P(\varepsilon_k, \Delta_k) \propto (\varepsilon/\Delta_k)^s \tag{2.21}$$

with $-1 \leq s \leq 1$ leads to a noise spectral density satisfying both limits $S \propto 1/f$, and $S \propto f$ for energies below, and above $k_{\mathrm{B}}T$, respectively.

In the position basis, the lowest eigenstates corresponding to the left ($|L\rangle$) and right ($|R\rangle$) well hybridize. The resulting eigenstates are analogous to the Euler angle description of a qubit (Eq. 2.2)

$$|\psi_+\rangle = \sin\left(\frac{\theta}{2}\right)|L\rangle + \cos\left(\frac{\theta}{2}\right)|R\rangle, \tag{2.22}$$

$$|\psi_-\rangle = \cos\left(\frac{\theta}{2}\right)|L\rangle - \sin\left(\frac{\theta}{2}\right)|R\rangle, \tag{2.23}$$

with the mixing angle

$$\theta_k = \arctan(\Delta_k/\varepsilon_k). \tag{2.24}$$

The energy difference between the states $|\psi_\pm\rangle$ is

$$E_k = E_- - E_+ = \sqrt{\Delta_k^2 + \varepsilon_k^2}. \tag{2.25}$$

TLS may couple by their electric dipole moment to a qubit's oscillating electric fields which periodically vary the TLS asymmetry ε_k, while the intrinsic tunneling energy remains constant. Naturally, the dipole moment can be expressed as eigenvalue of the position basis $\{|L\rangle, |R\rangle\}$. Thus, the interaction with an electric field can be written as

$$\hat{H}_{\mathrm{int}} = \sigma_z\frac{\partial\varepsilon_k}{2\partial|\vec{E}|}\vec{E} = \sigma_z\vec{d}_k\vec{E}, \tag{2.26}$$

with the electric field $\vec{E}$ and the dipole moment $\vec{d}_k$. In the eigenbasis of the TLS $\{|\psi_+\rangle, |\psi_-\rangle\}$, the interaction between a qubit and a TLS is

$$\hat{H}'_{\text{int}} = g_k(\cos(\theta_k)\sigma_z - \sin(\theta_k)\sigma_x) \tag{2.27}$$

with the mixing angle θ_k, Eq. (2.24) and the coupling constant g_k. The cosine and sine terms in Eq. (2.27) stand for variation in the energy levels, and energy exchange, respectively. These diagonal and off-diagonal entries in the coupling operator are generally referred to as longitudinal and transversal. In the language of qubit coherence, the transversal component induces state transitions and accounts for relaxation, while the longitudinal term produces dephasing.

Following ref. [38], the relevant spectral components of TLS are separated into three terms

$$\begin{aligned} S_k(\omega) = &\cos^2\theta_k(1-\langle\sigma_z\rangle^2)\,\frac{2\gamma_{1,k}}{\gamma_{1,k}^2+\omega^2} \\ &+\sin^2\theta_k\left(\frac{1+\langle\sigma_z\rangle^2}{2}\right)\frac{2\gamma_{2,k}}{\gamma_{2,k}^2+(\omega-E_k)^2} \\ &+\sin^2\theta_k\left(\frac{1-\langle\sigma_z\rangle^2}{2}\right)\frac{2\gamma_{2,k}}{\gamma_{2,k}^2+(\omega+E_k)^2}, \end{aligned} \tag{2.28}$$

with the thermal equilibrium population of $\langle\sigma_z\rangle = \tanh(E_k/2k_BT)$, and the TLS' intrinsic relaxation and dephasing rates $\gamma_{1,k}$ and $\gamma_{2,k}$. The three terms in Eq. (2.28) represent Lorentzian distributions around zero and $\pm E_k$. The latter two can be interpreted as emission and absorption, swapping the TLS state. For typical qubit experiments these energies are high compared to the thermal level. In this case, the excitation by high frequency TLS ($\omega = -E_k$) is suppressed by the Boltzmann factor and can usually be neglected. The absorption by TLS close to the qubit frequency ($\omega_q \approx E_k$) can be a relevant photon loss channel, as discussed in Sec. 6.1.

The longitudinal term centered around zero frequency describes random switching of a thermally excited TLS with $E_k \lesssim k_BT$, also called two-level fluctuators (TLF). TLS may also interact with each other via their dipole moments, or their response to mechanical strain [39, 40]. Coherent TLS-TLS interaction was first observed in our group by Lisenfeld *et al.* [40]. We assume fluctuations by TLF, mediated by their coupling to other TLS, to be the indirect source of spectral diffusion in qubit frequencies observed during this work (see Ch.6 for details).

2.5 Driven Qubit

If a two-level system exchanges energy with an external oscillation field, it has to change its projection onto the quantization axis. Under a resonant drive it will oscillate between $|0\rangle$ and$|1\rangle$. These coherent oscillations are called Rabi oscillations. This behavior differs from harmonic oscillators and is therefore a useful test, to distinguish qubits from other microwave modes in the system. Further, we use the measured period of Rabi oscillations to calibrate the amplitude of the used microwave drives and gauge our qubit gates, see Sec. 2.6. The Hamiltonian of a qubit transversally coupled to an oscillating electromagnetic field is given by

$$\hat{H} = \hbar\frac{\omega_\mathrm{q}}{2}\sigma_z + \hbar\Omega_0\sigma_x\cos(\omega_\mathrm{d}t) \tag{2.29}$$

with the drive of frequency ω_d and amplitude Ω_0, given as a rate of incoming photons, which is also the Rabi frequency for the assumed coupling σ_x. In the rotating frame of the drive, the Hamiltonian transforms to

$$\hat{H}_\mathrm{rot} = \hbar\frac{\omega_\mathrm{q}-\omega_\mathrm{d}}{2}\sigma_z + \hbar\frac{\Omega_0}{2}\sigma_x, \tag{2.30}$$

which can be diagonalized to obtain the eigenenergies

$$E_\pm = \pm\frac{1}{2}\sqrt{\Omega_0^2+\Delta\omega^2} = \pm\frac{1}{2}\Omega. \tag{2.31}$$

Here $\Delta\omega$ is the detuning between drive and qubit frequency and Ω is the generalized Rabi frequency in the presence of detuning $\Delta\omega \neq 0$, defined as $\Omega = \sqrt{\Omega_0^2+\Delta\omega^2}$. With increasing detuning, the corresponding rotation axis moves out of the xy-plane, resulting in a coherent oscillation between $|0\rangle$ and $(1-\alpha)|0\rangle + \alpha|1\rangle$ with

$$\alpha = \left(\frac{\Delta\omega}{\sqrt{\Omega_0^2+\Delta\omega^2}}\right)^2. \tag{2.32}$$

For example, if the drive is detuned by the Rabi frequency Ω_0, the rotation axis is tilted $\theta = 45^\circ$ and the largest probability to measure the excited state is $p(|1\rangle)_\mathrm{max} = 0.5$.

2.6 Qubit Control

In the previous section, Rabi oscillations in the presence of a drive field are discussed. It is possible to stop the drive in midst of the Rabi cycle to obtain a probability distribution according to the last orientation of the Bloch vector. This technique is used for all deliberate rotations of the qubit state changing θ. In conjunction with phase rotations, for example by changing the drive frequency ω_q, full control of the qubit state is obtained. The microwave tones used for qubit manipulation are referred to as "gates" or "pulses". To extract the current state of the qubit means to perform a projective measurement on the quantization axis. Information about the probability distribution along other directions is obtained by fast rotations of the axis in question onto the quantization axis and subsequent measurement. Fast, in this context, means that the pulse length is short compared to the respective decoherence times T_2^* and T_1.

In general, the smallest possible error per gate (EPG) is given by the ratio between gate time and coherence time. Thus, short gate pulses are desirable to reduce the EPG, which is crucial to enable successful quantum computing. However, as shorter pulses have larger bandwidth and many physical qubit implementations have more than the two levels used as computational basis, shorter pulses may lead to the excitation of higher states outside the computational subspace. This effect is also called state leakage [41]. It is therefore important to limit the bandwidth of gate pulses. The simplest form, a square wave envelope, as e.g. provided by a simple microwave switch, contains odd harmonics of frequencies only limited by the systems bandwidth and is obviously not ideal.
One solution to this problem is to create a pulse that has a narrow bandwidth but the same effect on the qubit, by changing its envelope. This technique is called "pulse shaping". By using derivative reduction by adiabatic gate (DRAG) pulses [42], over 99.9 % of single qubit gate fidelity have been achieved on superconducting devices [13]. Detuning the pulse to counteract the AC-Stark shift caused by large drive amplitudes can further increase the gate fidelity for short pulses [43].

When creating optimized gate pulses, it is important to account for experimental imperfections e.g. the non-uniform transfer function of the microwave line. This can be done, by means of optimal control theory [44], optimizing pulse shapes with various methods [45, 46] until a threshold gate fidelity is reached. Another possibility is using the qubit's Rabi oscillation as reference, effectively measuring the transfer function in the accessible frequency range [47]. Unless noted otherwise, we used Gaussian envelopes, which provide a sufficient protection against state leakage for the gate times used in this work, which are usually on the order of 100 ns.

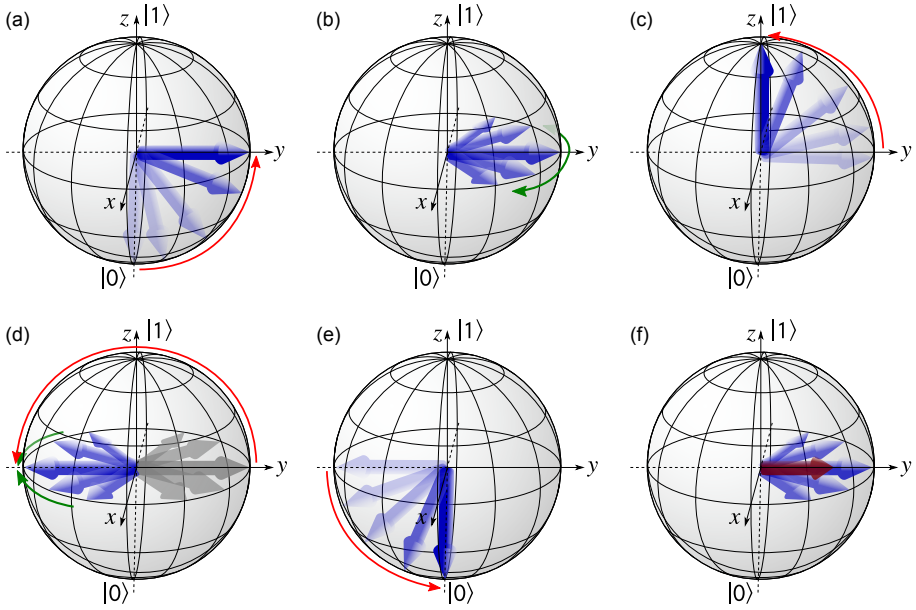

Figure 2.3: Visualization of the qubit state evolution in the rotating frame for different microwave pulses and free evolution. The upper row (a-c) illustrates a Ramsey sequence, consisting of two $(\pi/2)_x$ pulses (a,c), separated by the free evolution (b). The pulses are usually slightly detuned, to cause a beating in the signal called Ramsey fringes, which enable the extraction of the qubit frequency. Insertion of a $\pm\pi_x$ (or $\pm\pi_y$) pulse (d) in the middle of the free evolution, creates a spin-echo sequence (a,b,d,e). Spin-echo can re-align phase drifts with correlation times longer than $1/\Delta t$. In (f), the effective shrinking of the Bloch vector due to averaging over an ensemble of states with different phase is illustrated. For simplicity, we choose the $|1\rangle$ state to point in the positive z-direction.

In order to measure the coherence of a qubit, or manipulate its state, we need to define the necessary gate pulses. This is done by means of a Rabi measurement: A microwave tone at the qubit frequency is synthesized to create pulses of increasing length that cause Rabi oscillations. For every pulse length, the resulting qubit state is measured (see section 5.2.2 for details on the pulse generation and measurement). Finally, the resulting data relates different pulse lengths to the resulting probability distribution or in other words, the rotation angle θ. The pulses calibrated this way are denoted by their rotation angle θ, as well as the rotation axis. For example, the pulse causing a rotation of $\Delta\theta = \pi$ around x is called a π or π_x pulse.

The qubit may loose its excitation by spontaneous emission into the resonator, its substrate, or the environment. In order to measure the energy relaxation time T_1, a π-pulse is applied to the qubit, preparing it in the $|1\rangle$ state. In consecutive measurements, the free evolution or delay time before readout is increased, revealing an exponential decay of the excited state $p(|1\rangle) = a_0 e^{-t/T_1}$ as predicted by Eq. (2.15).

Dephasing of the qubit is caused by variation of its transition energy. Depending on the physical implementation, many different sources for dephasing can be present. In general we can describe the incoherent environment by a noise spectral density $S(\omega)$. Note that different measurement sequences act as a filter and thus are sensitive to different parts of the noise spectrum. Among the pulse sequences used in this work are the Ramsey method and the Hahn or spin echo sequence [48]. For a Ramsey measurement, the sequence starts with a $(\pi/2)_x$ pulse, preparing the qubit in a superposition state on the equator, see Fig. 2.3(a). Next, the qubit state is left unchanged for the variable free evolution time Δt, depending on fluctuations in ω_q some additional phase $\Delta\phi = \Delta\omega_\mathrm{q} \cdot \Delta t$ is acquired, depicted by the green arrows in Fig. 2.3(b). Finally, another $(\pi/2)_x$ gate is applied and the state is measured, see Fig. 2.3(c). Without dephasing, the resulting state is $|1\rangle$. If the accumulated phase during free evolution is π, the final state is $|0\rangle$. As the accumulated phase differs across different measurements, the final state of the ensemble slowly decays towards the center of the Bloch sphere, on the time scale of T_2 [see Fig. 2.3(f)]. For an optimal measurement of T_2, intentionally detuning the $(\pi/2)_x$ pulses by $\Delta\omega_\mathrm{q}$ is beneficial. The additional phase leads to rotations around the z-axis during the free evolution, and consequently to oscillations in the final projection. The measurement result is a decaying sine function, oscillating at the detuning frequency $\Delta\omega_\mathrm{q}$ with a decay rate of T_2. This enables an accurate measure of variations in the qubits frequency, by extracting the detuning frequency. Further, the extracted T_2 time is more reliable, because the boundary value of $P(|1\rangle) = 0.5$ is well defined.

The spin echo is closely related to Ramsey measurements, however, an additional $\pm\pi_x$ (or $\pm\pi_y$) rotation is added halfway through the free evolution. This so-called "refocusing" pulse inverts any phase drift that is constant on the timescale Δt of the pulse sequence. Applying more than one refocusing pulse further increases the cutoff frequency of reversible noise components. A widely used example is the Carr-Purcell-Meiboom-Gill (CPMG) sequence [49], consisting of a train of evenly spaced π pulses during the free evolution time.

2.7 Superconductivity

For any physical system suitable as a qubit, dissipation has to be minimized as it corresponds to the loss of quantum information. For qubits based on macroscopic circuits, one way to avoid inherent dissipation is to avoid any resistive parts. Superconductors satisfy this requirement when cooled below their respective critical temperature T_c. In the following, a short summary of the relevant properties of superconductors and the related theoretical description is given.

2.7.1 Physical Properties

In 1908, the Dutch physicist Heike Kamerlingh Onnes accomplished the liquefaction of Helium by using the Hampson–Linde cycle. This enabled his groundbreaking discovery of "practically zero" resistance below 4.2 K for mercury, as Onnes wrote in his notebook [50]. Interestingly, during the same experiment the transition from liquid to superfluid helium was observed, but not immediately recognized.

Shortly after the discovery, measurements of persistent currents in superconducting rings and methods of different paths confirmed the assumption of zero resistance [51, 52]. Besides being a perfect conductor, superconductors are also ideal diamagnets. This manifests in the Meissner–Ochsenfeld effect [53], the expulsion of any magnetic field from superconductors when transitioning to the superconducting state. At a certain magnetic field strength, the so-called "Meissner state" without field lines penetrating the superconductor, breaks down. Superconductors can be divided into two groups, according to the functional dependence of the breakdown on the magnetic field. In type-I superconductors, superconductivity stops abruptly at a certain critical field $H_c(T)$. Pure metal superconductors, with the exception of Niobium, usually display this property.

Type-II superconductors exhibit two critical fields. Below the lower critical field $H_{c1}(T)$, the sample is in the Meissner state. Between $H_{c1}(T)$ and the higher critical field $H_{c2}(T)$, quanta of the magnetic field can penetrate the material, confined by vortices of supercurrent called Abrikosov vortices [54]. This state is also called mixed, Shubnikov, or vortex state. The amount of vortexes increases with the external field, until $H_{c2}(T)$ is reached and the superconducting state is destroyed [55].

A phenomenological description of superconductivity, capturing both the Meissner effect, and perfect conductance, was given in 1935 by Fritz and Heinz London [56]. The two London equations read

$$1. \quad \frac{\partial \vec{j}_s}{\partial t} = \frac{n_s e_s^2}{m_s}\vec{E} \qquad \text{and} \qquad 2. \quad \nabla \times \vec{j}_s = -\frac{n_s e_s^2}{m_s}\vec{B}, \tag{2.33}$$

with the superconducting current density $\vec{j}_s$, the electric and magnetic fields $\vec{E}$ and $\vec{B}$ inside the material. The constants n_s, m_s, and e_s are associated with charge carrier density, their mass, and charge, respectively. The London equations Eq. (2.33) state the lossless flow of current (1.) and that any magnetic field $\vec{B}$ implies a current density $\vec{j}_s$, to cancel the field (2.). Thus, the second London equation captures the Meissner effect.

If we apply Ampere's law $\nabla \times \vec{B} = \mu_0 \vec{j}$ to the second London equation, the resulting differential equation is given by

$$\nabla^2 \vec{B} = \frac{1}{\lambda_L^2}\vec{B}, \qquad \text{with} \qquad \lambda_L(T) \equiv \sqrt{\frac{m_s}{\mu_0 n_s(T) e_s^2}}. \tag{2.34}$$

The so called "London penetration depth" λ_L defines the characteristic length scale over which an external magnetic field $\vec{B}$ is exponentially suppressed.

2.7.2 Ginzburg-Landau Theory

The London equations capture the properties of type-I superconductors with constant charge carrier density n_s. However, they do not describe type-II superconductors. The Ginzburg-Landau theory describes the transfer into the superconducting state as a phase transition. It was initially postulated as a phenomenological theory, but could later be derived from the microscopic description by Bardeen, Cooper and Schrieffer [57, 58], which is discussed in the next section. The Ginzburg-Landau theory expresses the free energy F in terms of a complex order parameter $\psi(\vec{r})$, which is nonzero below the phase transition into the superconducting state. We can interpret the square of the absolute value $|\psi(\vec{r})|^2 = n_s$ as the carrier density of the superconducting state. It is this quantity we try to influence by using a gated semiconducting weak link, as is explained in section 2.8.2.

For a homogeneous superconductor of volume V, the free energy F_s of the superconductor can be expanded for small values of $|\psi(\vec{r})|^2$ as

$$F_s = F_n + \int_V \mathrm{d}^3 r \left(\alpha |\psi(\vec{r})|^2 + \frac{\beta}{2} |\psi(\vec{r})|^4 + \ldots \right). \tag{2.35}$$

With the free energy of the normal state F_n and the phenomenological parameters α and β. In a homogeneous superconductor without supercurrent it follows that $|\psi|^2 = -\alpha/\beta$, with

$\alpha < 0$ below T_c. For an added magnetic field $\vec{B}$ and under the condition of small $|\psi(\vec{r})|$ and its gradients, as can be assumed close to the phase transition, the free energy has the form [59]

$$F_s = F_n + \int_V \mathrm{d}^3 r \left[\alpha |\psi(\vec{r})|^2 + \frac{\beta}{2} |\psi(\vec{r})|^4 + \frac{1}{2m_\mathrm{s}} \left| \left(-i\hbar\nabla - e_s \vec{A} \right) \psi \right|^2 + \frac{|\vec{B}|^2}{2\mu_0} \right]. \tag{2.36}$$

Choosing the magnetic vector potential $\vec{A}$ such that $\vec{B} = \nabla \times \vec{A}$, a variation of ψ and $\vec{A}$ yields the equilibrium condition

$$\delta F_s = \frac{\partial F_s}{\partial \vec{A}} \delta \vec{A} + \frac{\partial F_s}{\partial \psi^\star} \delta \psi^\star = 0, \tag{2.37}$$

which can only be true, if both parts vanish individually. Minimizing the free energy leads to the "Ginzburg-Landau equations"

$$\frac{\partial F_s}{\partial \vec{A}} = 0 = -\Delta \vec{A} + \mu_0 \frac{e_s \hbar}{2m_\mathrm{s} i} (\psi^\star \nabla \psi - \psi \nabla \psi^\star) + \frac{e_s^2}{m_\mathrm{s}} \psi^\star \psi \vec{A}, \tag{2.38}$$

$$\frac{\partial F_s}{\partial \psi^\star} = 0 = \alpha \psi + \beta (\psi^\star \psi) \psi + \frac{1}{2m_\mathrm{s}} \left| -i\hbar\nabla + e_s \vec{A} \right|^2 \psi, \tag{2.39}$$

with the boundary condition

$$\int \mathrm{d}^2 r (-i\hbar\nabla + e_s \vec{A}) \psi = 0 \tag{2.40}$$

setting the supercurrent through the surface of the material to zero, corresponding to the Coulomb gauge $\nabla \vec{A} = 0$. By choosing a spatially constant order parameter $\nabla \psi = 0$ we can obtain the second London equation,

$$\nabla \times \vec{A} = \mu_0 \frac{e_s^2 n_\mathrm{s}}{m_\mathrm{s}} \vec{A} = \frac{\vec{A}}{\lambda_\mathrm{L}^2} = -\mu_0 \vec{j}_s \qquad \text{with} \qquad \psi^\star \psi = n_\mathrm{s}. \tag{2.41}$$

An important length scale of the superconducting phase is the so-called "Ginzburg-Landau coherence length" ξ_GL of the order parameter. It defines the scale of possible variations of the order parameter ψ within the superconducting phase. It is also known as "leakage-length" and defined as

$$\xi_\mathrm{GL}(T) = \sqrt{\frac{\hbar^2}{2m_\mathrm{s}|\alpha(T)|}}. \tag{2.42}$$

We can now discriminate between type-I and type-II superconductors by the relation of London penetration depth and Ginzburg-Landau coherence length. Both scale as $(1 - T/T_c)^{-1/2}$ with temperature, so their ratio is temperature independent. Type-I are materials with $\lambda_\mathrm{L}/\xi_\mathrm{GL} < 1/\sqrt{2}$, type-II with $\lambda_\mathrm{L}/\xi_\mathrm{GL} > 1/\sqrt{2}$ [60]. These relations have

a very intuitive interpretation. Type-I superconductors have a positive free energy of the superconductor-normal metal boundary, while it is negative for type-II materials. Negative surface energy indicates that the system will likely evolve towards a geometry where this surface is larger, allowing vortices to form.

The finite coherence length in superconductors is also responsible for the finite probability of Cooper pairs existing in adjacent insulators or normal conductors. This constitutes the basis for the Josephson effect, which is discussed in section 2.7.5.

2.7.3 Bardeen-Cooper-Schrieffer Theory

So far, no explanation for the appearance of superconductivity has been given. The microscopic theory by Bardeen, Cooper and Schrieffer, the so-called "BCS" theory, provides an explanation based on the pairing of electrons into a boson-like state [57]. Several experiments such as ultrasonic absorption [61], far-infrared spectroscopy [62] and the existence of a critical temperature reveal the existence of a band gap in the density of states (DOS) of the superconducting state. Further experiments show a dependence of T_c on the isotopic mass of the lattice atoms [63], the so-called "isotope effect".

A condensation into a single ground state, as seen in Bose-Einstein condensates, is as such impossible for electrons, because of the Pauli exclusion principle. In 1956, Cooper found that any net attractive force between electrons may lead to a bound state reducing the overall energy at low enough temperatures. This bound state, a so-called "Cooper pair", is of boson-like nature and provides the possibility of condensation into a common ground state. Spin-singlet Cooper pairs with $S = 0, L = 0$ are characterized by the state $|\vec{k}_i \downarrow, -\vec{k}_i \uparrow\rangle$ with equal end opposite momentum and spin. The BCS theory postulates phonons to mediate the attractive interaction, as is justified by the isotope effect. In this case, the new two-electron energy at the Fermi level is approximately [59]

$$E \approx 2E_F - 2\hbar\omega_D e^{\frac{-2}{N(E_F)V_0}}. \tag{2.43}$$

With the Fermi energy E_F, the Debye Frequency ω_D, the scattering potential V_0 and the DOS at the Fermi level $N(E_F)$. This shows a reduction with respect to the Fermi energy $2E_F$ close to the Fermi level, and thus produces an instability, resulting in the phase transition. For frequencies larger than ω_D, no phonons exist in the medium, limiting the attractive interaction to a small range of $\hbar\omega_D$ around the Fermi level. Compared with the Fermi level, the energy of phonons at the Debye frequency is small $\hbar\omega_D \ll E_F$. The low temperatures needed to induce superconductivity suppress thermally induced pair breaking. The size of the emerging energy gap Δ is

$$\Delta = \frac{\hbar\omega_D}{\sinh(1/N(E_F)V_0)} \approx 2\hbar\omega_D e^{\frac{-2}{N(E_F)V_0}}. \tag{2.44}$$

Close to the critical temperature, the material independent BCS prediction of the gap is

$$\Delta(T \to T_\mathrm{c}) \approx 3.06\, k_\mathrm{B} T_\mathrm{c} \sqrt{1-(T/T_\mathrm{c})}, \tag{2.45}$$

vanishing for $T = T_\mathrm{c}$. Any excitations in the superconducting state have to bridge this energy gap and are called Bogoliubov quasiparticles. They can be understood as a superposition of electron and hole, their excitation energy is

$$E_k = \sqrt{\xi_k^2 + |\Delta_k|^2}, \tag{2.46}$$

with the kinetic energy term

$$\xi_k = \sqrt{\frac{\hbar \vec{k}^2}{2m_k^\star} - \mu}, \tag{2.47}$$

containing the effective mass $m_k^\star$ and the chemical potential μ. The energy needed to break a Cooper pair is at least 2Δ for $\xi_k = 0$. This finite energy gap is responsible for the lossless flow of current because scattering events that transfer less than the equivalent energy of 2Δ have no free states to scatter into and thus cannot occur.

2.7.4 Fluxoid Quantization

Several experiments demonstrated that the sum of magnetic flux Φ penetrating a superconducting loop of area S, and the flux Φ_j generated by its persistent current $\vec{j}_\mathrm{s}$, is quantized. The quantity

$$\Phi' \equiv \underbrace{\iint_S \vec{H}\mathrm{d}\vec{S}}_{\Phi} + \underbrace{\frac{4\pi}{c}\lambda_\mathrm{L}^2 \oint \vec{j}_\mathrm{s}\mathrm{d}\vec{r}}_{\Phi_j} = n\Phi_0 \qquad n = 0, \pm 1, \pm 2, \ldots \tag{2.48}$$

was defined as the "fluxoid" by Fritz London. He predicted the quantization in multiples of the magnetic flux quantum $\Phi_0 = h/q = h/2e$, albeit mistakenly with the charge of a single electron $q = e$. One can argue, that if the condensate follows a wave function

$$\psi(\vec{r},t) = \sqrt{n_\mathrm{s}} e^{i\phi(\vec{r},t)} \tag{2.49}$$

assuming macroscopic phase coherence, it has to be single valued if we integrate along a closed path

$$\oint \nabla\phi \mathrm{d}\vec{r} = 2\pi n. \qquad n = 0, \pm 1, \pm 2, \ldots \tag{2.50}$$

Experimentally the quantization was shown by e.g. the Little-Parks effect, oscillations in T_c of a thin-walled superconducting cylinder exposed to a parallel magnetic field [64]. The experiments of Doll and Näbauer [65], as well as those of Deaver and Fairbank [66]

used small cylinders, oscillating orthogonal to their axis. Using different strategies, both concluded the value of $\Phi_0 = h/2e$ independently. This is seen as experimental proof for the macroscopic phase coherence and the existence of Cooper pairs.

The fluxoid quantization and the associated screening currents are essential in many modern superconducting devices such as SQUIDS[3] or flux-tunable qubits.

2.7.5 The Josephson Effect

A second crucial effect used in superconducting qubits arises if two superconductors are separated by a weak link [67]. This weak link can consist e.g. of a thin insulating barrier, a thin normal conductor, or a small constriction locally weakening the superconductivity, see Fig. 2.4(a). These structures are named "Josephson junctions" (JJ) after Brian David Josephson who predicted the effect in 1962. In addition to quasiparticle tunneling, Josephson considered the lossless tunneling of Cooper pairs. We can model the time dependent Schrödinger equation of two coupled superconductors as

$$i\hbar\frac{\partial\psi_{1,2}}{\partial t} = E_{1,2}\psi_{1,2} + K\psi_{2,1}. \tag{2.51}$$

K represents the coupling due to the exchange of Cooper pairs. Using the semi-classical wave function of Eq. (2.49), while separating imaginary and real part yields

$$\frac{\mathrm{d}n_{12}}{\mathrm{d}t} = \frac{2K}{\hbar}\sqrt{n_1 n_2}\sin(\phi_{1,2} - \phi_{2,1}) \qquad \text{with} \qquad \frac{\mathrm{d}n_1}{\mathrm{d}t} = -\frac{\mathrm{d}n_2}{\mathrm{d}t} \tag{2.52}$$

and

$$\frac{\mathrm{d}\phi_{1,2}}{\mathrm{d}t} = \frac{K}{\hbar}\sqrt{\frac{n_{1,2}}{n_{2,1}}}\cos(\phi_{2,1} - \phi_{1,2}) - \frac{E_{1,2}}{\hbar}. \tag{2.53}$$

We can define the phase difference between the two superconductors $\Delta\phi = \phi_2 - \phi_1$ and for two similar materials, the supercurrent is defined by the first Josephson equation

$$I = I_\mathrm{c}\sin(\Delta\phi). \tag{2.54}$$

With the critical current

$$I_\mathrm{c} = \frac{2e\hbar\kappa}{m_\mathrm{s}^\star}\frac{\sqrt{n_1 n_2}}{\sinh(2\kappa d)} \simeq \frac{2e\hbar\kappa}{m_\mathrm{s}}\sqrt{n_1 n_2}\cdot e^{-2\kappa d}, \tag{2.55}$$

similar to normal tunneling with the characteristic decay constant $\kappa = \sqrt{2m_\mathrm{s}(\Delta V_0)/\hbar^2}$ where ΔV_0 is the tunneling barrier. Eq. (2.54) shows, that no voltage drops across a

[3] SQUID is the abbreviation for "superconducting quantum interference device"

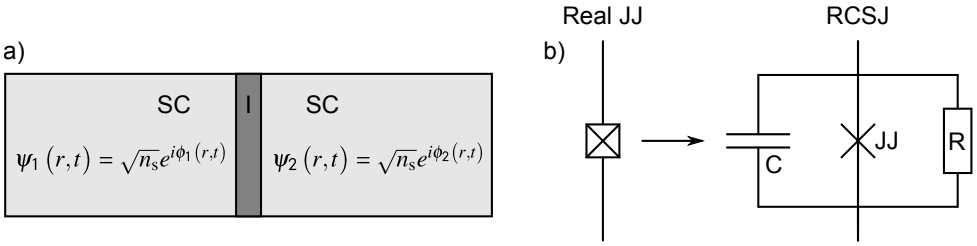

Figure 2.4: Schematic and circuit diagram of a single Josephson junction. (a) Two Superconductors (SC) are separated by an insulating (I) weak link. Their close proximity causes the phases ϕ_1 and ϕ_2 to be related following the Josephson equations. In (b), the equivalent circuit diagram for a Josephson junction (JJ) and its decomposition into the resistively and capacitively shunted (ideal) junction (RCSJ) model is shown.

Josephson junction while the current is below its critical value $I < I_c$. Eq. (2.53) defines the time evolution of the phase difference and can be summed up to

$$\frac{\mathrm{d}}{\mathrm{d}t}\Delta\phi = \frac{1}{\hbar}(E_1 - E_2). \tag{2.56}$$

If both superconductors have the same chemical potential $E_1 = E_2$, then the phase difference is constant $\Delta\phi = \text{const}$. According to Eq. (2.54) this results in a DC current. If any voltage U is applied, a finite phase difference follows

$$\frac{\mathrm{d}}{\mathrm{d}t}\Delta\phi = \frac{2e}{\hbar}U(t) = \frac{\Phi_0}{2\pi}U(t). \tag{2.57}$$

This is the second Josephson equation: for a constant voltage it predicts a constant phase change. In conjunction with the first Josephson equation Eq. (2.54), this results in an oscillating current with a frequency of $\nu = 2eU/\hbar$, called "AC Josephson effect". This frequency is, apart from natural constants, only dependent on the voltage and is used as the international voltage standard [68]. The phase difference across the junction $\Delta\phi$ is often referred to as the Josephson phase ϕ of the junction.

We can define a characteristic potential energy for JJs that is linked to the current. In an ideal inductor, flowing current creates a magnetic field storing the energy $E_{\mathrm{ind}} = {}^1\!/_2 LI^2$. For JJs, we can calculate the energy related to current across the junction as

$$E(\phi) = \int_0^t I_\mathrm{s} U \mathrm{d}t = \frac{\Phi_0}{2\pi}\int_0^t I_\mathrm{s}\frac{\mathrm{d}\phi}{\mathrm{d}t}\mathrm{d}t = \frac{\Phi_0}{2\pi}\int_0^\phi I_\mathrm{c}\sin(\phi)\mathrm{d}\phi = \frac{\Phi_0 I_\mathrm{c}}{2\pi}(1-\cos\phi), \tag{2.58}$$

with the so-called "Josephson energy" $E_\mathrm{J} = \Phi_0 I_\mathrm{c}/2\pi$. This energy is not associated with a magnetic field, but only dependent on the phase across the junction, and thus a potential energy. In the same manner we can assign a Josephson inductance to the junction. Comparing the voltage across a JJ, Eq. (2.57) to the voltage across an inductor $U_{\mathrm{ind}} = L \cdot \dot{I}$, we find

$$U = \frac{\hbar}{2eI_\mathrm{c}\cos(\phi)}\frac{\partial I}{\partial t}. \tag{2.59}$$

This corresponds to a phase dependent Josephson inductance

$$L_{\mathrm{J}}(\phi) = \frac{\Phi_0}{2\pi I_{\mathrm{c}} \cos(\phi)}, \tag{2.60}$$

which may become negative or even infinite. This nonlinear relation arising from the Josephson equations is the reason why superconducting circuits can have anharmonic energy levels serving as qubits. The dynamics of real Josephson junctions are often described by the resistively and capacitively shunted junction (RCSJ) model, see Fig. 2.4(b). In this equivalent circuit, the junction is replaced by three ideal elements in parallel: a Josephson junction, a resistor, and a capacitor. This is reasonable because any real junction includes a finite capacitance between the two electrodes. The resistance includes any dissipation, primarily to include the finite voltage regime. It is highly nonlinear, depending on voltage and temperature $R = R_{\mathrm{N}}$ for $|U| \geq 2\Delta(T)/e$. With the resistance in the normal state R_{N}.

If we consider the RCSJ model, the total junction current is given by [60, 69]

$$I = I_{\mathrm{c}} \sin(\phi) + \frac{U}{R} + C\frac{\mathrm{d}U}{\mathrm{d}t}. \tag{2.61}$$

Plugging in the second Josephson equation and using the normalized time $\tau = \omega_{\mathrm{p}} t$, we obtain a differential equation describing the motion of a "phase particle" with mass C in a tilted sinusodial or "washboard" potential experiencing drag proportional to $1/R$

$$\frac{I}{I_{\mathrm{c}}} = \frac{\mathrm{d}^2\phi}{\mathrm{d}\tau^2} + \frac{1}{\omega_{\mathrm{p}} RC}\frac{\mathrm{d}\phi}{\mathrm{d}\tau} + \sin(\phi). \tag{2.62}$$

With $\tau = \omega_{\mathrm{p}} t$ and the so-called "plasma frequency"

$$\omega_{\mathrm{p}} = \frac{1}{\sqrt{L_{\mathrm{J}} C}} = \sqrt{\frac{2eI_{\mathrm{c}}}{\hbar C}}. \tag{2.63}$$

ω_{p} can be understood as frequency of a small oscillation in any of the potential wells. For small phase differences ($\phi \bmod 2\pi \ll 1$), the junction itself resembles a parallel LC-circuit. A second characteristic frequency of Josephson junctions is defined as

$$\omega_{\mathrm{c}} = \frac{R_{\mathrm{N}}}{L_{\mathrm{J}}} = \frac{2e}{\hbar} V_{\mathrm{c}} = \frac{2\pi}{\Phi_0} V_{\mathrm{c}}, \tag{2.64}$$

with the characteristic voltage $V_{\mathrm{c}} = I_{\mathrm{c}} R_{\mathrm{N}}$, usually called $I_{\mathrm{c}}R_{\mathrm{N}}$-product. Together, ω_{c} and ω_{p} define the Stewart-McCumber parameter $\beta_{\mathrm{C}} \equiv \omega_{\mathrm{c}}^2/\omega_{\mathrm{p}}^2$. It can be understood as the square of the quality factor $Q^2 = \beta_{\mathrm{C}}$ for the LRC-cirquit depicted in Fig. 2.4(b). Junctions with $\beta_{\mathrm{C}} < 1/4$ are overdamped, corresponding to large drag in the mechanical analog. For larger values of $\beta_{\mathrm{C}} > 1/4$, the junction is underdamped and plasma oscillations are possible.

2.8 Physical Implementation

As stated in section 2.2, any quantum mechanical two-state system may be considered a qubit. However, to be of practical use in a real quantum computer, physical qubit implementations have to meet several criteria. These are directly connected to the so-called "DiVincenzo criteria" [70] outlining the minimal requirements for a quantum computer:

- A scalable physical system with well-characterized qubits
- The ability to initialize the state of the qubits to a reference state, such as to $|000...\rangle$
- A universal set of quantum gates
- Long relevant decoherence times, much longer than the gate-operation time
- A qubit-specific measurement capability

Several physical qubit implementations exist with different strengths and weaknesses regarding the DiVincenzo criteria. One possibility is to harness natural two-level systems like the spins of nuclei [71], the polarization of light [72] or the electronic configuration of single atoms [73]. Isolated systems like ions in a quadrupole trap [74] exhibit coherence times up to minutes [75] but face difficulties in scaling and fast initialization of many qubits. Other possible implementations are nuclear or electronic spins in semiconductor quantum dots or in impurity systems like color centers in diamonds, donors in silicon or rare-earth ions in solids[76, 77]. These can usually be realized at room temperature with coherence times on the order of milliseconds [78].

Superconducting solid-state qubits are among the largest physical qubits with dimensions on the order of 100 µm. This enables precise manipulation of their energy spectra via local control fields. Larger size also increases interactions with the environment or each other, reducing the coherence and gate times compared to other qubit implementations. Overall we believe superconducting qubits to be among the most promising candidates to realize a quantum computer. In fact, a recent demonstration of 'quantum supremacy' used a processor consisting of 53 superconducting qubits [19]. In this work we focus on so-called "transmon" qubits, which are discussed in the next section.

2.8.1 The Transmon

The transmon, which is an abbreviation for "transmission line shunted plasma oscillation" qubit, is a modification of a charge qubit or Cooper-pair box (CPB) [79]. Proposed by Jens Koch *et al.* [23] in 2007, the transmon aims for reduced sensitivity to charge noise

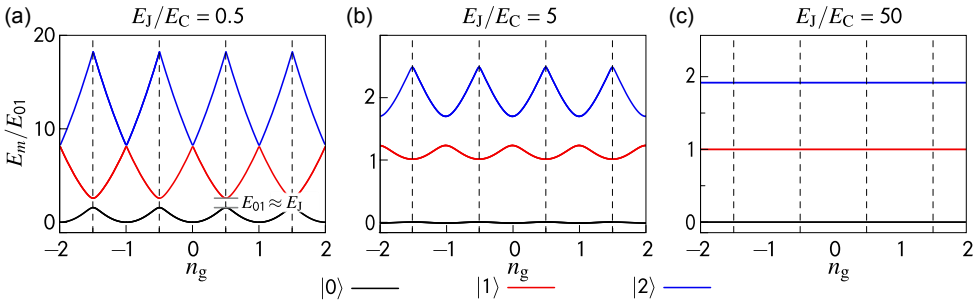

Figure 2.5: Eigenenergies of the first three levels of the transmon Hamiltonian, Eq. (2.65) plotted against the offset charge n_g for different ratios of Josephson to charging energy, as shown in Ref. [23]. The energy scale is normalized to the transition energy E_{01} at $n_g = 0.5$. In (a), for $E_J/E_C = 0.5$ the energy dispersion still resembles parabola, as expected for the charge regime. The Josephson coupling lifts the degeneracy and generates the computational basis with large anharmonicity at half integer n_g. In (b), the ratio of E_J/E_C increases and the dispersion flattens, until it is visibly flat in the transmon regime (c). With increasing E_J/E_C, the relative anharmonicity follows a weak power law, while the sensitivity to charge noise is reduced exponentially.

by capacitively shunting the two superconductors parallel to the junction, see Fig. 2.6(a). This increases the ratio of Josephson- to charge-energy E_J/E_C compared to charge qubits and exponentially flattens the charge dispersion with respect to $(E_J/E_C)^{1/2}$, as shown in Fig. 2.5.

The charging energy E_C is associated with the amount of energy stored in the electric field of the circuit per charge carrier and it can be written as $E_C = e^2/2C$. The effective Hamiltonian of a transmon is identical to that of a CPB [23]

$$\hat{H}_C = 4E_C(\hat{N} - n_g)^2 - E_J \cos\hat{\phi}. \tag{2.65}$$

With the number operator $\hat{N}$ corresponding to the number of Cooper pairs transferred across the junction, the offset charge on the island n_g, and the Josephson phase operator $\hat{\phi}$. The number operator is defined as

$$\hat{N} = \sum_N N\,|N\rangle\langle N|\,. \tag{2.66}$$

We define the commutation relation between number and phase operators after Dirac [80] as

$$\left[\hat{\phi}, \hat{N}\right] = -i. \tag{2.67}$$

With the phase as the conjugate variable with respect to the number of charge carriers. It is energetically unfavorable to change the amount of Cooper pairs on the island, if the charging energy is larger than the thermal energy $k_B < e^2/2C$. For a typical Josephson junction with a junction capacitance on the order of 1 fF/µm^2 at a temperature of $T = 20$ mK, the energy required to add one electron to the island is much larger than the thermal energy

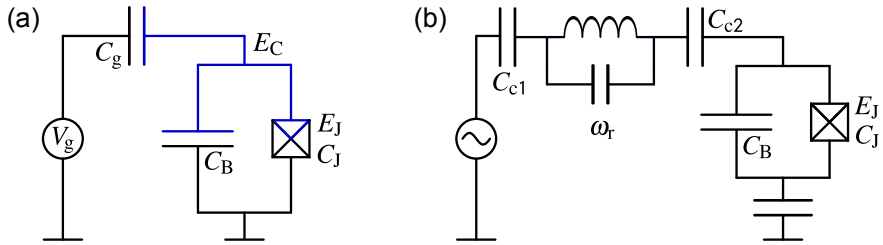

Figure 2.6: Circuit diagram of a transmon qubit. (a) as derived from the Cooper pair box, the superconducting island is depicted in blue. The shunting capacitance is labeled C_B, the offset charge can be adjusted by the voltage gate V_g. (b) Implementation in the presented experiments, capacitively coupled to a readout resonator of frequency ω_r via the coupling capacitance C_{c2}. A microwave feedline is coupled to the system capacitively by C_{c1}.

$E_C \approx 80\,\mu\text{eV} \gg k_B T \approx 1.7\,\mu\text{eV}$. This so-called "Coulomb blockade" [81] is the reason why the charge on the island of a CPB (blue part in Fig. 2.6) is well defined. Hence the CPB is said to operate in the charge regime. Its dispersion relation is composed of parabola centered at every integer number of Cooper pairs with avoided crossings proportional to the Josephson energy, see Fig. 2.5(a). The computational basis used in charge qubits is the coherent superposition of different charge eigenstates, created by the Josephson coupling.

For the transmon however, the charging energy is much smaller than the Josephson energy, typically their ratio is $E_J/E_C \gtrsim 50$. Its dispersion relation is almost flat with regard to the charge degree of freedom, as can be seen in Fig. 2.5(c). The transmon is usually described in the phase basis, the exact solution to the Hamiltonian Eq. (2.65) can be obtained in terms of Mathieu functions [82] as

$$E_m(n_g) = E_C a_{2[n_g + k(m,n_g)]}\left(-\frac{E_J}{2E_C}\right), \tag{2.68}$$

with the Mathieu characteristic values $a_{f(n,k)}$ and the integer function $k(m,n_g)$ sorting the correct eigenvalues with respect to the energy level m, and the offset charge. Due to the flat charge dispersion, the transmon is insensitive to charge fluctuations across the junction. For small fluctuations in charge with the noise amplitude A, the dephasing time can be estimated as

$$T_2 \sim \frac{\hbar}{A}\left|\frac{\partial E_{01}}{\partial n_g}\right|^{-1}. \tag{2.69}$$

The highest possible change in the charge dispersion is the tunneling of a single electron, shifting n_g by one half. Starting from an extremum, the frequency shift caused by this even-odd transition can be calculated by evaluation of Eq. (2.68) for two different values of k. In a transmon of $E_J/E_C \approx 80$, as e.g. used in this thesis, the maximum frequency shift

caused by tunneling of a single electron is $\Delta\omega_\mathrm{q} \approx 2\,\mathrm{Hz}$ and thus negligible in the presented experiments. The transmons peak-to-peak charge dispersion can be approximated by [23]

$$E_m^\mathrm{pp} = (-1)^m E_\mathrm{C} \frac{2^{4m+5}}{m!} \sqrt{\frac{2}{\pi}} \left(\frac{E_\mathrm{J}}{2E_\mathrm{C}}\right)^{\frac{m}{2}+\frac{3}{4}} e^{-\sqrt{8E_\mathrm{J}/E_\mathrm{C}}}. \tag{2.70}$$

The last term reveals an exponential suppression in peak-to-peak amplitude of the energy levels with respect to $E_\mathrm{J}/E_\mathrm{C}$. As can be seen in Fig. 2.5, the lower charge sensitivity is accompanied by decreased anharmonicity. To avoid excitation of higher levels, the anharmonicity needs to stay sufficiently large compared to the bandwidth of the used gate pulses. For $E_\mathrm{J}/E_\mathrm{C} \gg 1$, the cosine in Eq. (2.65) can be expanded around $\phi = 0$ to approximate the level spacing

$$E_m \approx -E_\mathrm{J} + \sqrt{8E_\mathrm{J}E_\mathrm{C}}\left(m+\frac{1}{2}\right) - \frac{E_\mathrm{C}}{12}(6m^2+6m+3). \tag{2.71}$$

The resulting anharmonicity $\alpha \equiv E_{12} - E_{01}$ and relative anharmonicity $\alpha_\mathrm{r} = \alpha/E_{01}$ are

$$\alpha \approx -E_\mathrm{C} \qquad \text{and} \qquad \alpha_\mathrm{r} \approx -(8E_\mathrm{J}/E_\mathrm{C})^{-1/2}. \tag{2.72}$$

This scaling of anharmonicity leaves a parameter range of $20 \lesssim E_\mathrm{J}/E_\mathrm{C} \ll 5 \cdot 10^4$ for transmon architectures [23], assuming a pulse duration of 10 ns.

The transmon Hamiltonian can also be formulated using the bosonic creation and annihilation operators $\hat{a}^\dagger$ and $\hat{a}$, which satisfy the commutation relation $\left[\hat{a}, \hat{a}^\dagger\right] = 1$. This notation is needed in the framework of the Jaynes-Cummings model (Sec. 3.2.1) and the dispersive readout (Sec. 3.2.2). We can write the basic Hamiltonian of a transmon qubit coupled to a resonator of frequency ω_r as [23]

$$\hat{H}_\mathrm{q} = 4E_\mathrm{C}(\hat{N} - n_\mathrm{g})^2 - E_\mathrm{J}\cos\hat{\phi} + \hbar\omega_\mathrm{q}\hat{a}^\dagger\hat{a} + \hbar g(\hat{a}^\dagger + \hat{a}). \tag{2.73}$$

Expanding the cosine in Eq. (2.73) in analogy to Eq. (2.71), the transmon system can be well approximated as [1]

$$H_\mathrm{q} = \hbar\omega_\mathrm{q} a^\dagger a - \hbar\alpha(a^\dagger)^2(a)^2, \tag{2.74}$$

with the anharmonicity α. This approximation follows from considering only number-conserving terms and applying normal ordering to the terms up to fourth order in $\hat{\phi}$. It is valid for large $E_\mathrm{J}/E_\mathrm{C}$ in the dispersive limit, which is discussed in Sec. 3.2.2

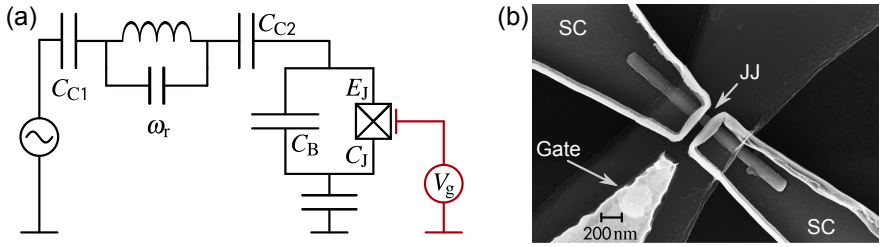

Figure 2.7: (a) Circuit diagram of a gatemon qubit as used in the presented experiments. (b) Scanning electron microscope image of a gatemon junction with side-gate. The superconducting contacts appear transparent, a detailed description of the related fabrication is given in Sec. 4.2.

2.8.2 The Gatemon

To achieve a tunable transition frequency in transmon qubits, the single JJ is usually replaced by two parallel junctions forming a loop also called split-junction. The effective E_J of this dc-SQUID can now be tuned by an external flux. Typically a bias coil is fabricated next to the split-junction to provide local flux. A precisely controlled current through the bias coil is then used to tune the qubit to its desired frequency.

The "gatemon" is a variation of the transmon qubit, that achieves tunabiliy by employing a semiconducting weak link instead of an SIS junction. As shown in Eq. (2.55) the critical current depends on the charge carrier density of the respective material. In a semiconductor, this carrier density can be varied by an electrostatic gate. The equivalent circuit diagram is shown in Fig. 2.7(a). Due to the finite coherence length outside the superconductor, superconductivity can be induced into the junction material. This so-called "proximity effect" [83–85] also affects the superconductor close to the junction and is highly sensitive to the transmission coefficient of the interfaces. For highly transparent material combinations it is possible to create semiconducting Josephson junctions usable in qubits. With this technique, the critical current and thus the transition frequency of gatemons can be tuned in a wide range. Depending on the junction and gate geometry, the supercurrent may be suppressed completely by the gate [86].

Contingent on the architecture, crucial operations in quantum processors rely on fast and reliable tuning of qubit frequencies. Prime examples are swap-gates [87], manipulating inter-qubit coupling and setting the qubit frequencies with respect to readout resonators or parametric amplifiers. Gatemon qubits simplify gate architectures by only needing one tunable junction in contrast to split-junctions. Further, voltage gates can be fabricated very close to the junction and have very small cross talk compared to flux tuning. In our fabrication, the gate-junction distance is defined by the layer of dielectric of $\approx 15\,\mathrm{nm}$ (see Sec. 4.2). The resulting higher possible qubit density and simplified calibration may help

to mitigate scaling challenges. In comparison to traditional transmon qubits, gatemons are still not widely adopted despite the above-named advantages. One reason is the tendency for metal-semiconductor junctions to form Schottky barriers [88] and thus constitute a parasitic resistance, rendering a persistent qubit excitation impossible. One solution is the use of semiconductors that intrinsically form ohmic contacts with the superconductor in question, as further discussed in section 5.3.

As of today, nanowires [89] or layered stacks forming two-dimensional electron gases (2DEG) [90] are used to incorporate semiconductors as junction material. This technology is still in development and new geometries and techniques are to be expected. A scanning electron microscope (SEM) image of a tunable junction based on an indium arsenide (InAs) nanowire is shown in Fig. 2.7(b). The depicted sample was fabricated in the course of this project by Patrick Zellekens.

3 Quantum Circuits

A quantum processor can only work, if its qubits evolve undisturbed for a sufficiently long time on average. "Long" here means until the computation is finished or longer than the threshold for quantum error correction [91]. It is thus necessary, to isolate the qubit from the environment to prevent decay and dephasing. However, in order to perform computations, gates need to change the quantum state and at some point this state needs to be observed to extract the result. A totally isolated system is thus not a useful qubit according to the DiVincenzo criteria (see sec 2.8).

For superconducting qubits, the dilemma of introducing a loss channel together with the needed coupling to the qubit is usually met by using a readout resonator to couple the qubit to the feedline. This resonator is detuned from the qubit frequency and acts as a band-pass filter. Further, the noise level, temperature, and local material loss need to be minimized to ensure sufficiently long coherence times, as shown in section 5.2.1. To further reduce radiative decay, additional resonators called "Purcell filters" may be added [92]. In the following, the theoretical aspects and the practical approach to build a quantum circuit are presented.

3.1 Microwave circuits

All presented experiments are implemented in the microwave regime, with frequencies on the order of 10 GHz. As measured in the year 1887 in Karlsruhe by Heinrich Hertz, electrical circuits behave distinctly different from their low-frequency counterparts [93]. If the wavelength is comparable to the size of the circuit, electromagnetic (EM) radiation becomes important, interference and polarization effects have to be considered. In the following, a short summary of transmission lines, scattering parameters and resonators in microwave circuits are given.

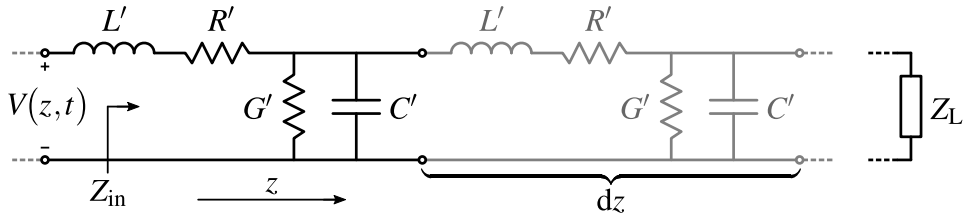

Figure 3.1: Schematic of the lumped-element equivalent circuit for an infinitesimal piece of transmission line (black). The lumped circuit elements for line length element dz, series inductance L', series resistance R', shunt capacitance C', and shunt conductance G' are given per unit length. Together these form the transmission lines characteristic impedance Z_0. The input impedance Z_{in} depends on the length z and the load impedance Z_{L} terminating the line. If the load impedance equals Z_0, it is considered a matched load and no signal is reflected. This is usually the desired case, to avoid standing waves and frequency dependent amplitudes at the sample.

3.1.1 Transmission Lines

The task of a transmission line is to conduct a signal across a distance z ideally without altering it. For low frequencies, one usually views signal wires as instantaneously equalizing the potential, acting like a small resistor. However, if the signals wavelength becomes comparable to z, the variation of current and voltage across the wire, its inductance, capacitance and the radiation of electromagnetic waves can no longer be ignored. The transmission line is a circuit element and a distributed parameter network [94].

In microwave engineering, a transmission line is modeled as an assembly of infinitely many two-port elementary components. The line properties are then specified per unit length and can be integrated to yield the effect on the signal. The related lumped-element model, as shown in Fig. 3.1 is applicable, since the infinitesimal line segments are again short compared to the wavelength. Application of Kirchhoff's rules to the lumped element model yield the telegrapher equations

$$\frac{\mathrm{d}V(z)}{\mathrm{d}z} = -(R' + i\omega L')I(z) \qquad \text{and} \qquad \frac{\mathrm{d}I(z)}{\mathrm{d}z} = -(G' + i\omega C')V(z), \tag{3.1}$$

describing the signal propagation along a transmission line. The series resistance R', series inductance L', shunt capacitance C', and shunt conductance G' are the properties per unit length. A plane wave ansatz solves equations (3.1) and yields

$$V(z) = -V_0^+ e^{-\gamma z} + V_0^- e^{\gamma z} \qquad \text{and} \qquad I(z) = -I_0^+ e^{-\gamma z} + I_0^- e^{\gamma z}, \tag{3.2}$$

for the voltage and current, respectively. Here, the complex propagation constant is

$$\gamma = \alpha + i\beta = \sqrt{(R' + i\omega L')(G' + i\omega C')} \tag{3.3}$$

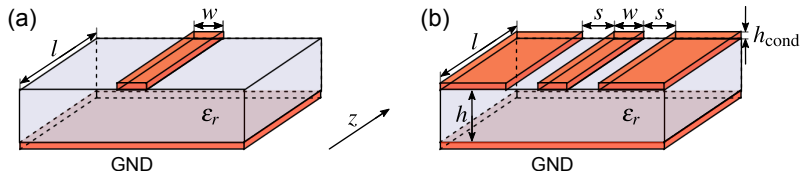

Figure 3.2: Equivalent geometries of stripline (a) and coplanar waveguide (b), commonly used in planar microwave circuits. Here, the conductors are thin sheets of metal (orange), with thickness on the order of $h_{\text{cond}} \sim 100\,\text{nm}$ on the superconducting samples. The substrate used in this work is intrinsic silicon with $h \sim 400\,\mu\text{m}$ and a dielectric constant of $\varepsilon_r = 11.68$. The characteristic line impedance can be adjusted by the ratio of s and w for the coplanar (CPW) and by the width w for the stripline. Depending on the substrate ε_r and height h, the ground layer is not always necessary for CPW. For a stripline however, it is the single ground reference. For both geometries, the ground layer and dielectric may be mirrored to sandwich the transmission line in multilayer assemblies.

and the terms with positive (negative) γ represent waves propagation in the positive (negative) z direction. The real part of the propagation constant contains the dissipation due to the series and parallel resistances R' and $1/G'$, including dielectric loss. While the imaginary part includes the reactive components and thus the phase. The relation between voltage and current for any given point along a transmission line are defined by its characteristic impedance Z_0, defined as

$$Z_0 = \frac{V_0^+}{I_0^+} = \frac{V_0^-}{I_0^-} = \sqrt{\frac{R' + i\omega L'}{G' + i\omega C'}}. \tag{3.4}$$

Any load Z_L that deviates from Z_0 creates a boundary where the traveling wave is scattered. The amplitude of the reflected signal in relation to the incident wave is given by the "voltage reflection coefficient" Γ

$$\Gamma = \frac{V_0^-}{V_0^+} = \frac{Z_\text{L} - Z_0}{Z_\text{L} + Z_0}. \tag{3.5}$$

No reflection occurs, if the load equals the line impedance $Z_\text{L} = Z_0$. Such a load is called "matched" to the line. Avoiding reflections is of particular importance for quantum circuits, as the signals are usually in the single photon regime. So reducing the signal by unwanted reflections may drastically reduce the signal-to-noise ratio (SNR). The effective impedance Z_in seen from the port of the transmission line depends on the load impedance and the distance to the load d as

$$Z(l) = Z_0 \cdot \frac{Z_\text{L} + Z_0 \tanh(\gamma l)}{Z_0 + Z_\text{L} \tanh(\gamma l)}. \tag{3.6}$$

The transmission lines used in the presented experiments are mainly commercial coaxial cables with a standardized line impedance of $50\,\Omega$ (for details on the microwave wiring, see section 5.2.2). To minimize reflections, the thin film feedline on the sample chip needs

to be matched to the 50 Ω line impedance. For 2D-structures, two of the most popular designs are the coplanar and the stripline geometries, as shown in Fig. 3.2.

A single slit in a conducting plane also constitutes a transmission line, called slot line. The coplanar waveguide (CPW) can be understood as two coupled slot lines. Its characteristic impedance can then be approximated in the relevant parameter range $1.5 \leq \varepsilon_r \leq 120$, as calculated by Simons [95]. For the chip and circuit design, the initial parameters are calculated using

$$s = w \cdot \left[\frac{1}{4} \exp\left(\frac{30\pi^2}{Z_0 \varepsilon_{\text{eff}}^{0.5}} \right) + \exp\left(-\frac{30\pi^2}{Z_0 \varepsilon_{\text{eff}}^{0.5}} \right) - 1 \right], \tag{3.7}$$

with the effective dielectric constant ε_{eff}, including the mode volume in vacuum.

For the feedline on intrinsic silicon ($\varepsilon_r = 11.68$) with a thickness of $h = 380\,\mu\text{m}$, the chosen values are $w = 12\,\mu\text{m}$ and $s = 7\,\mu\text{m}$. For a signal of 10 GHz, these parameters result in $Z_0 = 50\,\Omega$ and an effective electrical length of $30^\circ/\text{mm}$. For the chip carrier, milled `TMM10`[1] substrate [96] was used. In order do contact the feedline and connect it to the coaxial signal lines, its width needs to be increased until a bond wire can be attached. To reduce mismatch loss, taper on both sides of the carrier and the feedline smoothly increase the conductor width while maintaining the characteristic impedance of 50 Ω. Examples of such a taper are depicted in Figs. 5.6 and A.1.

3.1.2 S-Parameters

Microwave networks with matched load terminations, like the presented experimental setup (see also section 5.2.1) can be described using the elements of a scattering matrix. These are called "S-parameters" and characterize the amplitude and phase characteristics of single- or multi-port networks between all possible port combinations. Every matrix element $S_{i,j}$ represents the factor relating the voltage V_j^+ of an incident signal from port i, with the resulting output voltage V_i^- on port j, such that [94]

$$S_{i,j} = \left. \frac{V_i^-}{V_j^+} \right|_{V_k^+ = 0 \text{ for } k \neq j}. \tag{3.8}$$

This definition requires all ports except i and j to be set to zero. S-parameters are the measured variable of network analyzers, which are the standard tool for spectroscopic measurements. It is possible to calculate the impedance (Z) and admittance (Y) matrices from the S matrix and vice versa.

[1] The used substrate is coated with 35 µm copper on both sides and has a thickness of 640 µm.

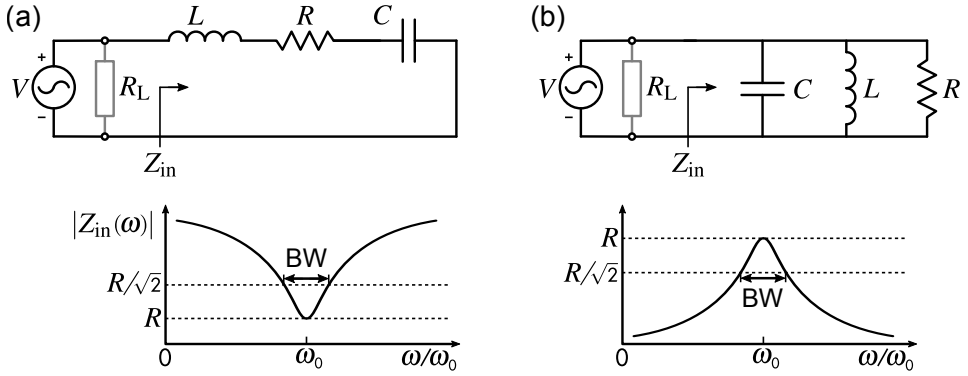

Figure 3.3: Schematics of equivalent circuits for electrical resonators also called "RLC circuits" in series (a) and parallel (b) topology. The respective magnitude of the input impedance $|Z_{\mathrm{in}}(\omega)|$ as seen from the source V is depicted below each circuit. On resonance, this impedance is purely real and only depends on the dissipative part $Z_{\mathrm{in}}(\omega_0) = R$.

Passive networks that only contain isotropic materials are reciprocal. In this case, the S matrix is symmetrical $S_{i,j} = S_{j,i}$ and $S_{i,i} = S_{j,j}$. For the presented experiments, active and non-isotropic elements as e.g. amplifiers and circulators are in the signal chain, rendering them non-reciprocal. In networks where all ports are matched to the line impedance, the reflection vanishes and diagonal entries in the S matrix are zero. This can be seen by setting $Z_{\mathrm{L}} = Z_0$ in Eq. (3.5). Thus, the reflection coefficient is a benchmark for the quality of impedance matching in connections like the bond wires.

3.1.3 Resonators

Electrical circuits comprising inductive and capacitive elements have a resonance frequency due to the opposing phases of their impedance. This also holds if the circuit does not include the dedicated components inductor or capacitor, because small amounts of inductance and capacitance are unavoidable due to the finite size of any conductor. Resonators in superconducting circuits are usually realized by a short piece of conductor with shorted or open ends, creating the boundary condition for a standing wave.

Close to resonance, even these distributed resonators can be modeled by lumped-element equivalent circuits [94]. The most general model here is an RLC circuit, named after its components: resistor (R), inductor (L), and capacitor (C). These can be arranged in series or parallel, as can be seen in Fig. 3.3 (a) and (b) respectively. The effective input impedance Z_{in} for the series configuration is

$$Z_{\mathrm{in}} = R + i\omega L - i\frac{1}{\omega C} \tag{3.9}$$

and for the parallel configuration

$$Z_{\text{in}} = \left(\frac{1}{R} - i\frac{1}{\omega L} + i\omega C \right)^{-1}. \tag{3.10}$$

As can be seen in equations (3.9) and (3.10), the imaginary parts due to inductive and capacitive elements have opposite signs and mutually inverse dependence on frequency. The frequency, where these so-called "reactive" parts cancel out and the effective impedance Z_{in} becomes purely real, is the resonance frequency ω_0. For both topologies it is defined by

$$\omega_0 = \frac{1}{\sqrt{LC}}. \tag{3.11}$$

The bandwidth (BW) of the resonance dip or peak is an important parameter of every resonator. It depends on the amount of dissipation per oscillation measured by the so-called "quality factor" Q, which is defined as

$$Q = \omega_0 \frac{W_m + W_e}{P_d}. \tag{3.12}$$

Here, W_m and W_e are the averaged magnetic and electric energy stored in the inductor and capacitor respectively and P_d is the averaged dissipated power. On resonance, electric and magnetic energy are equivalent $W_e = W_m$. The quality factor of the bare resonator circuit, also called "unloaded" quality factor is

$$Q_{\text{i}} = \frac{\omega_0 L}{R} = \frac{1}{\omega_0 RC} \qquad \text{and} \qquad Q_{\text{i}} = \frac{R}{\omega_0 L} = \omega_0 RC \tag{3.13}$$

for the series and parallel RLC circuits, respectively. It can be understood as a measure of the systems damping, associated with the exponential decay of energy in a dissipative harmonic oscillator. The Fourier transform of an exponential function is Lorentzian. Thus, the Lorentzian line shape of the squared amplitude of the resonators S-matrix element can be used to link its bandwidth Γ, the characteristic decay time of the oscillation τ, and the quality factor as (see Appendix A for the calculation)

$$\Gamma = \frac{\omega_0}{2Q_L} \qquad \tau = \frac{2Q_L}{\omega_0}. \tag{3.14}$$

In this case, the "loaded" quality factor Q_L is used because the resonant circuit is connected to a feedline leading to additional dissipation due to the load resistance R_{L} (see Fig. 3.3). Loss due to the coupling is characterized by the "external" or coupled quality factor Q_{c}. The equivalent circuit suggests the loss factors to be connected by

$$\frac{1}{Q_L} = \frac{1}{Q_{\text{i}}} + \frac{1}{Q_{\text{c}}}. \tag{3.15}$$

How strongly the resonator is affected by the feedline can be expressed by the coupling factor κ_{r}. It is defined by the ratio of Q_{i} and Q_{c}, it follows $Q_{\text{i}} = \kappa_{\text{r}} Q_{\text{c}} = (\kappa_{\text{r}} + 1) Q_L$. The

coupling is called undercoupled ($\kappa_r < 1$) or overcoupled ($\kappa_r > 1$) if the dissipation is dominated by the internal or external quality factor, respectively. If the loss in the resonator equals the coupling losses ($\kappa_r = 1$), it is critically coupled. In the series RLC circuit, Q_c and κ_r are

$$Q_c = \frac{\omega_0 L}{R_L} \qquad \text{and} \qquad \kappa_r = \frac{R_L}{R}. \tag{3.16}$$

In the parallel configuration, the expressions are inverted

$$Q_c = \frac{R_L}{\omega_0 L} \qquad \text{and} \qquad \kappa_r = \frac{R}{R_L}. \tag{3.17}$$

For the design of readout resonators, the coupling factor is critical. The resonator needs to be coupled strong enough to the transmission line, to provide sufficient signal. However, its bandwidth should remain low enough not to compromise the dispersive readout, explained in section 3.2.2. The maximum measurement rate is naturally limited by the coupling. Here usually the coupling rate κ is used, which denotes the photon leakage rate out of the cavity.

3.2 Cavity Quantum Electrodynamics

The interaction of light and atoms in a system, where the electromagnetic spectrum is determined and quantized by a cavity, is called cavity quantum electrodynamics (cavity QED). Besides optical cavities [97], superconducting circuits offer the possibility to study fundamental quantum mechanical interactions of open systems or measurement induced decoherence [98]. Conditions that facilitate coherent oscillations of a single excitation between atom and cavity are of particular interest. These so-called vacuum Rabi oscillations between atom and cavity occur if the exchange rate exceeds the rates of relaxation and dephasing in both systems. This regime can be realized with superconducting circuits, rendering them a versatile platform for cavity QED experiments [99]. The system consisting of qubit and readout resonator usually belongs in this category. However, if we restrict the system to an ideal two-level system coupled to a resonator, it holds only qualitatively for the transmon, because its higher levels are ignored.

3.2.1 Jaynes-Cummings Model

The basic interaction of a two-level system with the quantized mode of a cavity is described by the Jaynes-Cummings model of quantum optics. A famous example is the experiment of Haroche and Raimond, using Rydberg atoms to probe microwave photons [100, 101].

The coupling between the electric dipole moment $\vec{d} \propto \vec{d}_0 \hat{\sigma}_x$ of the atom and the quantized electric field $\vec{E} \propto (\hat{b}^\dagger + \hat{b})$ of the cavity mode is proportional to $\vec{\hat{E}} \cdot \vec{\hat{d}}$. It can be expressed as

$$\hat{H}_\mathrm{c} = \hbar g \hat{\sigma}_x \left(\hat{b}^\dagger + \hat{b}\right), \tag{3.18}$$

with the coupling strength g and the harmonic creation and annihilation operators $\hat{b}^\dagger$ and $\hat{b}$ for the cavity photons, satisfying $\left[\hat{b}, \hat{b}^\dagger\right] = 1$. For the full system consisting of cavity and atom (qubit), the Hamiltonian reads

$$\hat{H} = \hbar \frac{\omega_\mathrm{q}}{2} \hat{\sigma}_z + \hbar \omega_\mathrm{r} \left(\hat{b}^\dagger \hat{b} + \frac{1}{2}\right) + \hbar g \hat{\sigma}_x \left(\hat{b}^\dagger + \hat{b}\right) + \hat{H}_\kappa + \hat{H}_\gamma. \tag{3.19}$$

With the qubit energy $\hbar\omega_\mathrm{q}$ and the number of photons $\hat{b}^\dagger \hat{b}$ with the frequency ω_r of the relevant cavity mode [102]. $\hat{H}_\kappa$ describes the coupling of the cavity to the environment, resulting in decay at the rate

$$\kappa = \omega_\mathrm{r} / Q_\mathrm{L}. \tag{3.20}$$

In Eq. (3.19), $\hat{H}_\gamma$ represents the qubits relaxation and dephasing [98]. For simplicity, we neglect potential higher levels of the qubit and treat it as a perfect two-level system.

If the coupling energy of the cavity QED system in question is much smaller than the energies of the cavity and qubit excitations ($g \ll \omega_\mathrm{q}, \omega_\mathrm{r}$), a rotating wave approximation (RWA) can be applied, transforming Eq.(3.19) into the Jaynes-Cummings Hamiltonian [103]

$$\hat{H}_\mathrm{JC} = \hbar \frac{\omega_\mathrm{q}}{2} \hat{\sigma}_z + \hbar \omega_\mathrm{r} \left(\hat{b}^\dagger \hat{b} + \frac{1}{2}\right) + \hbar g \left(\hat{\sigma}_+ \hat{b} + \sigma_- \hat{b}^\dagger\right). \tag{3.21}$$

Here, the loss terms are omitted and the transversal coupling is re-written using the identity $\sigma_x = \sigma_+ + \sigma_-$. In the rotating wave approximation, the so-called "counter-rotating" terms $\sigma_+ \hat{b}^\dagger$ and $\sigma_- \hat{b}$ are neglected, because they oscillate rapidly compared to the timescale of relevant system dynamics.

3.2.2 Dispersive Readout

Diagonalization of the Jaynes-Cummings Hamiltonian Eq. (3.21) yields the ground state $|g,0\rangle$ and the dressed excited eigenstates [98]

$$\begin{aligned} |\overline{+,n}\rangle &= \quad \cos\theta_\mathrm{n} |e,n\rangle + \sin\theta_\mathrm{n} |g,n+1\rangle, \\ |\overline{-,n}\rangle &= -\sin\theta_\mathrm{n} |e,n\rangle + \cos\theta_\mathrm{n} |g,n+1\rangle, \end{aligned} \tag{3.22}$$

with the mixing angle

$$\theta_\mathrm{n} = \frac{1}{2} \arctan\left(\frac{2g\sqrt{n}}{\Delta}\right), \tag{3.23}$$

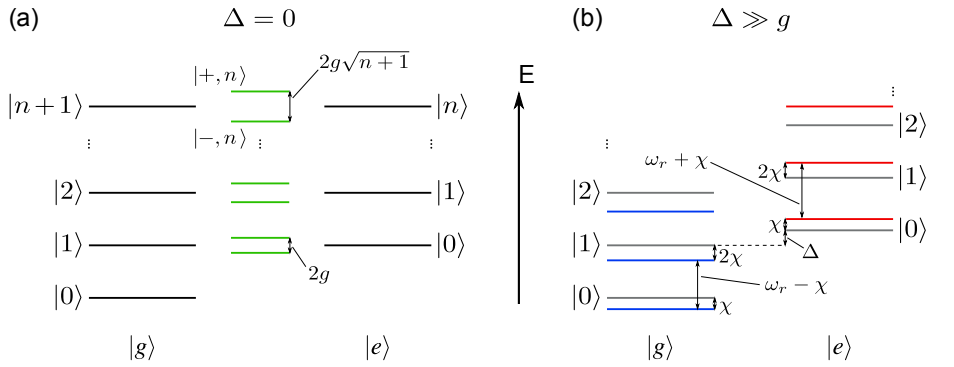

Figure 3.4: Visualization of the energy level structure for the coupled system of qubit and resonator. The uncoupled energy spectra are depicted in black, with the cavity photon number n rising from bottom to top and the ground (excited) state of the qubit on the left (right). (a) shows the dressed states in the resonant case in green. Cavity and qubit form a superposition state with an energy splitting proportional to $2g\sqrt{n+1}$. (b) In the dispersive regime, the level spacing depends on the state of the qubit, enabling the so-called "dispersive readout".

dependent on the detuning $\Delta = \omega_\mathrm{q} - \omega_\mathrm{r}$. It is important to note, that these states are no longer eigenstates of either qubit or resonator, but a collective excitation of the two. Except for the ground state $|g,0\rangle$, the relevant number of excitations in the system is the total photon number $N = n+1$, not the number of photons in the cavity. This also means, that part of the qubit excitation is now in the cavity and vice versa, enabling readout (and decay) of the qubit state through the cavity possible. For the resonant case $\Delta = 0$ ($\Delta \ll g$) the eigenstates of the system are an equal superposition of $|g,n+1\rangle$ and $|e,n\rangle$

$$|\pm,n\rangle = \frac{1}{\sqrt{2}}\left(|g,n+1\rangle \pm |e,n\rangle\right). \tag{3.24}$$

Here, resonator and qubit coherently exchange energy at the vacuum Rabi frequency $\Omega/2\pi = g\sqrt{n+1}$. Fig. 3.4(a) depicts the energy spectrum in the resonant case in green. Excluding the ground state $|g,0\rangle$, the corresponding eigenenergies of the Jaynes-Cummings Hamiltonian Eq. (3.21) are

$$E_{|\pm,n\rangle}(\Delta) = \hbar\omega_\mathrm{r}(n+1) \pm \frac{\hbar}{2}\sqrt{4g^2(n+1)+\Delta^2} \tag{3.25}$$

for the dressed state.

In the so-called "dispersive limit", resonator and qubit are far detuned compared to their coupling strength $g \ll \Delta$. In this case, the new basis states $|\overline{\pm,n}\rangle$ are similar to the pure qubit and resonator states with a small correction. For $g/\Delta \ll 1$, the Hamiltonian Eq. (3.21) can be diagonalized approximately [98], which yields

$$\hat{H}_\mathrm{eff} \approx \hbar\left(\omega_\mathrm{r}' + \chi_\mathrm{eff}\hat{\sigma}_z\right)\hat{b}^\dagger\hat{b} + \frac{\hbar}{2}\left(\omega_\mathrm{q}' + \chi_\mathrm{eff}\right)\hat{\sigma}_z, \tag{3.26}$$

with the shifted resonator and qubit frequencies $\omega_\mathrm{r}' = \omega_\mathrm{r} - \chi_{01} - \chi_{02}$ and $\omega_\mathrm{q}' = \omega_\mathrm{q} + \chi_{01}$. This way, the uncoupled Hamiltonian is restored, except for a small correction given by the effective dispersive shift, which also depends on the next higher level [104]

$$\chi_\mathrm{eff} = \chi_{01} - \frac{\chi_{12}}{2} + \frac{\chi_{02}}{2} \qquad \text{with} \qquad \chi_{ij} = \frac{g_{ij}^2}{\omega_{ij} - \omega_\mathrm{r}}. \tag{3.27}$$

Higher levels have to be included, because the coupling may be similar to the charging energy $g \sim E_\mathrm{C}$. Here, we consider transitions between the lowest three levels. The effective dispersive shift can be written as

$$\chi_\mathrm{eff} \simeq \frac{g^2}{\Delta} \frac{-\hbar\omega_\mathrm{p}}{4(\hbar\Delta - E_\mathrm{C})}. \tag{3.28}$$

In this case the one excitation eigenstates are

$$\begin{aligned} |\overline{+,0}\rangle &\sim \quad |e,0\rangle + \left(\frac{g}{\Delta}\right)|g,1\rangle\,, \\ |\overline{-,0}\rangle &\sim -\left(\frac{g}{\Delta}\right)|e,0\rangle + |g,1\rangle\,. \end{aligned} \tag{3.29}$$

The corresponding energy spectrum is shown in Fig. 3.4(b). Blue and red depict the respective energy levels of the coupled system for the qubit in the ground and excited state. The coupling between qubit and cavity scales with the electric field and therefore with the number of photons in the cavity n. Above a critical photon number [98]

$$n_\mathrm{crit} = \frac{\Delta^2}{4g^2}, \tag{3.30}$$

the dispersive limit $g/\Delta \ll 1$ breaks down and the state of the coupled system can no longer be approximated by qubit and cavity eigenstates. The state separation and thus the resonator's eigenfrequency is now dependent on the qubit state. This can also be seen in Eq. (3.26), where the bare resonator frequency is replaced by $\omega_\mathrm{r}' + \chi_\mathrm{eff}\hat{\sigma}_z$. Thus, by populating the resonator and measuring ω_r via the reflected or transmitted signal, the qubit state can be deduced. As we described in the previous chapter, the linewidth of the readout resonator is given by the total loss rate

$$\kappa_\mathrm{L} = \omega_\mathrm{r}/Q_\mathrm{L} \tag{3.31}$$

determined by the loaded quality factor, see Eq. (3.15). Thus, the resulting resonance peaks for the two qubit states are separated, if $\kappa_\mathrm{L} < \chi_\mathrm{eff}$. However, this is not a requirement for successful readout because of the finite slope of the phase signal ($\propto \tanh(\omega)$) at $\omega = \omega_\mathrm{r}$. So the measurement can either be performed, by applying a pulse of frequency $\omega_\mathrm{r}' + \chi_\mathrm{eff}$ and observing the transmission amplitude, or by choosing a drive at the bare

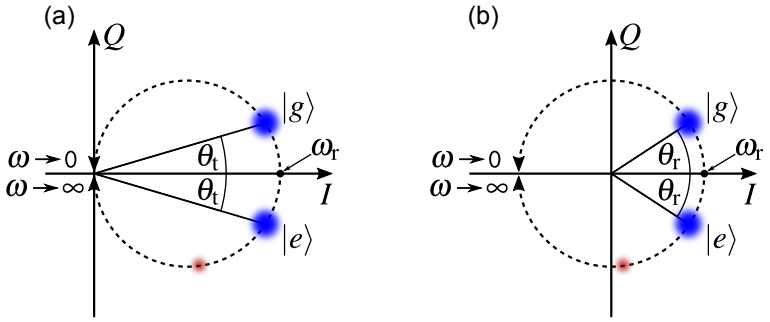

Figure 3.5: Sketch of the response of an ideal readout resonator coupled to a qubit in transmission (a) and reflection (b). The bare resonator frequency is ω_r and the average response to a varying drive frequency is shown by the dashed circle. Its diameter is given by the linewidth and thus defined by κ_r [105]. Coupling to the qubit shifts the response at $\omega = \omega_\mathrm{r}$ by $\pm\chi_\mathrm{eff}$ to the blue dots, depending on the state of the qubit. The separation of $|g\rangle$ and $|e\rangle$ and thus the SNR is identical in both configurations. In the transmission however, information about the qubit state is encoded in amplitude and phase, while in reflection the amplitude is constant, and the information is only encoded in the phase. The faint red blob represents a possible higher level, as can be measured in real transmon qubits with low anharmonicity for high drive power or increased sample temperature. The size of the Gaussian blobs is fundamentally limited by the number-phase uncertainty. For clarity the blobs are drawn unrealistically small, compared to our measurements.

resonator frequency and measure the phase signal, while the latter is usually applied for comparatively small dispersive shifts, compared to the linewidth.

The time for a successful readout is inversely proportional to the coupling rate $\Delta t_\mathrm{R} \propto 1/\kappa$. Its fidelity can be measured by the probability of falsely assigned states

$$F = 1 - P(e|g) - P(g|e)\,. \tag{3.32}$$

Here, $P(e|g)$ is the "false positive" probability to measure the qubit to be in state $|e\rangle$, while it was prepared in state $|g\rangle$. Any real qubit will be subject to decay, so the readout is a tradeoff. Longer data acquisition leads to a more accurate state extraction. However, shorter readout reduces the decay probability during readout, and the induced decay by the coupling, which is subject of the next section. The possible SNR depends on several factors, including the signal chain as is further discussed in Sec. 5.2.1. The coupling generating maximal phase space separation for readout at the bare resonator frequency is given by [106, 107]

$$\kappa_\mathrm{L} = 2\chi_\mathrm{eff}. \tag{3.33}$$

In Fig. 3.5, this corresponds to the largest possible phase separation of the blobs at $2\theta_\mathrm{t} = 90^\circ$ and $2\theta_\mathrm{r} = 180^\circ$, respectively. The readout projects the qubit onto one of its eigenstates and the corresponding observable $\hat{\sigma}_z$ commutes with the system Hamiltonian

Eq. (3.26). Therefore, repetitive readout gives the same result [2], which renders dispersive readout a so-called "quantum non-demolition" (QND) measurement [108, 109]. The phase information of the qubit however, is lost during measurement. This can be intuitively understood, as a projection onto the z-axis of the Bloch sphere, where no phase can be defined.

Under the influence of dissipation, the probability of a quantum transition from $|e\rangle$ to $|g\rangle$ is proportional to t^2 for short periods of time t. Thus, fast repetitive measurements can be used to reduce the decay probability. This is called the quantum Zeno effect [110] and has been observed in several systems, including flux qubits [18, 106]. A complete disruption of decay processes can not be achieved in this fashion, as this would require infinitely fast (and strong) measurements. For fast, repetitive measurements, quantum jumps can be observed [111, 112].

3.2.3 Purcell loss

Edward Mills Purcell discovered enhanced spontaneous emission for radiative transitions in atoms when inside a resonant cavity, compared to free space [113]. This can be intuitively understood as a manifestation of Fermi's golden rule, relating the transition rate to the density of possible final states. Following this argument, the radiation of a quantum system inside a cavity may also be suppressed, if the respective mode is not supported by the cavity [114]. Enhanced coherence times of qubits in 3D cavities can be attributed to the reduction of Purcell loss.

In the dispersive limit, the qubit state acquires a small photonic component, which may radiate out of the cavity. Assuming only the fundamental mode of the cavity to be close to the qubits frequency so higher modes can be neglected, the Purcell rate is given by [23]

$$\Gamma_\kappa = \frac{g^2}{\Delta^2}\kappa_\mathrm{L}, \tag{3.34}$$

with the total resonator loss rate κ_L, see Eq. (3.31). This can directly be seen in equation (3.29), as the qubits superposition has the probability $(g/\Delta)^2$ to be a cavity photon, which decays at the rate κ_L. In the resonant case the system is in an equal superposition state $|\pm, n\rangle$ (see Eq. (3.24)). Half of the time it is photon-like, thus the Purcell rate is

$$\tilde{\Gamma}_\kappa = \kappa_\mathrm{L}/2, \tag{3.35}$$

[2] Assuming the readout is fast compared to the qubits lifetime

in this case. In conjuncture with the previous chapter, it becomes clear that there is a tradeoff between maximizing the quality of the readout signal and reducing Purcell loss of the qubit.

4 Semiconducting Nanowires

To discuss the processes leading to charge transfer across a superconductor-semiconductor junction, we first need to have a look at the key properties of the materials involved. Further, the geometry and effective size of the junction compared to the characteristic length scales, like the coherence length ξ, play a crucial role for the leading physical effects. In this chapter, the relevant properties of superconductor-semiconductor interfaces are discussed, setting the basis for further discussion.

4.1 Superconductor-Semiconductor Junctions

The electronic properties of semiconductors are defined by the density of states (DOS) of their charge carriers close to the Fermi energy E_F. Electrical conductivity results from delocalized charge carriers that can freely transition between different states. This requires a partially filled band close to E_F in order to provide empty states to transition into. Semiconductors exhibit a band gap around E_F of ~ 0.1–$4\,\mathrm{eV}$, which is small enough that a significant amount of the states in the last filled (valence) band are thermally excited to the next higher (conduction) band at room temperature. An example of the corresponding band profile can be seen on the right sides of Figs. 4.1(a,b).

Most semiconductors form a depletion zone also called Schottky barrier, when in contact with a metal. The reason is the alignment of the respective Fermi levels. This can be understood intuitively, as the metals DOS is much higher at the Fermi energy. The resulting reduction of potential energy facilitates the valence electrons to migrate into the metal and metal electrons to fill empty states in the valence band. The resulting electric field created by the now ionized donors opposes the diffusion, it stops when an equilibrium is reached. The resulting change in carrier density can be included in the band model, by bending conduction and valence band up, locally changing their relation to E_F, see Fig. 4.1(a). The resulting theoretical barrier height Φ_B in the absence of surface states can be calculated by the Schottky-Mott rule [115] as

$$\Phi_B = \Phi_{\mathrm{metal}} - \chi_{\mathrm{semi}}, \tag{4.1}$$

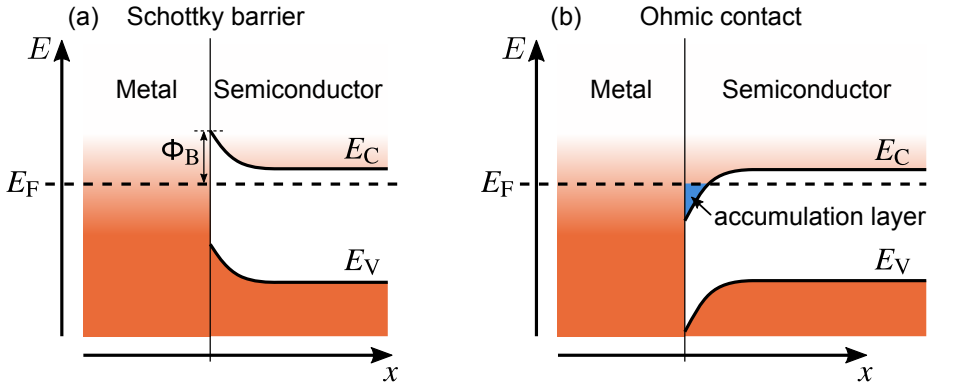

Figure 4.1: Schematic band profile of two semiconductor-metal interfaces forming a Schottky barrier (a), and an Ohmic contact (b). A Schottky barrier is common for most metal-semiconductor combinations and has diode characteristics. Due to its potential barrier, this type of contact is not suited as interface to a weak link for gatemon qubits. (b) shows an Ohmic contact as e.g. formed by InAs due to its high density of surface states. The blue region depicts a region of high charge carrier density. Close to the interface a so called two-dimensional electron gas (2DEG) can form.

with the metals work function Φ_{metal} and the ionization energy χ_{semi} of the semiconductor. Equation (4.1) ignores surface states and is therefore usually insufficient to describe real metal-semiconductor junctions.

Any surface interrupts the periodic potential of the bulk semiconductor. Thus, the DOS can differ strongly from the bulk band structure, which is defined by its periodicity. States which are inside the band gap and forbidden inside the material can exist on the surface [116]. This can be understood from a chemical point of view, where the surface atoms have free (dangling) bonds, that have different energy levels compared to the bulk. Dangling bonds are usually saturated by adsorption of external atoms or molecules, or by surface reconstruction. A second explanation considers the lattice potential, with a sudden boundary to vacuum. Bloch waves with an imaginary wave vector

$$\psi(\vec{r}) = e^{i(i\vec{k}\cdot\vec{r})}u(\vec{r}) = e^{-\vec{k}\cdot\vec{r}}u(\vec{r}), \tag{4.2}$$

which decay exponentially into the material and the vacuum, are relevant solutions at the surface. $u(\vec{r})$ has the periodicity of the crystal lattice. The amount and energy of these so-called surface states is strongly dependent on the semiconductor in question. Surface states can change the Fermi level near the surface. A high density of surface states causes so-called Fermi-level pinning and can even result in an inversion layer, creating an accumulation layer or a two-dimensional electron gas (2DEG), see Fig. 4.1(b). Surface states can be divided into intrinsic, originating from a well ordered clean surface, and extrinsic, which include the influence of defects, adsorbates or, interfaces with other materials [117].

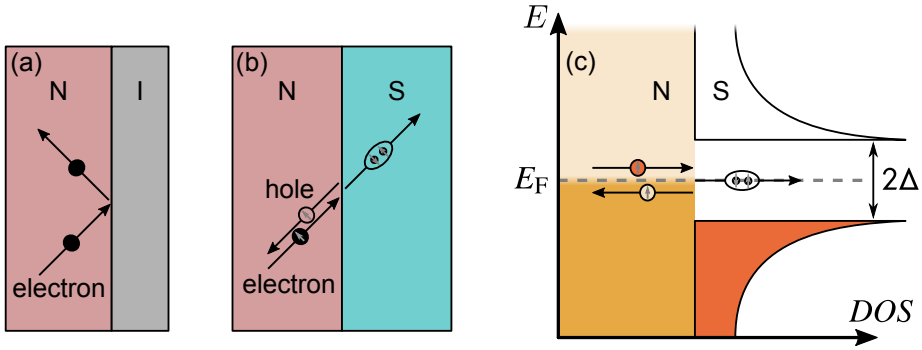

Figure 4.2: Schematic of normal and Andreev reflection on N-I and N-S interfaces in normal space (a,b) and in an energy band diagram (c). In this conversion process, which is treated as scattering, a normal current is converted into a current of Cooper pairs. The incident electron is retro-reflected (anti-parallel to its incoming vector) as a hole. The electron and hole depicted here have the same spin, because the spin of a hole actually denotes the absence of this spin.

Indium arsenide (InAs) is a III–V semiconductor, which exhibits a surface accumulation layer [118], increasing the tendency to form Ohmic (linear current-voltage characteristic) contacts with metals [86, 119, 120]. The schematic band profile of such a contact is shown in Fig. 4.1(b), it is a precondition for transparent contacts with possible application in gatemon qubits (see Sec. 2.8.2). Surface properties are especially important for nanowires (NWs), due to the high surface to volume ratio.
Besides forming an Ohmic contact with aluminum and niobium, InAs is chemically stable, and nanowires can be grown defect free by molecular beam epitaxy (MBE). Further, it was shown by Krogstrup *et al.* [121], that a domain-matched aluminum layer can be grown in situ on InAs nanowires, strongly increasing transparency and proximity effect (explained in the following). These properties render InAs the material of choice for weak links in gatemon qubits.

The proximity effect was first observed by R. Holm and W. Meissner [83, 122] in 1932. It describes the effect at junctions between a superconductor (S) and a normal (N) conductor, where the normal conductor inherits superconducting properties across small distances (on the order of the coherence length ξ). The critical temperature T_c of the superconductor is usually reduced close to the contact. The proximity effect (as well as the Josephson effect) can be understood in terms of Andreev reflections (AR) [123, 124].

In a normal conductor, charge transport is performed by individual electrons with energies in close proximity to the Fermi energy. These electrons can not enter a superconductor if their energy is within Δ of the Fermi energy. If we consider charge transport across a S-N boundary, it can be described as a scattering process. To satisfy charge conservation when creating a Cooper pair, a hole needs to be created as well, moving in the opposite direction

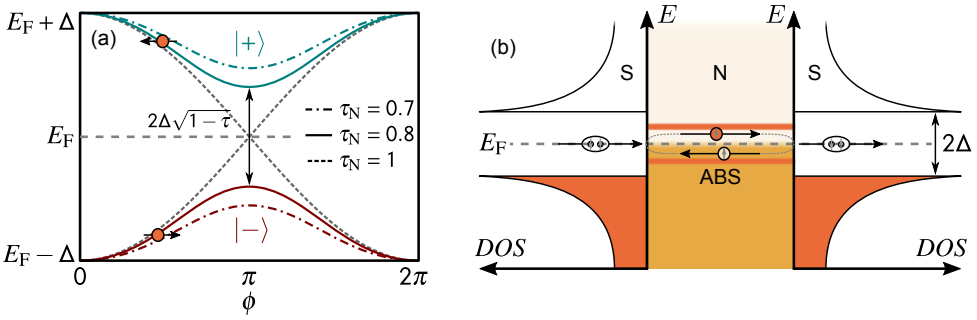

Figure 4.3: Energy spectrum and schematic of current flow by Andreev bound states (ABS). The phase dependent energy spectrum for different values of transmission probability τ_N is shown in (a). The two branches $|+\rangle$ and $|-\rangle$ (red and green), correspond to an effective current in different directions related to the phase difference. (b) depicts a sketch of coherent current flow through an S-N-S configuration by successive Andreev reflection, representing an ABS.

as the incoming electron [125]. This way, an effective charge of 2e is transferred for every AR, see Fig. 4.2(b,c). This type of reflection reverses all components of the incident vector and is called retro-reflection.

This reflection is phase-conserving, a reflected hole possesses information about the phase of the incident electron, the phase ϕ of the superconductor, and obtains an energy dependent phase shift of $\arccos(E/\Delta)$. If a weak link between two superconductors is shorter than the coherence length, a so-called Andreev bound state (ABS), restricted by the energy gap on both sides can emerge, see Fig. 4.3(b). A Josephson junction can be considered as two superconductors connected by a weak link with a single conduction channel of transmission probability τ_N. In this case, its coupling can be explained by a single pair of ABS [123, 124] with energy

$$E_{N\pm}(\phi, \tau_N) = \pm\Delta\sqrt{1 - \tau_N \sin^2 \frac{\phi}{2}}. \tag{4.3}$$

ϕ is the phase difference between the two superconductors, see Fig. 4.3(a) for a plot of the functional dependence for different transmission probabilities. For energies deep inside the superconducting gap, ABS are localized in the weak link, as indicated by Fig. 4.3(b).

Charge and phase are conjugate variables, hence the current across the nanowire for every occupied ABS can be calculated, using the canonical relation [126]

$$I_{ABS} = \frac{2e}{\hbar}\frac{dF}{d\phi} = \frac{2e}{\hbar}\frac{dE_\pm}{d\phi}, \tag{4.4}$$

with the free energy F. Plugging in the energy for a discrete bound state ($|+\rangle$ and $|-\rangle$), Eq. (4.3), we get the currents

$$\begin{aligned} I_{\mathrm{ABS}}^{|+\rangle} &= \frac{e\Delta}{2\hbar}\frac{\tau\sin\phi}{\sqrt{1-\tau\sin^2\phi/2}} \\ I_{\mathrm{ABS}}^{|-\rangle} &= -\frac{e\Delta}{2\hbar}\frac{\tau\sin\phi}{\sqrt{1-\tau\sin^2\phi/2}}. \end{aligned} \tag{4.5}$$

Apparently, these currents flow in opposite directions, as is indicated in Fig. 4.3(a). At zero temperature, only the lower state $|-\rangle$ is occupied, but for any finite temperature, the current flow consists of contributions from both levels. For longer junctions, the amount of states increases even further. If we consider the Fermi-Dirac distribution $f(E) = [1+\exp(E/k_{\mathrm{B}}T)]^{-}1$ between the states, the total current is changed by a factor of $[f(E_-) - f(E_+)]$ to

$$I_{\mathrm{ABS}} = \frac{e\Delta}{2\hbar}\frac{\tau\sin\phi}{\sqrt{1-\tau\sin^2\phi/2}}\tanh\left(\frac{\Delta}{2k_{\mathrm{B}}T}\sqrt{1-\tau\sin^2\phi/2}\right). \tag{4.6}$$

Considering the normal state conductance of the contact G_{N}, which can be described by the Landauer formula as a sum over all transmission channels with transmission coefficient τ_i

$$G_{\mathrm{N}} = \frac{2e^2}{h}\sum_{i=1}^{N}\tau_i. \tag{4.7}$$

If we describe the normal region of the weak link as a quantum point contact, with $\tau_i = 1$ for all channels up to N, the total current is

$$I(\phi) = G_{\mathrm{N}}\frac{\pi\Delta}{e}\tanh\left(\frac{\Delta}{2k\mathrm{B}T}\cos(\phi/2)\right). \tag{4.8}$$

However, for a tunnel junction with $\tau_i \ll 1$, the current transferred by ABS, given in Eq. (4.6) can be approximated to

$$I(\phi) = \frac{e\Delta}{2\hbar}\sum_{i=1}^{N}\tau_i\sin(\phi)\tanh\left(\frac{\Delta}{2k_{\mathrm{B}}T}\right). \tag{4.9}$$

This can also be expressed as the Ambegaokar-Baratoff formula [127]

$$I_{\mathrm{c}}R_{\mathrm{N}} = \frac{\pi\Delta}{2e}\tanh\left(\frac{\Delta}{2k_{\mathrm{B}}T}\right), \tag{4.10}$$

with the normal state resistance R_{N}, and the critical current I_{c}, defined as the maximum supercurrent across the junction ($\sin(\phi) = 1$). Considering Eq. (4.10), we can interpret

the voltage-gate tuning of the critical current as the effect of changing the normal state resistance R_N of the semiconductor weak link.

In a short junction ($L < \xi$), the supercurrent is transmitted by discrete ABS. With a junction length of approximately 100 nm, we may approach the short junction regime, depending on the purity of our samples [87]. The effective junction length also depends on the path of the charge carriers. In our case, the accumulation layer is on the surface of the NW and produces a cylindrical volume with a high DOS. Helical paths may have a significantly increased length, so the effective junction length is not well defined. Further, different sub-bands inside the accumulation layer may have different ABS, so the measured properties can differ significantly from our basic theoretical model.

For our gatemon design we use InAs nanowires, which are coated with aluminum on one side, we call this half shell. For sufficiently transparent contacts, an applied gate voltage V_g changes the Josephson energy E_J in two ways. A gate voltage changes the Fermi energy, directly modifying the number of transmission channels [128]. Further, the transmission probability τ_N of existing channels is changed [89, 129]. This variation in the spectrum of ABS is directly connected to the induced change in coherence length.

4.2 Sample Fabrication

Most of the fabrication for the gatemon samples was realized in the cleanroom facilities of our collaborators at Jülich Research Centre by Patrick Zellekens. In the following, a short description of the fabrication process is given.

In a first step, the InAs nanowires with a diameter of approximately 90 nm are grown. This can be achieved by vapor-liquid-solid growth [130], using a gold droplet as catalyst, or self-catalyzed by selective-area MBE. We use the latter method, where the NWs grow out of holes in a pre-patterned silicon oxide (SiO_2) mask on a Si(111) substrate. Figure 4.4 (a) shows a square of InAs NWs, grown in this manner. While still on the substrate, a half shell of aluminum (Al) is deposited onto the nanowires, to increase the contact transparency. This is done via MBE to ensure epitaxial growth and reduce stress-induced surface defects. The junction is later defined by etching away a small part of the Al shell.

Prior to positioning of the NWs, all CPW structures (see Sec. 3.1.1), including the transmission line, resonators, gates and ground plane are structured. We use intrinsic silicon(100) with a bulk resistivity of $\rho > 80\,\mathrm{k\Omega\,cm}$ at room temperature. In this electron-beam lithography (EBL) process, transmission line and resonators are structured by a lift-off process from 90 nm TiN. The bottom gate electrodes are made of a stack of 10 nm titanium (Ti) and platinum (Pt), respectively, while the longer gate lines and bond pads are

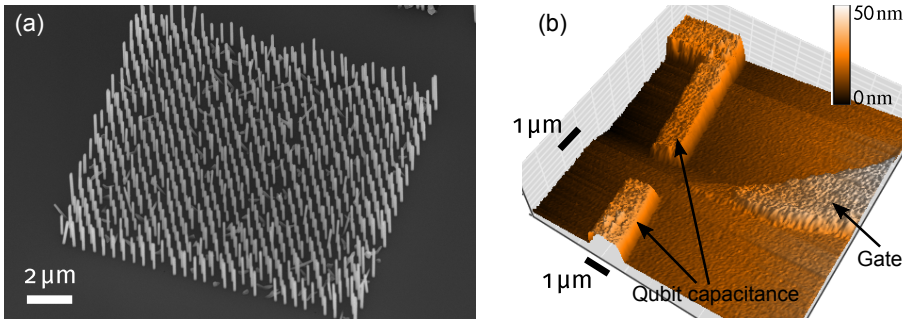

Figure 4.4: (a) Scanning electron micrograph of InAs NWs grown in a square pattern. The picture (b) was generated by an atomic force microscope (AFM) and shows the area where the nanowire is placed in a gatemon qubit. AFM microscopy was used to calibrate the exact height of the deposited films and the etch rate of the aluminum half shell around the NWs. The height of the metal film representing the qubit capacitance was 25 nm in this test.

30 nm Ti and 130 nm Pt. The Ti layers are needed as adhesion enhancement. The complete process parameters can be found in appendix C.

In the next step, the NWs have to be transferred onto the chip. This is achieved by a variation of the micro manipulation procedure, developed by MØlhaven *et al.* [131]. To position the NWs, an etched tungsten (W) tip is used and coated with a sheet of indium (In) to optimize its adhesion properties. The positioning is supported by a scanning electron microscope (SEM), for visual feedback, and guided by markers deposited during gate deposition. An example of this positioning process is shown in Fig. 4.5(f), showing a false-colored picture from the perspective of the guiding SEM. After positioning, the NW are held in place by van der Waals forces. These are strong enough, to fix the NW during spin coating and argon plasma cleaning. For side gates, the absolute position of the NW with respect to the gate electrode may vary from sample to sample on the order of several hundred nanometers. This changes the field strength at the NW for a given gate voltage V_g and thus, the effectiveness of the gate varies between samples. In the newer bottom gate design, the spacing between gate and NW is defined by the dielectric (HfO_2) layer, as depicted in Fig. 4.5(a-d). The necessary gate voltages could be lowered roughly by a factor of 10, using bottom gates (see Sec. 6.2).

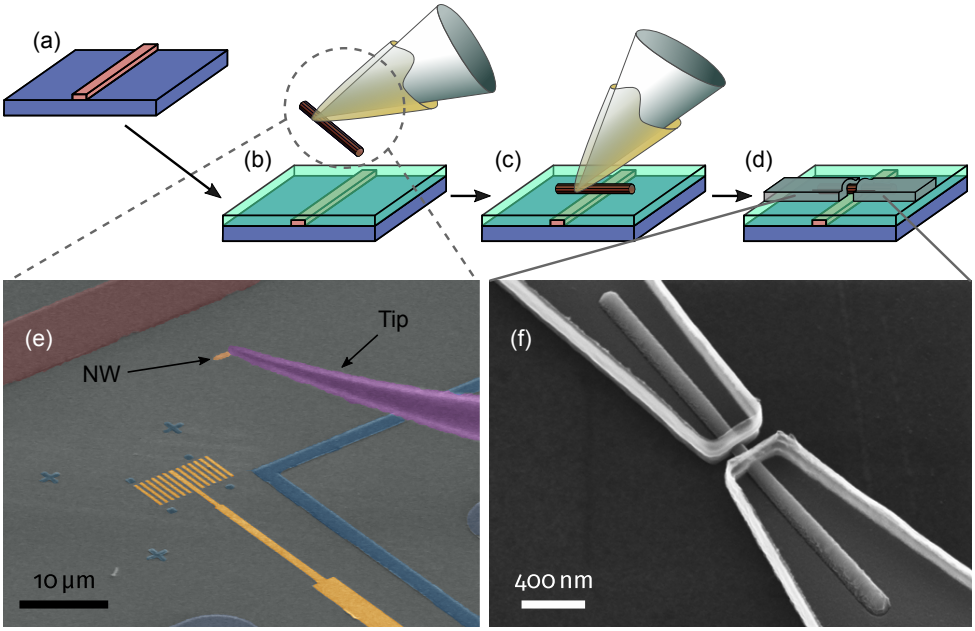

Figure 4.5: Simplified sketch of the fabrication procedure. (a) The gate electrode (Ti/Pt) is produced by EBL. (b) 15 nm of HfO_2 dielectric is deposited onto the sample, while the indium coated tungsten tip is used to handle the NW. (c) The NW is positioned across the gate, thereafter strong adhesive forces ensure its position to stay fixed. (d) In a next EBL step, the superconducting leads are structured. An SEM picture of a contacted NW to visualize this step is shown in (f), the leads are aluminum in this case and appear transparent. (e) shows the view of the guiding SEM while positioning a NW. The picture is false-colored for visibility. The tip with an attached NW, the gate structure, and positioning markers can be seen in this test.

The following steps are used to contact the NW by the qubit capacitance and to define the weak link:

1. Spin coat with a single layer of PMMA 950K at 5000 rpm for 50 s
2. Bake for 7 minutes at 150 °C
3. Ebeam lithography of the qubit design
4. Development with IPA:MIBK 2:1
5. Cleaning with Ar for 80 s
6. Deposition of 80 nm of NbTi
7. Liftoff with heated NMP for 2 h at 50 °C
8. Cleaning in ACE and IPA

9. Repeat steps 1 and 2
10. Ebeam lithography of the junction section
11. Development with IPA:MIBK 2:1
12. Etch of the Al shell in Transene-D[1] for 15 s (15 nm thickness) at 60 °C, stop etch in warm DI water for 30 s, clean in DI water for 30 s at room temperature
13. Liftoff with heated NMP for 2 h at 50 °C

The junctions fabricated in this fashion are approximately 110 nm long, mainly limited by the lateral etching of Transene-D. In a new technique, which is under development, we use one NW as a mask for a second one during aluminum deposition. This removes the etching process and ensures well defined and reproducible junction width. This way, junctions of 40 nm can be fabricated, limited by the diameter of the mask NW. A thorough description of the fabrication process can be found in the PhD thesis of P. Zellekens [132].

[1] https://transene.com/aluminum/

5 Experimental Setup and Methods

Due to their very nature, qubits need to be shielded from the noisy laboratory environment. More precisely this means that no unwanted interactions of the quantum system in question with the environment may change the quantum state prior to measurement. For solid-state qubits with transition frequencies on the order of $1-20\,\mathrm{GHz}$, the temperature of the sample needs to be low enough to render thermally induced state transitions unlikely on the timescale of single experiments. Hence the need for millikelvin temperatures. In chapter 3, the interaction between resonator and qubit is presented. Here, we adapt these considerations to built a circuit containing gatemon qubits, which are coupled to readout resonators and a transmission line. Further, the sample has to be electromagnetically shielded and the measurement electronics have to provide a noise level low enough not to affect the quantum state to be measured. In the following the sample design, and the measurement setup, namely the microwave electronics and the working principle of dilution refrigerators, are described.

5.1 Cryogenic Setup

To operate a dilution refrigerator manually, a thorough understanding of the working principle is necessary. The presented measurements are mostly carried out in two kinds of $^3\mathrm{He}/^4\mathrm{He}$ dilution refrigerators, so-called 'wet' or 'dry'. Here 'wet' means that cryogenic liquids, namely nitrogen and helium provide the primary cooling by evaporation. Thus, these liquids have to be refilled repeatedly from the outside. In 'dry' or cryogen-free cryostats, the working gas is precooled by a compressor-powered pulse-tube refrigerator and a Joule-Thomson cooler. The advantage of wet systems are no moving parts near the low-temperature section and therefore less vibrations during operation. For fast test measurements at 4.2 K, so-called dip-sticks are used, which are sample holders that can be directly inserted into a dewar of liquid helium.

The basic working principle of the $^3\mathrm{He}/^4\mathrm{He}$ mixture is the same for both types, based on the heat of mixing of the two Helium isotopes, as depicted in Figure 5.1. The cryostat

reaches its base temperature of about $10-20\,\mathrm{mK}$ in several steps from top to bottom. The working gas is a mixture of the two helium isotopes ^{3}He and ^{4}He. It undergoes a spontaneous phase transition into a ^{3}He-rich, and a ^{3}He-poor phase, called concentrated and dilute phase respectively when cooled below approximately 870 mK. The circulated part is almost pure ^{3}He, because of its higher partial pressure. The helium mixture follows a closed cycle depicted in Figure 5.1.

After purification by passing through cold traps filled with liquid Nitrogen at 77 K and liquid Helium at 4.2 K (not shown in Fig. 5.1), the ^{3}He enters the cryostat at a pressure of about 500 mbar. In contact with the 1K bath, the gas is precooled and liquefied at about 1.5 K, removing the heat of condensation. Subsequently, it enters the main impedance and a heat exchanger in thermal contact with the still, cooling it to about 600 mK. Thereafter it passes through the secondary impedance and a counterflow heat exchanger, cooling it further by the upward flow of ^{3}He from the base plate.

Entering the mixing chamber, the pure ^{3}He is added above the phase boundary separating the concentrated phase of almost pure ^{3}He and the dilute phase (93.4% ^{4}He and 6.6% ^{3}He). Due to its much higher partial pressure at 600 mK, the gas evaporated in the still is almost pure ^{3}He. This shifts the ratio of isotopes in the diluted phase away from equilibrium, creating an osmotic pressure. The resulting endothermic dilution of ^{3}He passing through the phase boundary causes the desired cooling of the mixing chamber.

The rate of ^{3}He evaporation in the still depends on its temperature. Therefore it is possible to increase the cooling power by heating the still and thus increase the flow of ^{3}He through the phase boundary. After the still, the gas exits the cryostat and enters the ^{3}He-Pump, after which the cycle starts again. To reduce heat exchange by thermal radiation, aluminized polyester foil interleaved with polyester, so-called "superinsulation foil" is wrapped around all internal stages, except the base. Our cryostat was thermally stable within $\Delta T \leq 1\,\mathrm{mK}$ at base temperatures of 15 to 30 mK.

Faster cooldown-cycle times can be achieved by adiabatic demagnetization refrigerators (ADR) or dipstick-style refrigerators. The latter have been used for quick test measurements. ADR cryostats usually work in cycles and make use of the magnetocaloric effect as secondary cooling. Magnetization of a magnetocaloric substance reduces its entropy and heat capacity by aligning its magnetic dipoles. Energy conservation causes the substance to heat up. This heat is removed by contact with the primary coolant, e.g. a pulse tube cryocooler. Subsequent demagnetization in contact with the sample increases the entropy of the magnetic dipoles and reduces the temperature, effectively cooling the sample. The alternating thermal contact is realized by heat switches. Once the temperatures of sample and coolant equalize, the cycle is repeated.

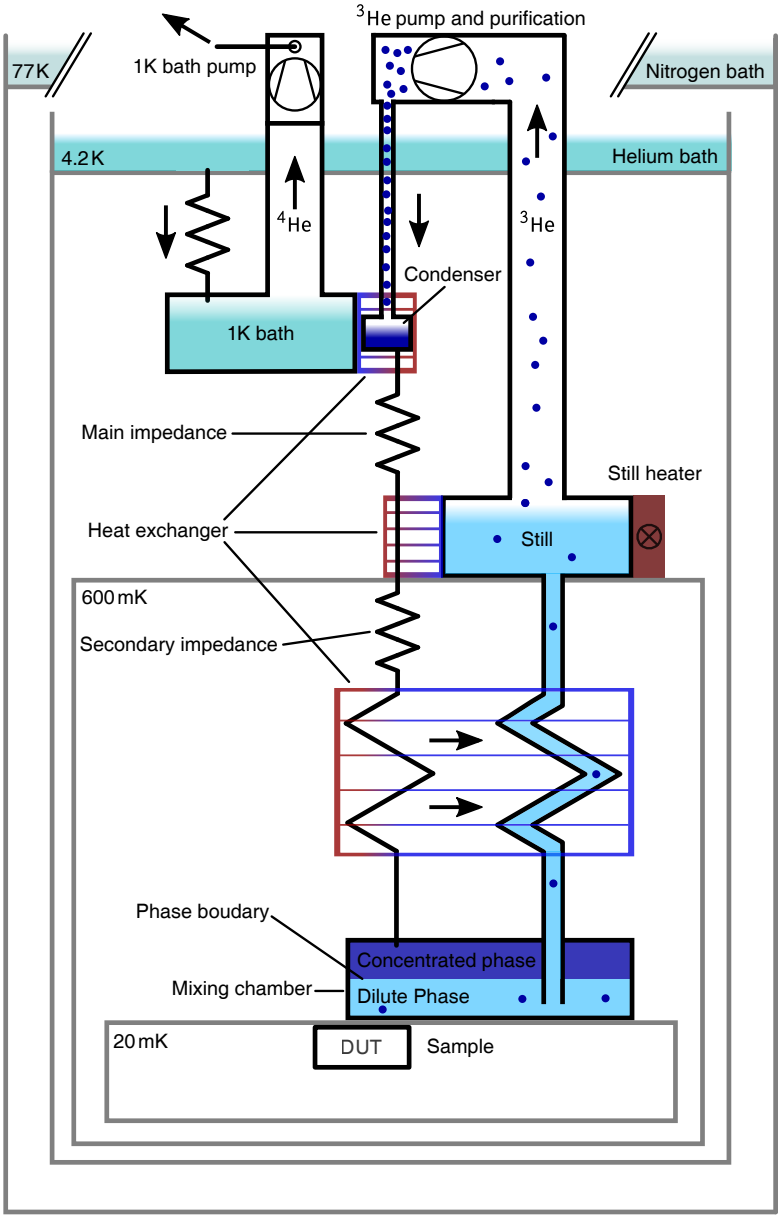

Figure 5.1: Schematic diagram of a ^{3}He/^{4}He dilution refrigerator, as used in the presented experiments (except the outer vacuum jacket). Temperatures well below thermal excitation of the examined qubit are a precondition for qubit measurements. The base temperature below 20 mK is ensured by endothermic dilution of ^{3}He passing through a phase boundary in the mixing chamber. Samples (DUT) are in thermal contact with the mixing chamber. ^{3}He is continuously cycled through the cryostat. A description of the complete cooling cycle can be found in the text.

5.2 Microwave Setup and Measurement Technique

The time resolution necessary to characterize energy relaxation and dephasing are set by the qubits' parameters and are usually in the microsecond range. However, the possible gate times for the discussed samples are tens of nanoseconds. Thus, the used electronics need a time resolution according to the correct sampling of the shortest pulses. In the following, the electronics used for spectroscopic and time resolved analysis of the samples are discussed.
In the previous section, the considerable efforts to ensure a sufficiently cold environment for solid-state qubits are depicted. Besides the thermal radiation, the electromagnetic environment of the microwave signal chain constitutes a large part of the dissipative bath discussed in 2.3. The noise level at the sample needs to be low enough to perform qubit measurements and the conditions for dispersive readout have to be met (see Sec. 3.2.2).

5.2.1 Cryogenic Signal Chain

Considering the bandwidth of a typical readout resonator to be on the order of 10 MHz, the noise power of room-temperature electronics in this band is about $P_\mathrm{n} = 4 \cdot 10^{-14}\,\mathrm{W}$. For comparison, the signal of a typical readout resonator is on the order of

$$P_\mathrm{sig} = \hbar\omega_\mathrm{r}\kappa \approx 1 \cdot 10^{-20}\,\mathrm{W}, \tag{5.1}$$

in the single photon regime. Without attenuation, the noise power of the room temperature impedance is more than five orders of magnitude larger than the signal of a typical measurement. Our microwave setup needs to reduce the effect of room-temperature electronics on the sample in order to observe coherent quantum states.

Throughout all experiments, 50 Ω impedance, coaxial microwave cables are used. Their material is selected according to the particular position, and is generally a trade-off between loss, thermal conductivity and mechanical properties like bending radius or thermal expansion. Between different temperature-stages, stainless steel wires are implemented, which have a low thermal conductivity but also increased loss. This is not a problem, as the thermal noise inherent to any conductor at room temperature needs to be heavily attenuated in order to enable single photon experiments. The power spectral density of Johnson–Nyquist noise for a resistor R at temperature T is [133]

$$\left\langle v_T^2 \right\rangle = 4k_\mathrm{B}TR \tag{5.2}$$

with the mean squared noise voltage per hertz $\left\langle v_T^2 \right\rangle / \sqrt{\mathrm{Hz}}$. The related noise power in the frequency bandwidth Δf is

$$P_\mathrm{n} = k_\mathrm{B}T\Delta f. \tag{5.3}$$

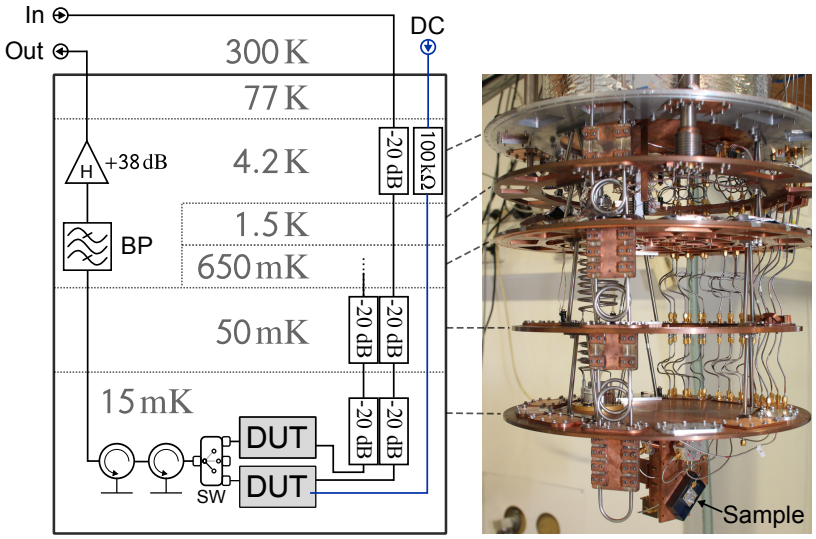

Figure 5.2: Schematic of the signal wiring inside the dilution refrigerator. To the right, a photograph of the opened cryostat is shown, dotted lines connect the thermal stages in the sketch with its real counterparts. Following the signal path from the input port "In", the microwave signal is repeatedly attenuated to reduce thermal noise, the overall cable loss is about 10 dB. Each sample has its individual input line, for clarity only one is drawn completely. After passing through the respective sample "DUT", a microwave switch "SW" enables different samples to be measured using the same amplifier line. Two circulators are used to isolate the sample from backwards radiation of the HEMT amplifier "H". A band-pass filter "BP" is used to suppress noise outside the amplifier bandwidth, usually between 4 and 16 GHz.

To account for thermal noise, the signal to the sample is repeatedly attenuated with resistors at ever lower temperatures as is shown in Fig. 5.2. Every attenuator of 20 dB dissipates 99 % of the incoming signal. Thus, the first attenuator dissipates the largest amount of heat. It is installed at 4.2 K, because this stage is cooled by liquid helium and can dissipate high thermal loads. It is important to keep the load on every stage well below the respective cooling power.

The attenuation is also beneficial to the signal-to-noise (SNR) ratio of the incoming signal, as the room temperature electronics can not easily reduce its own thermal noise, but an increase in signal strength is feasible. This stronger signal is damped by the cold attenuators, equally reducing the signal and the thermal noise, while adding thermal noise of its own temperature. For ideal components the resulting noise temperature T_n seen by the sample is only slightly higher than the base temperature $T_\mathrm{Base} = 15\,\mathrm{mK}$

$$T_\mathrm{n} = 15\,\mathrm{mK} + 50\,\mathrm{mK}\cdot \mathrm{A}_1 + 4.2\,\mathrm{K}\cdot \mathrm{A}_1\mathrm{G}_2 + 300\,\mathrm{K}\cdot \mathrm{A}_1\mathrm{A}_2\mathrm{A}_3 = 16.2\,\mathrm{mK} \qquad (5.4)$$

with the attenuation factors $\mathrm{A}_{1,2,3} = -20\,\mathrm{dB} = 1/100$. For real attenuators, the thermalization of the electronic bath is difficult at millikelvin temperatures, since the electron-phonon

scattering scales with T^5 for small temperatures well below the Debeye temperature $T \ll \Theta_D$ [134]. The number of thermal noise photons per signal photon at the sample is still below 0.002 for our setup [135].

For an amplifier chain, the equivalent noise temperature is given by Friis' formula [136]

$$T_{\mathrm{Sig}} = T_1 + \frac{T_2}{G_1} + \frac{T_3}{G_1 \cdot G_2} + \ldots \tag{5.5}$$

if the gain of the first stage G_1 is sufficiently high, the first amplifier dominates the noise temperature. This is the reason why the first amplifier usually has the strongest impact on the signal, and quantum limited amplifiers [137] like Josephson parametric amplifiers should always be the first amplifier in the chain. In our case, the first amplifiers are high-electron-mobility transistor (HEMT) amplifiers[1] with gains of $G_1 \approx 40\,\mathrm{dB}$ and an equivalent noise temperature of 2–6 K, denoted "H" in figure 5.2. Due to the large gain, the equivalent noise temperature of the signal chain is approximately the noise temperature of the respective HEMT. For a typical noise temperature on the order of 10 K, the SNR in the single photon regime is on the order of 0.1, ten noise photons for any signal photon. A band-pass filter "BP" protects the HEMT from DC-voltage and noise outside its usable bandwidth, usually between 4 and 16 GHz. As any attenuation of the signal emitted from the sample erases information, superconducting coaxial wires are implemented between base and HEMT. These provide low loss and low thermal conductivity. A microwave switch[2] "SW" enables different samples to be measured, by connecting them to the same amplifier line.

5.2.2 Spectroscopy and Time-Domain Setup

Generally, we distinguish spectroscopic and time-domain measurements, because of the specific demands on the electronics. The spectroscopic setup enables to extract the steady-state response of the sample with respect to microwave frequency, microwave power, gate voltage, or the parameters of a second microwave tone. The time-domain setup allows time-resolved measurement of the qubit state.

The room temperature setup used in this work is depicted in Fig. 5.3. Two possible arrangements for either spectroscopy (red box) or time-resolved measurements (gray boxes) are possible. Components framed by the green box are common to both setups.

[1] Mainly two models of amplifiers by the brand "Low Noise Factory" are used: "LNF-LNC4_16A s/n 013B" and "LNF-LNC4_8C s/n 200A", see `www.lownoisefactory.com`

[2] We use two microwave switches, one 4-port (Radiall r591-762-400) and one 2-port (Radiall r572-432-000), see `www.radiall.com`

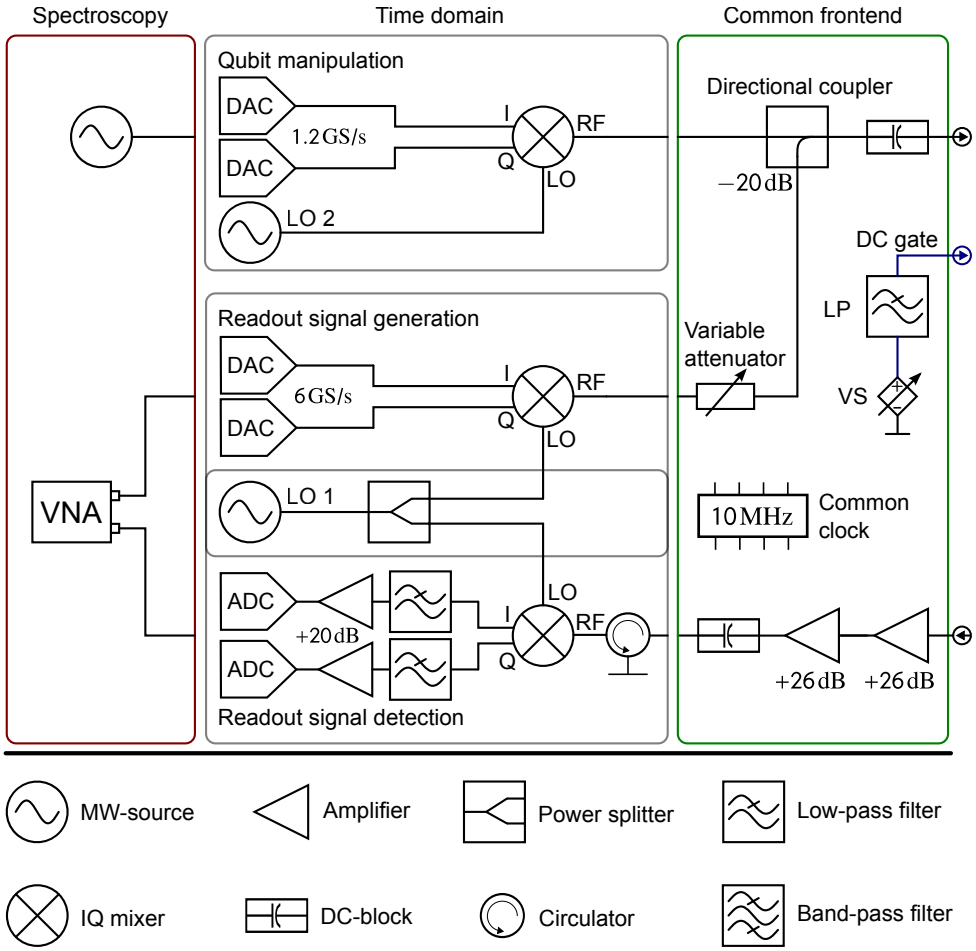

Figure 5.3: Schematic of the microwave setups at room temperature. Two possible signal paths for either spectroscopy (red box) or time domain (gray boxes) experiments are depicted. The components used in both setups are drawn in the green box on the right. For spectroscopy, the amplitude and phase of the signal passing through the sample is directly measured by a vector network analyzer (VNA). In this setup, the steady-state response of the sample with respect to microwave frequency, microwave power, gate voltage, or the parameters of a second microwave tone can be measured. For time-resolved measurements, readout and manipulation tones are modulated in IQ mixers via frequency conversion. The local oscillators (LO 1 and LO 2) are in the GHz-range, close to the resonator or qubit frequency, respectively. Digital-to-analog converters (DAC) provide the appropriate quadrature components in the MHz-range, also called baseband, to produce the desired pulse shape. All phase-sensitive components are phase-locked by a common 10 MHz Rubidium clock. The cryostat is galvanically isolated from the microwave equipment by DC-blocks, while the DC gate is battery-powered and connected by an optical fiber.

Spectroscopic measurements are performed using a conventional vector network analyzer (VNA), which can derive the complex scattering matrix. A microwave source[3] provides a secondary tone. Both signals are combined by a directional coupler, which selectively attenuates the VNA signal. This reduction of the readout signal compared to manipulation is needed, because the signal to the qubit is filtered by the resonator. Therefore the manipulation tone, which is off-resonant, needs to have a larger amplitude. Due to its higher measurement speed and dynamic range, the spectroscopy setup is typically used for sample characterization except for time-resolved measurements. The cryostat is galvanically isolated by DC-blocks from all microwave parts powered by mains supply. The voltage source "VS" for the DC gate and the power supply for the 26 dB room temperature amplifiers are isolated and grounded to the cryostat.

Time domain measurements are realized using a heterodyning technique. This means the signal is generated by a mixer, modulating a base band signal (LO), close to the desired frequency (ω_q or ω_r), with an envelope at lower frequency. The envelope is generated by fast digital-to-analog converters[4] (DAC), which generate the in-phase "I" and the quadrature "Q" component of the manipulation or readout pulses in the respective baseband of $30-50\,\mathrm{MHz}$. IQ mixers are driven as single-sideband modulators and mix these signals with the constant high frequency output of microwave sources called local oscillator "LO1" and "LO2". The frequencies are such, that the signal gets up-converted to the resonator or qubit frequencies

$$\omega_{\mathrm{DAC}} + \omega_{\mathrm{LO1}} = \omega_r \qquad \text{and} \qquad \omega_{\mathrm{DAC}} + \omega_{\mathrm{LO2}} = \omega_q. \tag{5.6}$$

The state of the qubit is encoded in the frequency shift of the readout resonator and thus in the amplitude and phase of the signal at ω_r. To extract this information, the returning signal gets down-converted with the same local oscillator used for the up-conversion ω_{LO2}, yielding the demodulated baseband signal. After low pass filtering to suppress leakage of the carrier frequency and further amplification, the signal is digitized by an analog-to-digital (ADC) converter card with a sampling rate of 500 MHz in the measurement PC. A Fourier transformation of the incoming signal for both quadratures gives the complex scattering parameter and in the case of dispersive readout, the state of the qubit. Phase stability in time and between components is maintained by a common 10 MHz reference clock[5]. Due to the poor signal-to-noise ratio (SNR), averaging of usually between 200 to 1000 single traces directly on the ADC-card is necessary to yield a sufficient signal after Fourier transformation. To extract coherence parameters for instance, traces containing several

[3] MWSRC

[4] For qubit manipulation we use a 10 bit, 6 GS/s Tektronix AWG7062B AWG, for readout a 14 bit 1.25 GS/s Tarbor WX1284C AWG

[5] The frequency standard used is a FS725 from Stanford Research Systems, see `https://www.thinksrs.com`

points are averaged during post-processing to ensure confident fits. The exact procedure is explained in section 5.2.3.

Heterodyne readout combines several advantages compared to for instance fast switching of the microwave sources at qubit and resonator frequency. Due to the mixing, the leakage of microwave power into the system in times of free evolution is extremely low, as the microwaves are detuned from the qubit or resonator frequency. Further, for multiple readout resonators, a single microwave source is sufficient, as all frequencies within the bandwidth of the DAC can be generated in a single pulse. For readout, pulses between 200 ns and 400 ns are used.

5.2.3 Interleaved Measurements

The majority of literature on qubits treats their coherence parameters as constants varying between devices and cooldowns, dependent on variable external parameters like probe power or temperature. During the course of this work however, it became evident, that intrinsic temporal fluctuations of qubit parameters are omnipresent. In low-SNR experiments, fast fluctuations may be masked due to the needed averaging described in the previous section. When qubit parameters are measured consecutively, inconsistencies as for instance $T_2^{\mathrm{R}} > 2T_1$ are possible due to fluctuations during the measurement sequence. In this work, a time-multiplexed pulse sequence pattern has been developed and employed, which allowed us to acquire all qubit parameters simultaneously. One large benefit of this technique is that the averaging can be defined during analysis (down to the threshold set by the repetition rate), to match the intended time resolution and SNR.

In Fig. 5.4, a sketch of the pulse sequence pattern (a) and the corresponding signal (b) are depicted. Here the sequence is as follows: single points for energy relaxation T_1, Ramsey dephasing T_2^{R}, and spin echo T_2^{E} coherence times are taken for every value of the free evolution time Δt, starting with $\Delta t = 0$. In this way, all three curves in (b) are formed simultaneously from left to right. After sorting the points T_1, T_2^{R}, T_2^{E} coherence times, as well as the Ramsey detuning frequency $\Delta\omega_{\mathrm{q}}$ can be extracted from fits to the respective functions. The expected state evolution is

$$P\left|1\right\rangle(t) \propto A_0\, e^{-\Delta t/T_1} + B, \tag{5.7}$$

$$P\left|1\right\rangle(t) \propto 0.5A_0 \left(1 - e^{-\Delta t/T_2^{\mathrm{E}}}\right) + B, \tag{5.8}$$

$$P\left|1\right\rangle(t) \propto 0.5A_0 \cos\left(2\pi\Delta\omega_{\mathrm{q}}\Delta t\right) \left(1 - e^{-\Delta t/T_2}\right) + B, \tag{5.9}$$

for energy relaxation, spin echo, and Ramsey measurements, respectively. Here, A_0 is the initial envelope amplitude, and B is the final population, including thermal population.

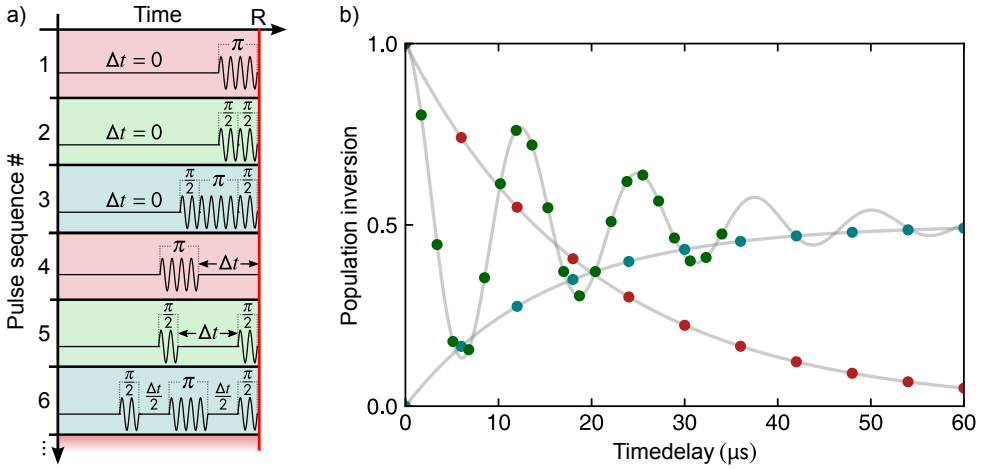

Figure 5.4: (a) Measurement pattern: Single pulse sequences of different measurements, here T_1, T_2^{R} and T_2^{E}, are interleaved, resulting in a simultaneous data acquisition. The time Δt is the free evolution. The red line depicts the readout labeled "R". The ratio between the number of pulses is usually not 1:1:1, as exponential functions require less points for accurate fitting, than a sinusoidal. On the right, (b) shows the corresponding ideal traces with fits for the functions given in equations (5.7) - (5.9). The fit parameters allow extraction of T_1 (red), T_2^{R} and the Ramsey detuning $\Delta\omega_{\mathrm{q}}$ (green) and T_2^{E} (cyan).

In this scheme the averaging is done per trace rather than per point, such that the pulse sequence shown in Fig. 5.4(a) is repeated until the intended minimal SNR is reached. Here we use that the our dephasing noise is short-correlated (e.g. white). This is well supported by almost perfect exponential decay in Ramsey measurements, see Fig. 5.5 for an exemplary trace. This is interesting, because we show in Sec. 6.1.2, that the low frequency part of our frequency noise spectrum resembles $1/f$. The mean-squared phase noise $\langle \delta\phi^2(t) \rangle$ depends on the spectral noise density $S_\lambda(\omega)$ for the noise source λ as

$$\langle \delta\phi^2(t) \rangle = \left(\frac{\mathrm{d}\omega_{\mathrm{q}}}{\mathrm{d}\lambda} \right)^2 \int_0^\infty \mathrm{d}\omega S_\lambda(\omega) W(\omega,t). \tag{5.10}$$

Here $W(\omega,t)$ is a weight function, to include the sensitivity of the related experiment to different parts of the frequency spectrum. $\mathrm{d}\omega_{\mathrm{q}}/\mathrm{d}\lambda$ describes the qubits sensitivity to the noise source λ. In the case of a Ramsey sequence, the weight function is

$$W_{\mathrm{R}}(\omega,t) = \frac{\sin^2(1/2\omega t)}{(1/2\omega)^2}. \tag{5.11}$$

This renders a Ramsey measurement sensitive, to the full noise spectrum. For large noise amplitude at low frequencies ($\omega \approx 0$), a non-exponential decay is expected. This kind of noise corresponds to a slow drift in ω_{q}, leading to averaging over several different frequencies in a Ramsey measurement. For long-term measurements on the order of

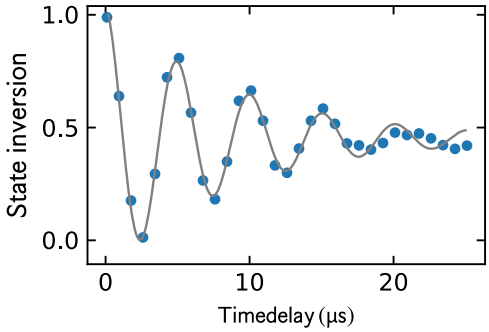

Figure 5.5: Exemplary Ramsey measurement, fitted with Eq. 5.9. A single exponential fits the envelope accurately. This indicates short correlated phase noise as dominant noise source for dephasing.

days, we see only small drifts in qubit frequency, see e.g. appendix Fig. A.5(a). These observations indicate that the relative amplitude of low frequency fluctuations seems to be negligible for the qubit dephasing in our case.

From the fit results, the derived values of the exact qubit frequency ω_q and the pure dephasing T_ϕ can be calculated. Theoretically it would be possible, to continue the sequence for the complete measurement duration and divide the resulting data as needed in post-processing. However, this approach is very demanding on the speed, stability and data handling of the measurement back-end and thus, not practical for our hardware. A newer version of the presented time-domain setup (see Sec. 5.2.2), based on a field-programmable gate array (FPGA) could be used in such a way.

Results of an exemplary measurement using the presented sequence, can be seen in chapter 6 (Fig. 6.1). It becomes apparent that single coherence times are an incomplete metric for the qubit's performance. The variance and Allan variance [21, 138] could for example be used, to describe the spread in relaxation and dephasing rates, as well as the frequency stability of a specific qubit.

5.3 Sample Design

This work discusses the coherence and parameter fluctuations in superconducting qubits, a detailed discussion follows in chapter 6. The majority of measurements have been executed using a non-tunable transmon qubit. The related sample was fabricated in the group of David P. Pappas at the NIST institute in Boulder, Colorado. The comparison of different qubit types or fabrication techniques regarding parameter stability could yield new insights on the factors limiting many-qubit processors. Hence, one part of my work was dedicated to build a qubit based on a semiconducting nanowire junction also called "gatemon" (see section 2.8.2). This project was a collaboration with the Forschungszentrum Jülich (FZJ), where the surface structuring, positioning, and contacting of the nanowire was carried out by Patrick Zellekens. Further details about these processes can be found in his PhD thesis [132]. The chip and sample box design for the gatemon qubit is part of my work and is discussed in the following.

5.3.1 Circuit Design

As discussed in chapter 3, the circuit design needs to meet the following criteria:

- A feedline matched to the characteristic line impedance Z_0 to avoid reflections
- Resonator frequencies that enable dispersive readout
- No parasitic modes close to the resonator or qubit frequencies to minimize Purcell loss
- Sufficient isolation of different qubits to avoid crosstalk
- Coupling capacitances between feedline, resonator, and qubit that allow dispersive readout of the qubit state without dominating its radiative loss
- The possibility to apply an electrostatic gate to the junction, without limiting the qubit lifetime by Purcell loss
- A shunt capacitance resulting in the desired qubit frequency and E_J/E_C ratio for the given range of critical currents I_c

As shown in Sec. 3.2, the dispersive shift is given by $\chi = g^2/\Delta$, while the Purcell loss rate in the dispersive limit is given by $\Gamma_\kappa = \kappa_L g^2/\Delta^2$. Good starting points for the design are the intended frequencies of qubit and resonator pairs. In this case, we had to account for chip size restrictions of approximately $6 \times 6\,\mathrm{mm}$ and the bandwidth of our microwave setup from $4-8\,\mathrm{GHz}$ and $8-12\,\mathrm{GHz}$. The chosen frequency range of the resonators is

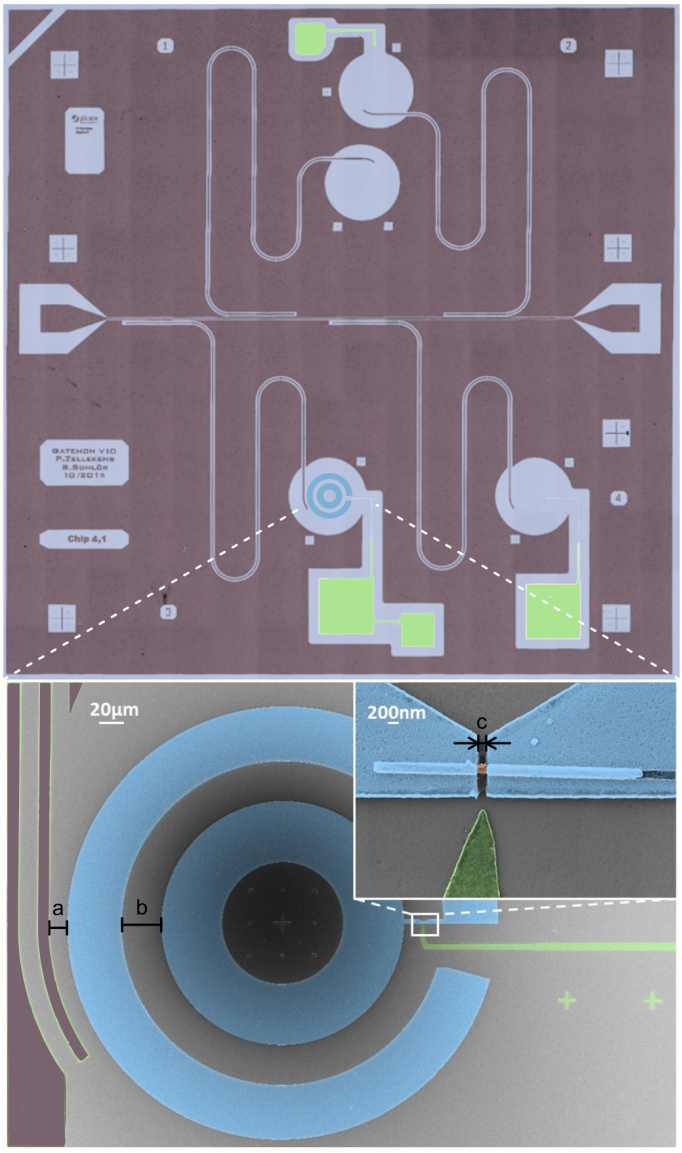

Figure 5.6: False-colored micrographs of a sample chip (silicon substrate), containing four resonators and gatemon qubits. A laser scanning microscope picture of the whole chip (6×6 mm) can be seen on top, with the qubit capacitances not yet fabricated. To clarify the orientation and size, the layout of one qubit was artificially added in blue. On the bottom, a zoomed in view of a finished chip taken with a scanning electron microscope is shown. The inset depicts a further zoom-in, where the InAs nanowire junction and the side-gate can be seen. So-called "bottom gates", extending below the nanowire have also been used. For this chip, three of the qubits have electric gates (green), one was left without gate structure, to investigate the amount of Purcell loss caused by the gate. The distances denoted "a, b, c" are used to tune the qubit-resonator coupling, the qubit's capacitance, and the critical current, respectively.

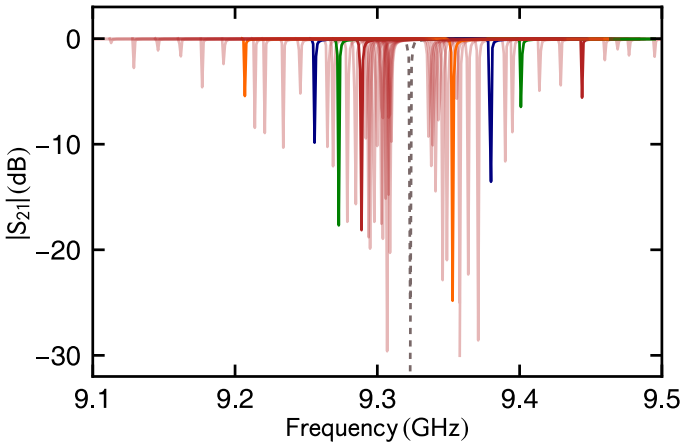

Figure 5.7: Simulated response $|S_{21}|$ of a single readout resonator coupled to the qubit capacitance. The different curves correspond to a parameter sweep of the ideal junction inductance L_{sim}, rendering the system harmonic. The bare resonator frequency is shown as gray dashed line. For clarity, only four exemplary curves have distinct colors, the extracted splitting is approximately 130 MHz. The quality factors and hence the depth of the curves is not simulated with high accuracy, and is subject to numerical variation. In this simulation, however only the resonances' frequencies are relevant.

between 8 GHz and 11 GHz. In this way, we could fit four qubits on one chip while still maintaining 0.5 mm of ground plane between resonator strips, to reduce crosstalk.

The design is composed of a feedline across the length of the chip, with two launcher pads on each end. The four readout resonators are capacitively coupled by their ends in close proximity to the feedline and the qubit, respectively. A picture of the complete chip is shown in Fig. 5.6. The coupling constant g is defined by the capacitance between the qubit conductor and the readout resonator, which can be defined by the gap between the structures ("a" in Fig. 5.6). To find the optimal geometry and distance, microwave simulations with the software package `Sonnet` [139] were performed.

By reproducing the layout of a single resonator coupled to feedline and qubit, the coupling can be realistically simulated, including an ideal inductance instead of the junction. If the value of this inductance L_{sim} is varied, an avoided crossing in the resonator response can be produced. The response curves for several values of inductance ranging from $L_{\mathrm{sim}} = 4.3\text{-}4.9\,\mathrm{nH}$ can be seen in Fig. 5.7. The smallest distance between the split response corresponds to twice the coupling rate. A distance of 15 µm corresponds to the intended coupling rate of $g = 65\,\mathrm{MHz}$.

To limit the Purcell effect but still ensure a strong dispersive shift, the coupling factor was designed to be $g = 65\,\mathrm{MHz}$. For a detuning of 1 GHz, and a strongly coupled resonator of

$Q_c \approx Q_L = 1000$, this results in a Purcell loss rate of $\Gamma_\kappa \approx (24\,\mu s)^{-1}$. For a slightly lower coupling rate ($Q_L = 5000$), the Purcell loss is $\Gamma_\kappa \approx (118\,\mu s)^{-1}$. The detuning is controlled via the gate voltage and can be used to vary the Purcell loss or the dispersive shift, if needed.

The coupling strength κ of the resonators to the feedline can be deduced directly from the width of the simulated resonance dips. Feedline and resonator are CPW structures, so their coupling is sensitive to the amount of ground plane in between. In addition, the coupling depends linearly on the length where the resonator is parallel to the feedline. Variation in both parameters was used to experimentally spread the coupling rate around $\kappa \approx 10 \cdot 10^3$. In our case, the robustness of the TiN layer during liftoff set a lower limit of approximately 2 µm for the thickness of the 500 µm long strips of ground plane separating resonator and feedline.

The CPW dimensions for the feedline ($w = 12\,\mu m$ and $s = 7\,\mu m$) were calculated as discussed in section 3.1.1. For the launchers, dimensions of $250 \times 250\,\mu m$ are sufficient for approximately three bond wire connections, as can be seen in Fig. B(appendix). Constant thickness of the substrate causes the ratio between gap and center conductor to vary with the size of the line. For the launchers the gap is $w = 190\,\mu m$. As a starting value, the length l_{res} of the readout resonators was calculated by

$$l_{res} = \frac{c}{\sqrt{\varepsilon_{eff}}} \frac{1}{2}, \tag{5.12}$$

with the effective dielectric constant $\varepsilon_{eff} = 6$. The kinetic inductance L_{kin} of the superconducting $\sim 90\,nm$ TiN film was evaluated after the first resonator measurements. To that end, we reproduce the measured frequencies in a Sonnet simulation, by varying L_{kin}. This resulted in a value of $L_{kin} \approx 1\,pH/\square$, which was used in all further simulations. The resonators were spaced roughly 400 MHz apart, corresponding to $\sim 200\,\mu m$ variation in length.

A common problem in CPW structures are so-called slotline modes, where the electrical potential on opposing parts of the ground plane are equal and opposite. In the presented design, these modes couple inductively to the central feedline and can have larger absolute amplitudes than the intended (quasi transverse electromagnetic) resonator modes. This can be suppressed by connecting the ground plane across the resonators or feedline by air bridges or bondwires. All samples have been equipped with bond wires distributed with the simulated density to suppress slotline modes. An exemplary picture can be found in the appendix (Fig. B).

The calculation of the shunt capacitance for the qubit was based on the estimated critical current range of the nanowire, and the limitation to stay in the transmon regime (see

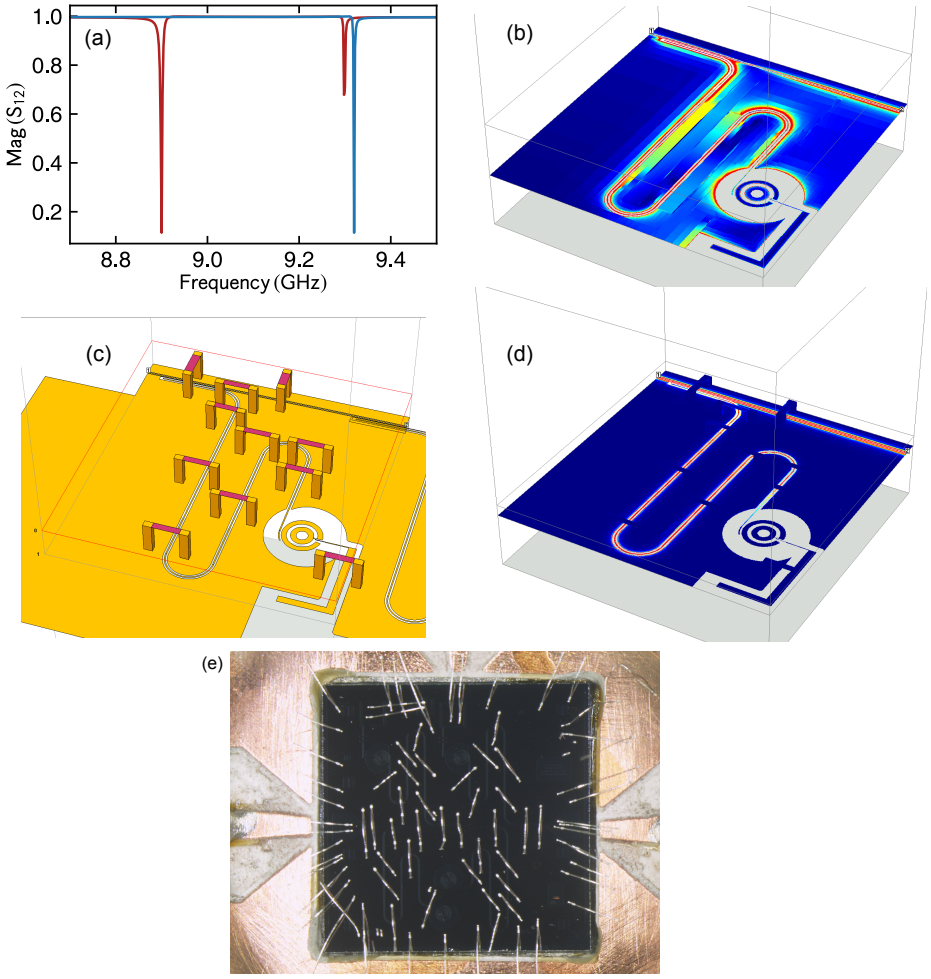

Figure 5.8: Simulated response $|S_{21}|$ of a single readout resonator coupled to the feedline. Without connections across the resonator, parasitic slotline modes appear. (a) shows the response with (blue) and without (red) connections across the resonator, respectively. The slotline mode at $\sim 8.9\,\mathrm{GHz}$ is more pronounced and causes a shift to the intended mode at $\sim 9.3\,\mathrm{GHz}$. The corresponding current distribution at $\sim 8.9\,\mathrm{GHz}$ is plotted in (b), large currents along the ground plane indicate a slotline mode. (d) shows the same simulation with added connections (vias) shown in (c) for clarity. The slotline mode is completely suppressed, which is confirmed by the corresponding frequency response (a) in blue. (e) Micrograph of a four-qubit chip, glued onto a copper-plated TMM10 sample-holder. The bond wires are used to contact the chip, and to prevent parasitic resonances by connecting the ground plane across resonators and feedline as shown in (c). The tapered connections on the chip-carrier are coplanar and matched to $50\,\Omega$. A zoomed out version of this image including the sample box can be found in appendix A.1.

Sec. 2.8.1). For a critical current tunable up to $I_c = 130\,\mathrm{nA}$, a capacitance of $C = 60\,\mathrm{fF}$ results in $\alpha \gtrsim 3\,\%$ anharmonicity and a qubit frequency tunable up to $\omega_q/2\pi = 12.6\,\mathrm{GHz}$. For the intended critical currents of approximately 80–100 nA, these parameters correspond to a ratio of $E_J/E_C = 120$–150, deep in the transmon regime.
The actual qubit frequency is still dependent on the gate voltage. The chosen capacitance enables dispersive readout and the possibility to tune the qubits in resonance with the resonators. Designing the capacitance to the intended value was achieved analogous to the simulation of the coupling g. Again the junction was replaced by an ideal inductor, the simulated resonance frequency is directly dependent on the capacitance. A parameter sweep of the distance between the inner and outer conductor of the qubit capacitance was used to determine the distance "b" in Fig. 5.6 corresponding to $C = 60\,\mathrm{fF}$ to be $42\,\mu\mathrm{m}$.

5.3.2 Sample Box Design

The purpose of the sample housing is to allow connections to the microwave and gate lines inside the cryostat, and to provide a clean microwave background without parasitic resonant modes in the relevant spectral range. Several multi-purpose box designs already existed prior to this work, but measurements and 3D simulations using the software `CST Studio` [140] showed resonant modes close to 11 GHz, close to the intended qubit transitions. These resonant box-modes had to be suppressed to prevent excessive Purcell loss. To this end, a new, smaller box was designed, see Fig. 5.9(b) for a rendering of the CAD design.

In the older version of the sample box, one objective was to minimize the internal volume, with the aim of increasing the frequency of the lowest supported mode. However, this approach requires the enclosed volume to be surrounded by a continuous conductor. In the older design, the square lid was flush with the top surface of the box and a cylinder slightly smaller than the round cutout in the box protruded inside to minimize the volume. This design has an undefined path for the current of the lowest (TM_{010}) mode, due to the stable oxide layer formed on an aluminum surface. In this case, the conductivity between box and lid is highly dependent on the cleanliness and flatness of the surfaces, and also on the pressure exerted by the screws, rendering the spectrum ill-defined. Contrary to its purpose, the structure can be described as a klystron cavity [141], where an increased capacitance between lid and box can significantly decrease the frequencies of the mode spectrum (compared to a simple cylindrical cavity).

To create a more reproducible and defined electromagnetic environment for the sample, a groove was added to the circular cutout, highlighted in white (arrow) in Fig. 5.9(b). The resulting cylindrical cutout below the groove is 0.45 mm smaller than the corresponding

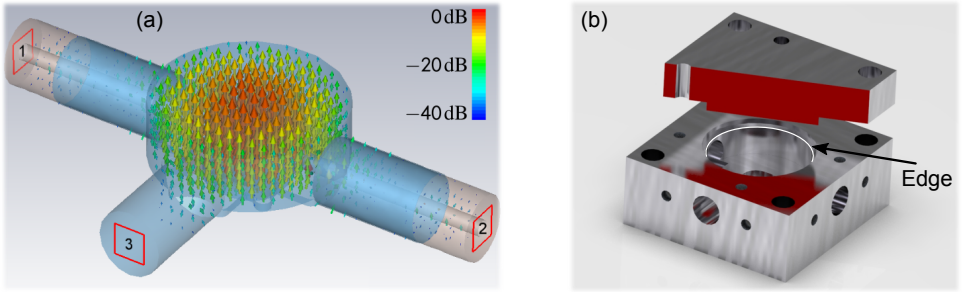

Figure 5.9: 3D models of the sample box. (a) Microwave simulation of the ground mode, including the silicon chip and SMA connectors on ports 1 and 2. The third connector is used for the gate and is therefore included in the simulation with a high port impedance. The arrows depict the electric field with the amplitude encoded in the color. The ground mode frequency is 18.5 GHz and well above the relevant frequency range of roughly 8 – 12 GHz. (b) Rendered CAD drawing of the same box, in the same orientation. A part of the lid has been cut away so the cylindrical protrusion contacting the groove on the box (white) can be seen. When closed, the two edges become slightly deformed and produce a galvanic contact, breaching the oxide layer formed on aluminum parts in the atmosphere.

cylindrical protrusion of the lid. This causes the touching surface of both parts to be deformed as the screws are tightened, breaching the surface oxide layer and producing a reproducible conducting geometry. A simulation of the mode spectrum for the new geometry shows the lowest mode at 18.5 GHz [see Fig. 5.9(a)], which was confirmed by spectroscopic measurements.

The second qualitative difference to the older sample boxes is a drilled hole of 1 mm diameter in the bottom of the box. It serves as a precise guide for the orientation while gluing the chip carrier. Later, it serves as a vent for the now otherwise almost vacuum-tight box, preventing slow leakage into the vacuum shield or condensation of air on the chip. Electromagnetic shielding is not affected, because the hole is much smaller than the wavelength in the relevant frequency range. The CAD model was designed using the software `Solid Edge` [142] and rendered by `Keyshot` [143]. All sample boxes were machined from 5754 aluminum alloy in the workshop of our institute.

6 Results

In this chapter the experimental results derived form long-term measurements of a transmon qubit and spectroscopic analysis of gatemon samples is presented. Further, measurements optimized for accuracy in the qubit transition frequency ω_q are used to extract the spectral density of observed frequency fluctuations. Implementing the interleaved pulse method discussed in section 5.2.3, simultaneous measurement of the qubit's relaxation and dephasing rate as well as its resonance frequency is possible. This enables us to analyze the correlations between these parameters on a time scale of the qubit's coherence time, and yields information about the microscopic origin of the intrinsic decoherence mechanisms in the sample. The results are consistent with a small number of microscopic two-level systems located at the edges of the superconducting film. Our data uniformly supports the interacting defect model [1, 40, 144, 145], as is discussed in the following.

6.1 Parameter fluctuations in qubits

The output of every projective qubit measurement is one of two values with added noise. To extract the probability distribution $P|n\rangle$ after a certain pulse sequence, the measurement has to be repeated and the output needs to be averaged. This necessary repetition for a theoretical perfect quantum system needs to be increased according to the SNR of a real experiment. For the presented measurements with a SNR of approximately 0.1, the minimum averaging for reliable fits was between 200 and 1000 per point. Under the assumption of stable qubit parameters, longer averaging leads to more accurate evaluation of its characteristic values.

However, during calibration measurements with a consecutive measurement technique, inconsistencies between subsequent measurements were observed. In this case, T_1 and T_2^R measurements had been alternated with several minutes of averaging for every single value. Some of the consecutive pairs violated the relaxation limitation for the dephasing time $T_2^* \leq 2T_1$, see Eq. (2.13).This observation supported the notion of fast fluctuation qubit parameters, and motivated the development of the interleaved measurement scheme, which was used in all following measurements.

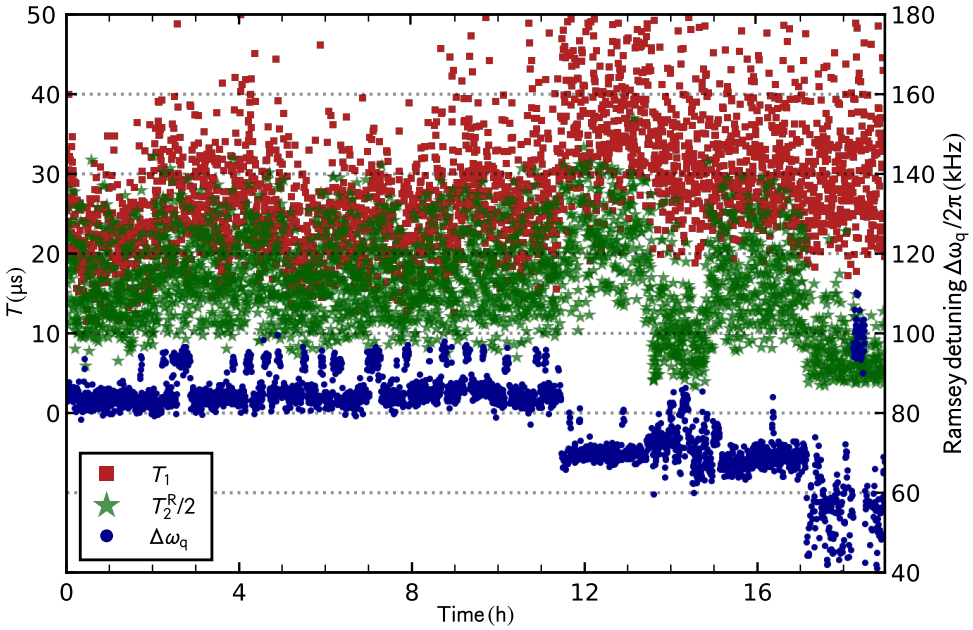

Figure 6.1: Exemplary long-term measurement, using the interleaved pulse method. The data taken over a course of 19 hours displays fluctuations in T_1 and T_2^R (red squares and green stars, left axis), and telegraph-like switching of the Ramsey detuning $\Delta\omega_q$ (blue dots, right axis), which is a direct measure for the shift in qubit frequency. The time resolution corresponds to 10 s of averaging using the interleaved pattern presented in section 5.2.3. For clarity, dephasing times are divided by two. Telegraphic switching in the qubit frequency as well as sudden variations in the fluctuation dynamics (e.g. at 11.5 h) can be seen. With this type of measurement and the subsequent correlation analysis, we reveal a connection between noise at mHz frequencies and qubit dephasing. This figure can also be found in the related publication [22].

Figure 6.1 shows the fit results of a typical long-term measurement. The Ramsey detuning $\Delta\omega_q$ depicted in blue dots is a direct measure for the shift in qubit frequency. The energy relaxation time T_1 is shown in red squares and the Ramsey dephasing time T_2^R in green stars. For clarity, dephasing times are divided by two. All values are extracted from least-squares fits to the respective functions, discussed in section 5.2.3. T_1 and T_2^R show fluctuations and a clear correlation with $\Delta\omega_q$, which we evaluate in the following. The qubit transition frequency displays telegraphic noise with multiple stationary points, which prompts our interpretation of the data in terms of an ensemble of environmental two-level systems (TLS) interacting with the qubit.

We interpret the presented data according to the interacting defect model, which is further motivated by recent experiments by Meißner *et al.* [146], where the thermal switching of individual TLS in AlO_x Josephson junctions was measured directly. Further, spectral diffusion of TLS was recently observed by monitoring the T_1 time of a tunable transmon

qubit by Klimov *et al.* [20]. Our results confirm the findings that single TLS strongly affect qubit coherence, independent of flux noise. In the interacting TLS model, defects may mutually interact electrically or via their response to mechanical strain [39, 40]. If the transition energy of a particular TLS is below or close to the thermal level $k_B T$, it undergoes random, thermally activated state-switching. We call these two-level fluctuators (TLF) to distinguish them from the more coherent TLS [1] with higher transition energies. Longitudinal coupling between TLS and TLF causes telegraphic fluctuation or spectral diffusion [147] of the TLS' resonance frequencies. This coupling can be mediated by mechanical strain, even for large detunings between TLS and TLF energy. The resulting time-dependent frequency fluctuation of near-resonant TLS give rise to phase noise of superconducting resonators [148] and may also cause the parameter fluctuations of qubits [145], investigated here. Figure 6.3(b) illustrates the physical picture.

First evidence that TLS are a dominating decoherence mechanism for superconducting qubits was reported by Martinis *et al*. [36], leading to improved qubit designs where the number of TLS in the oxide layer is reduced by smaller tunnel junctions [149]. Moreover, capacitive circuit components were optimized to reduce electric fields [150] and hence the coupling to TLS. We assume the standard dipole form of qubit-TLS coupling [38, 151]

$$H_{\mathrm{int},k} = \hbar g_k \sigma_z (a + a^\dagger), \tag{6.1}$$

with the the coupling strength g_k between qubit and TLS number k. To express the dynamics of the coupled system, we use the generic TLS Hamiltonian Eq. (2.16), and the approximated transmon Hamiltonian Eq. (2.74). Transformation into the dispersive frame yields

$$\begin{aligned} H_q + H_{\mathrm{TLS},k} + H_{\mathrm{int},k} \approx \hbar(\omega_q + \chi_k \sigma_z) a^\dagger a + \\ \frac{\hbar}{2}(\omega_{\mathrm{TLS},k} + \chi_k)\sigma_z - \hbar\alpha (a^\dagger)^2 (a)^2, \end{aligned} \tag{6.2}$$

where $\chi_k = g_k^2/\Delta$ is the dispersive shift and the detuning between TLS k and qubit is given by $\Delta = \omega_{\mathrm{TLS},k} - \omega_q$. The coupling strength g_k between qubit and TLS can be estimated from the observed fluctuation amplitude $\Delta\omega_q$, assuming resonant TLS with a typical dipole moment on the order of 1 eÅ [152–154]. The related analysis is presented in detail in section 6.1.1. In short, we find the frequency variation ranging from 5–140 kHz, which is inconsistent with the expected coupling strength of approximately 48 MHz for TLS inside the junction. By simulating the electric field distribution, we find the coupling strength to TLS at sites closer than 20 nm to capacitor edges is $g_k \gtrsim 100$ kHz. Which is in good agreement with our observations. Thus we conclude that the dominant TLS in our experiment reside close to film edges.

To fathom the microscopic origin of the fluctuations, we analyze correlations between all extracted parameters. The envelope of a Ramsey measurement consists of relaxation

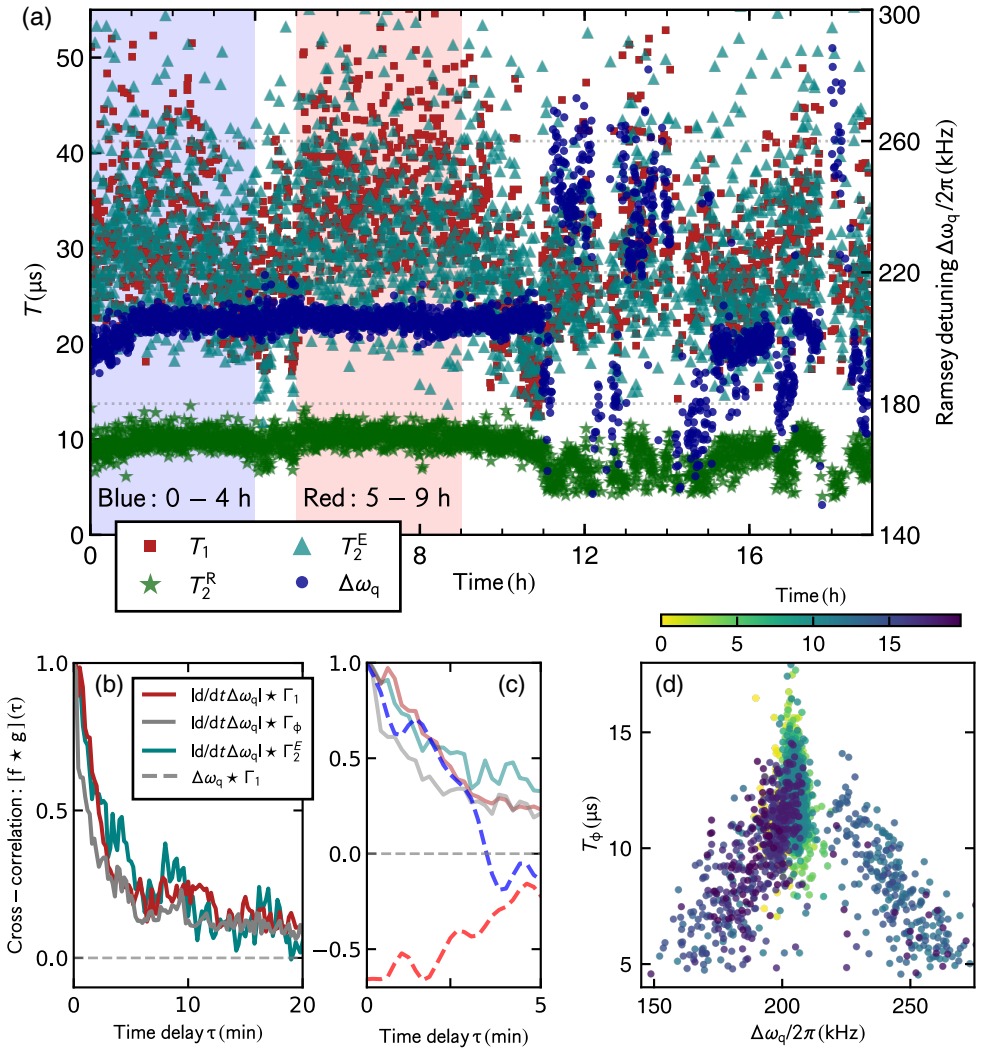

Figure 6.2: Data gathered during a successive cooldown (identical setup) with respect to Fig. 6.1. (a) Fit results of a long-term interleaved measurement with pronounced changes in qubit frequency of about 100 kHz (right axis) and Ramsey dephasing times consistently below 15 µs (green stars, left axis) even during times without relatively strong fluctuation (first 10 h). The blue and red shaded areas of four hours respectively, indicate timeframes with different signs for the cross-correlation between $\Delta\omega_q$ and Γ_1, plotted in (c). (b) shows cross-correlations of the absolute fluctuation strength $|d/dt\,\Delta\omega_q|$ and the relaxation or dephasing rates Γ_1, Γ_ϕ, and Γ_2^E of the dataset shown in (a). All curves show significant correlation at zero time delay τ, relating fluctuations in qubit frequency on the order of seconds to relaxation and dephasing down to the order of microseconds. A scatterplot of T_ϕ versus Ramsey detuning is shown in (d), the point color indicates the measurement time. Point clouds of different slopes can be seen, indicating positive, negative, and no correlation within the measurement period. Figures (c) and (d) can also be found in the related publication [22].

and pure dephasing T_ϕ, connected by Eq. (2.12). By measuring T_1 and T_2^{R}, we can extract the pure dephasing or the corresponding rate $\Gamma_\phi = 1/T_\phi$. The data shown in Fig. 6.2 was taken in a later cooldown compared to Fig. 6.1 and exhibited generally larger fluctuations and lower dephasing times without changes to the experimental setup. Scatterplots are an intuitive way to visualize correlation in data. In Fig. 6.2(d), the corresponding scatterplot to the raw data (a) relates the pure dephasing T_ϕ and the change in qubit frequency $\Delta\omega_{\mathrm{q}}$. Interestingly, different types of correlation could be observed in the course of a single measurement of 19 hours. A time interval of about 10 h without obvious correlation between T_ϕ and $\Delta\omega_{\mathrm{q}}$ is followed by alternating positive and negative correlation during times of strong frequency fluctuation[1]. We interpret these observations as coupling to a single spectrally diffusing TLS, crossing the qubit frequency several times. To our knowledge, no other interpretation is in agreement with our observations, as is discussed in section 6.1.3. The polarity and strength of the correlations depend on the sign of the detuning between TLS and qubit and their mutual coupling strength.

In the interpretation of the presented data, the relevant noise spectra have to be taken into account. For Ramsey measurements, variations down to the total averaging time contribute to the extracted dephasing. A slow drift in frequency for example, causes several sine functions of different frequency to produce a reduced envelope when averaged. Only the relaxation rate Γ_1 and the spin-echo dephasing rate Γ_2^{E} have a low-frequency cutoff. Relaxation processes become irrelevant if the rate is significantly slower than the repetition rate or the inverse qubit relaxation time. Spin-echo is specifically designed to counteract low frequency noise (see Sec. 2.6), the cutoff is 25 kHz in our case. Consequently, correlations of Γ_1 and Γ_2^{E} with the fluctuation strength measured at a rate on the order of $(10\,\mathrm{s})^{-1}$ allow the conclusion of fluctuations on the order of microseconds to be correlated to slow variations in qubit frequency.

The second mathematical tool used to analyze the connection between the observed parameters is the cross-correlation. For two signals $f(t)$ and $g(t)$ it is defined as

$$(f \star g)(\tau) = \int_{-\infty}^{\infty} f^*(t) g(t+\tau) \mathrm{d}t, \tag{6.3}$$

where $f^*(t)$ denotes the complex conjugate of $f(t)$. The cross-correlation can be understood as a measure of the similarity between the two signals f and g, dependent on their respective temporal offset τ. The cross-correlation of two identical signals is maximal if they completely overlap and the time-delay τ is zero. The normalized cross-correlation between different parameters of the data shown in Fig. 6.2(a) is plotted below in (b). The

[1] Please note, that the positive and negative correlated branch in Fig. 6.2(d) contain points of the respective opposite color. The hopping between these can also be seen in the last third of the raw data.

highest value for all of the shown pairs is at zero delay. This proofs similar behavior with respect to the mean value, which suggests the same source of fluctuation. In this case, it relates the absolute fluctuation strength $|\mathrm{d}/\mathrm{d}t\,\Delta\omega_\mathrm{q}|$ to higher dephasing and relaxation rates, linking slow fluctuations on the order of seconds, namely the measurement repetition rate, to dephasing or relaxation up to the order of microseconds. The absolute fluctuation strength $|\mathrm{d}/\mathrm{d}t\,\Delta\omega_\mathrm{q}|$ is calculated as the absolute value of the frequency difference of every data point to the previous.

The coherence time of individual high frequency TLS in AlO_x was found to range from nanoseconds to microseconds [154, 155]. Thus, for qubits with several microsecond relaxation times like our sample, these TLS represent a relevant photon loss channel if coupled to the qubit and close to resonance. Assuming that a single dominant TLS is responsible for dephasing and photon loss implies that the cross-correlations $\Delta\omega_\mathrm{q} \star \Gamma_\phi$ and $\Delta\omega_\mathrm{q} \star \Gamma_1$ have the largest value and the same sign at zero delay. While this was our typical observation, also opposing signs were encountered. To probe for possible temporary variations in the cross-correlations, smaller windows instead of the whole data set have been examined. Figure 6.2(c) shows the cross-correlation between qubit frequency and relaxation rate in dashed lines corresponding to the shaded areas of the same color in (a). The change in sign at zero delay between two timeframes of 4 h points towards different sources for dephasing and relaxation in this case. The observation can be explained by the presence of a stable TLS 'A' close to resonance with the qubit, increasing its relaxation, and a second more weakly coupled TLS 'B' which fluctuates and is mainly responsible for dephasing. Correlations of opposite sign emerge if both TLS are above or below the qubit frequency. In that case, diffusion of B towards the qubit frequency results in level repulsion, detuning the qubit further from A, resulting in increased dephasing, but reduced energy relaxation. In Fig. 6.3(b), TLS 'A' would be located between the dark red TLS and the blue qubit resonance.

During periods of high coherence, we observe no cross-correlation between Γ_1 and $|\frac{\mathrm{d}}{\mathrm{d}t}\Delta\omega_\mathrm{q}|$ (see appendix Fig. A.5). We interpret this, as due to a bath of weakly coupled TLS limiting Γ_1, rather than a single strongly coupled TLS [156–158]. In the same measurement we still observed some correlation of the absolute fluctuation strength with Γ_ϕ. Our explanation is the different scaling of relaxation $\Gamma_1 \propto g^2/\Delta^2$ and dispersive shift $\chi_k \propto g^2/\Delta$ regarding the detuning. Thus, a TLS can be detuned far enough to still cause dephasing, but not dominate the relaxation. This also explains the stronger fluctuations in Γ_ϕ compared to Γ_1, observed throughout our measurements.

To perform a quantitative analysis of the connection between the fluctuations in qubit frequency and the pure dephasing time, we examine the variance in qubit frequency associated with multiple ranges of dephasing times while the qubit frequency is relatively

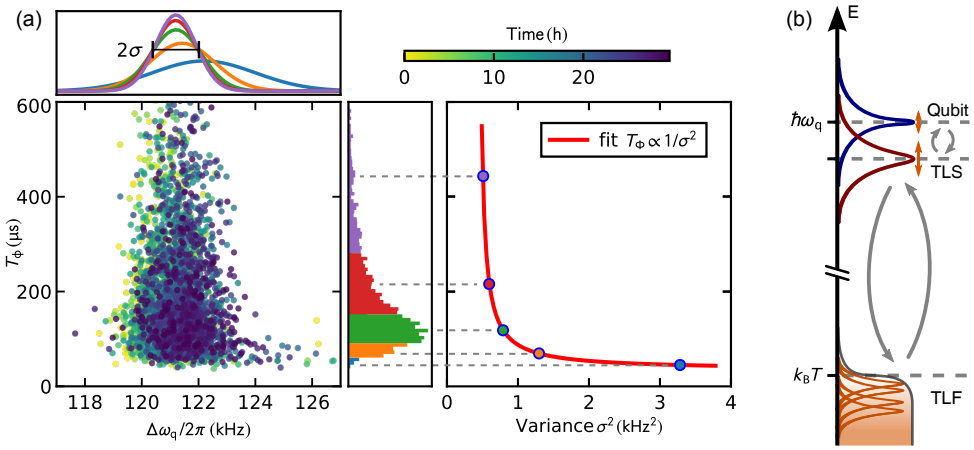

Figure 6.3: (a) Quantitative relation between slow fluctuation in qubit frequency and pure dephasing. The scatterplot was taken while the qubit frequency was relatively stable. Under this condition the standard deviation of the qubit frequency $\sigma(\Delta\omega_q)$ can be extracted. Bins of pure dephasing times are colored in the vertical histogram, corresponding fits to normal distributions (top panel) are colored accordingly. Lower dephasing times correspond to larger variances in qubit frequency. The standard deviation of the violet curve is indicated exemplarily. On the right, the extracted variances σ^2 are plotted against the corresponding mean values of pure dephasing. A fit to the expected function $T_\phi \propto 1/\sigma^2$ is in agreement with the data. (b) Illustration how the frequency of a single TLS near resonance with the qubit fluctuates due to its longitudinal coupling to thermally activated TLS (so-called TLF) at energies at or below $k_B T$ (orange shaded area). Depending on the detuning between qubit and TLS, this can cause positive or negative correlations between qubit coherence times and its resonance frequency. This figure can also be found in the related publication [22].

stable, see Fig. 6.3(a)[2]. We bin the frequency shift data according to their associated pure dephasing times, and fit the data in each bin to a Gaussian distribution. Assuming the qubit frequency shifts to be due to random sampling of a linear function (as is the case for small frequency shifts of a dispersively coupled TLS), the standard deviation σ of the distributions will be proportional to the slope of this linear function. Conversely, the pure dephasing rate Γ_ϕ in such a situation is proportional to the square of the slope of the frequency change with the random parameter [159]. If the origin of the measured large frequency fluctuations is the same as the one for the pure dephasing, we expect the two slopes to be the same. In this case, for each bin in pure dephasing time we have $\Gamma_\phi \propto \sigma^2$, which is in good agreement with our data. Relating to our physical picture (Fig. 6.3), the same noise channel for high and low frequency noise corresponds to the effect of one dominant TLS, coupled to a bath of TLF.

[2] The absence of large jumps in frequency is necessary in order to define the variance of the distribution as a small perturbation. The related dataset is shown in appendix Fig. A.5.

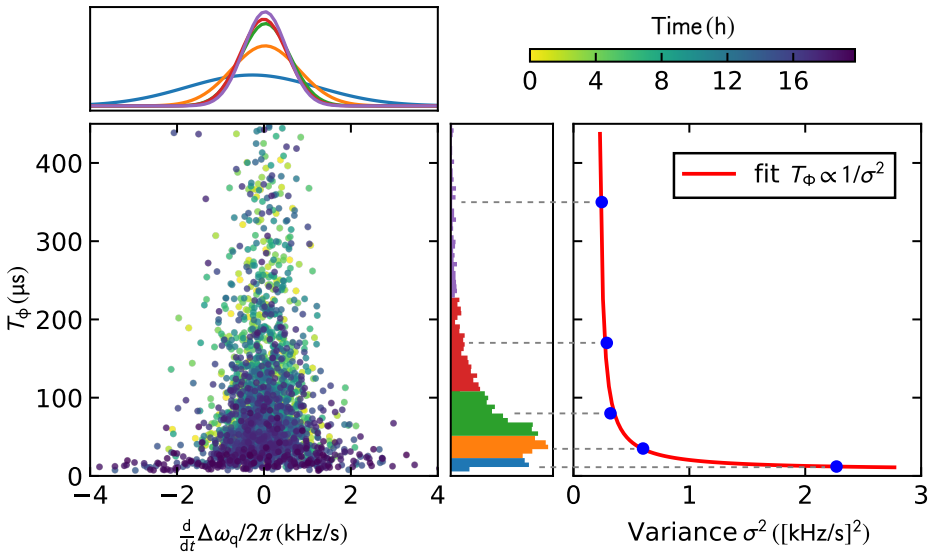

Figure 6.4: Scatterplot of the pure dephasing time T_Φ versus fluctuation strength of the data shown in Fig. 6.1. The point color indicates the measurement time. The triangular shape in the scatterplot indicates that stronger fluctuations in $\Delta\omega_q$ on the order of seconds are related to lower pure dephasing times, and was consistently measured in all cooldowns, regardless of fluctuation strength or coherence. Fits to normal distributions for different ranges of pure dephasing in the top panel show the increased variance in fluctuation strength at lower pure dephasing times. The functional dependence is roughly $T_\Phi \propto 1/\sigma^2$. For visibility, the outliers due to switching which are symmetrically distributed around zero on the x-axis near $\pm 20\,\mathrm{kHz/s}$ are not shown.

Figure 6.4 shows the results of the same analysis for the fluctuation strength $|\frac{d}{dt}\Delta\omega_q|$, and data with larger fluctuations (the raw data is shown in Fig. 6.1). In order to compare different data sets and varying frequency stability, we focus on the contribution of small fluctuations. This is equivalent to discarding the larger jumps between metastable states, see appendix Fig. A.5(b) for the corresponding scatterplot of qubit frequencies. In the scatterplot of Fig. 6.4, larger jumps produce small point clouds at $\pm 20\,\mathrm{kHz/s}$. By focusing on small fluctuations, we can interpret the variation in ω_q as dispersive shift. The resulting distribution follows approximately $T_\Phi \propto 1/\sigma^2$. The fit error is too large, to rule out a different exponent. The trend towards low pure dephasing times for large variance in the fluctuation strength however, is clearly evident.

In repeated measurements and different cooldowns, we find the qubit coherence times to be anti-correlated with the maximum amplitude of frequency fluctuations. In our model, this corresponds to different dispersive shifts χ_k due to the respective dominant TLS. During cooldowns with persistently long relaxation and dephasing times (see e.g./appendix Fig. A.5), this shift is low and qubit frequency fluctuations are small. If increased interaction with a TLS leads to shorter relaxation and dephasing times, even for

intermediate times without resolvable frequency fluctuations of the qubit, dephasing tends to stay low. This is expected because of the higher frequency noise we can not resolve by our sub-Hz repetition rate. Possible explanations for abrupt changes in decoherence dynamics are slow thermalization processes in the amorphous parts, logarithmically slow TLS relaxation [160], or background radiation.

Throughout our measurements, reduced coherence manifests itself most strongly in the dephasing times T_ϕ and T_2^{R} rather than in T_1 and spin echo T_2^{E}. The observed effective reduction of dephasing by spin echo pulses suggests most of the relevant noise spectrum to lie below the spin-echo cutoff frequency of 25 kHz, in our case. This observation is in agreement with the typical maximum fluctuation rate of thermal TLS due to phonons of $\gamma_1^{\max}(T = 20\,\mathrm{mK}) \approx 1.9\,\mathrm{kHz}$ [154] in our case. Further cross-correlation analysis confirms the relationship between the observed frequency fluctuations and dephasing in all datasets. We conclude that the same mechanism is responsible for the qubits dephasing and slow fluctuations of its parameters.

6.1.1 Coupling Strength and Density Estimation

Inside the qubit's Josephson junction, the coupling rate due to interaction of the TLS' dipole moment to the root mean square electric field of the qubits vacuum fluctuation follows from [36]

$$h \cdot g_{\max} = |\vec{E}||\vec{d}| = \frac{\bar{U}}{a}|\vec{d}|, \tag{6.4}$$

with the TLS' dipole moment $|\vec{d}|$ on the order of 1 eÅ [152–154], and the RMS voltage between the qubit electrodes $\bar{U}$, which is given by

$$\bar{U} = \sqrt{\frac{\hbar\omega_{\mathrm{q}}}{2C_{\mathrm{q}}}} \approx 3.7\,\mu\mathrm{V}. \tag{6.5}$$

The coupling strength is given by

$$g_{\max} = \frac{|\vec{d}|}{a}\sqrt{\frac{\hbar\omega_{\mathrm{q}}}{2C_{\mathrm{q}}}} \approx 50\,\mathrm{MHz}, \tag{6.6}$$

with the total qubit capacitance of $C_{\mathrm{q}} = 120\,\mathrm{fF}$, $\omega_{\mathrm{q}}/2\pi = 4.75\,\mathrm{GHz}$ and the width of the tunnel barrier thickness of the JJ a, corresponding to an estimated height of the oxide barrier of 1.8 nm [161]. In our experiment, the largest observed frequency fluctuations are 140 kHz. As the dispersive shift scales as $\chi = g^2/\Delta$, this implies a detuning between qubit and possible junction-TLS of the order of many GHz. Alternating positive and negative correlations in Fig. 6.2(d) imply frequency diffusion across the qubit frequency, see also

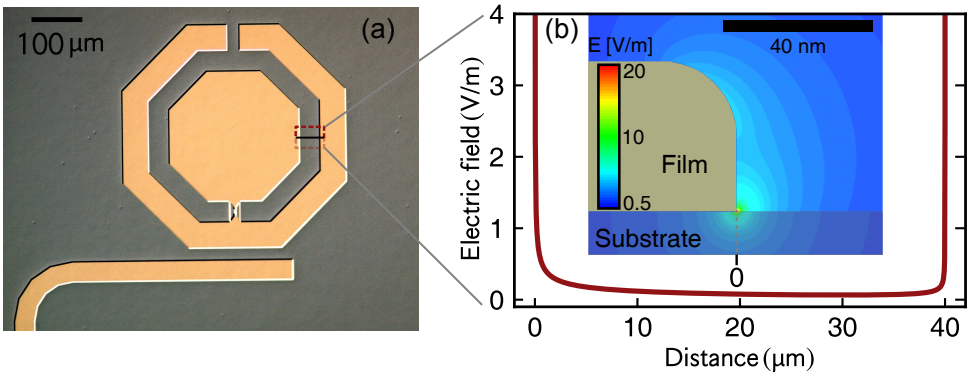

Figure 6.5: Micrograph of the used qubit (a) and simulation of the electric field distribution between the concentric parts of the qubit capacitance, created by the vacuum state (b). In the microscopic image, the qubit capacitance, and a small part of the readout resonator can be seen. A Josephson junction connects the outer and inner part of the octagon-shaped capacitance. The simulated field distribution along the black line between the conducting films is shown on the right (b). The inset shows a contour plot of the field distribution in close proximity of the superconducting film edge, the simulation model was developed by A. Bilmes [162]. The field distribution is slightly asymmetric between the two parts of the capacitance, because of their different size. The minimum of the electric field is 55 mV/m and very close to the film, it increases drastically. The Substrate here is intrinsic silicon, the films are treated as perfect conductors.

the raw data in Fig. 6.2(a). Thermal switching of several GHz detuned TLS between below and above the qubit is suppressed by the Boltzmann factor $\exp\left(-\hbar\omega_\mathrm{q}/k_\mathrm{B}T\right) \approx 10^{-7}$ and thus extremely unlikely. Therefore we assume the detuning between qubit and the most relevant (we call dominant) TLS to be close to zero for times of relatively large frequency shifts. If we assume the TLS to reside in the junction, the observed coupling implies their dipole moments to deviate less than 0.1° from perpendicular to the qubits electric field, which is unlikely for several observed TLS. We reason it unlikely that the observed frequency shifts are due to TLS which are located in the qubit's Josephson junction.

Significant changes in quality factors of superconducting resonators due to surface treatment observed e.g. in Ref [158] imply considerable coupling to surface TLS. The electric field at edges of metal films scales approximately as $1/\sqrt{x}$ [163]. In our case, the resulting field strengths are larger than 4 V/m at any position closer than 20 nm to the superconducting film edges, see Fig. 6.5. For the typical TLS dipole moments of $d \approx 1\,\mathrm{e\AA}$, this corresponds to a coupling rate to the qubit of $g \gtrsim 100\,\mathrm{kHz}$ in agreement with our observed qubit frequency shifts. The TLS mostly responsible for decoherence and frequency shifts are therefore presumably at the surface, near edges which create field enhancement. From simulations of the field distribution of our circuit, we know that the field drops to about 55 mV/m in the middle between the conductors, resulting in a maximum coupling rate of about $g = 1.3\,\mathrm{kHz}$ there. This result matches well with the

smallest observed fluctuations of about 1 kHz. We conclude that while our experiment is most sensitive to TLS residing on surfaces of the shunt capacitor, we can also measure the effect of other TLS positioned anywhere in the shunt capacitance. Figure 6.5(b) illustrates the electric field created by the qubits vacuum state. The field simulations have been calculated using the finite element software . The field simulations have been performed with `ANSYS Maxwell` [164], using the simulation model elaborated in the PhD work of A. Bilmes [162]. There, it has been experimentally shown that resonantly detectable TLS reside within 100nm from the metal-substrate-vacuum edge. These findings support our notion that the here-observed fluctuations are dominated by surface-TLS.

A recent preprint of Lisenfeld *et al.* [165] uses electrical field spectroscopy to distinguish between defects in Josephson junctions and at circuit interfaces. Their results suggest approximately 60 % of the observed TLS to reside at circuit interfaces. In addition, they place about 40 % in the large-area parasitic Josephson junctions that are produced as a byproduct during shadow evaporation. Considering these results, it is possible that parts of the observed fluctuations in our sample also originate in TLS inside the parasitic junction.

Although our fixed frequency qubit limits the accessible information on TLS density, we can deduce a rough estimate for the surface density of the dominant TLS based on the statistics of several measurements. We observed TLS with coupling rates on the order of $g_{\mathrm{max}} \approx 100\,\mathrm{kHz}$, and the observed frequency fluctuations for times of relatively high coherence and frequency stability are on the order of $\Delta\omega_{\mathrm{q,min}}/2\pi \approx 1\,\mathrm{kHz}$. Thus, assuming TLS of the coupling strength g_{max} are also present in times of high coherence, the detuning to such a TLS is approximately $2\pi g_{\mathrm{max}}^2/\Delta\omega_{\mathrm{q,min}} = 10\,\mathrm{MHz}$. At this frequency spacing of 20 MHz, the frequency density of dominant TLS is $50/\mathrm{GHz}$. The area of the qubit surface which is exposed to qubit fields stronger than $4\,\mathrm{V/m}$ is about $164\,\mu\mathrm{m}^2$. This results in an estimated dominant-TLS surface density of $0.3/\mathrm{GHz}\,\mu\mathrm{m}^2$.
For comparison, the TLS densities reported by other groups are e.g. $0.5/\mathrm{GHz}\,\mu\mathrm{m}^2$ for large ($\approx 1\,\mu\mathrm{m}^2$) $\mathrm{Al/AlO_x}$ junctions [36] or $2.4/\mathrm{GHz}\,\mu\mathrm{m}^2$ for significantly less coherent qubits [166]. The low loss material $\mathrm{Si_3N_4}$ showed only $0.03/\mathrm{GHz}\,\mu\mathrm{m}^2$ in measurements on lumped-element resonators [167]. Compared to these values, our estimated TLS density is plausible and as expected smaller than for larger $\mathrm{Al/AlO_x}$ junction qubits.

6.1.2 Spectral Noise Analysis

To further elucidate the origin of the observed qubit frequency fluctuations, we performed a long term measurement in which we optimized the measurement pulse sequence to gain maximum frequency resolution. This was done by only using Ramsey pulses with a relatively large number of 80 points, leading to a precise sine-fit for frequency extraction.

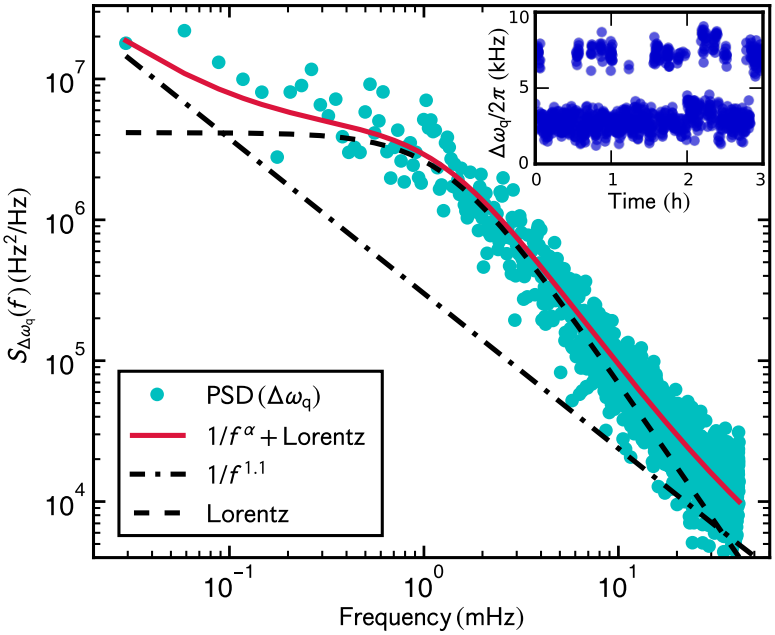

Figure 6.6: Power spectral density of frequency fluctuations $\Delta\omega_q$ (cyan dots) in a long-term measurement of 47 h, revealing significant deviation from $1/f^\alpha$ noise (dash-dotted line). A fit (red solid line) is in agreement with the effect of a single thermal TLF (black dashed line) plus $1/f^\alpha$. The inset shows a short section of raw data, showing telegraphic noise that is presumably due to frequency switching of a near-resonant TLS coupled to a single thermal fluctuator. The frequency uncertainty is approximately the size of the dots. This figure can also be found in the related publication [22].

The mean frequency error in the related fits is 0.7 kHz. If the observed fluctuations are due to individual TLS, we expect the power spectral density to follow the functional form given by the longitudinal part of Eq. (2.28)

$$S(\omega) \propto (1 - \langle\sigma_z\rangle^2) \frac{2\gamma_{1,k}}{\gamma_{1,k}^2 + \omega^2}, \tag{6.7}$$

a Lorentz distribution centered at zero frequency [38]. Here, $\gamma_{1,k}$ is the TLS relaxation rate, $\langle\sigma_z\rangle = \tanh(E_k/2k_BT)$ is the thermal equilibrium population of TLS 'k' and $E_k = \sqrt{\varepsilon_k^2 + \Delta_k^2}$ is its transition energy as presented in Sec. 2.4. Under the assumption of a uniform distribution of TLS barrier heights, the superposition of many such Lorentzian spectra are responsible for the typically observed low-frequency noise of the form $\sim 1/f^\alpha$, which is usually observed in all solid-state qubits [168]. This kind of noise is also called "pink", if the exponent α is close to 1.

The PSD of our measurements, shown in Fig. 6.6, deviates strongly from the ensemble $1/f^{\alpha}$ noise limit, but is fit well by a single Lorentzian added to a $1/f^{\alpha}$-type background. From these measurements, we extract a background parameter of $\alpha \approx 1.1$ and the switching rate of the individual TLS of $\gamma_1 \approx 1\,\mathrm{mHz}$. For the distribution of switching rates, we estimate a TLF energy of $E_k/k_\mathrm{B}T = \ln\left(\Gamma_\downarrow/\Gamma_\uparrow\right) = 1.1$ in good agreement with the assumption that the switching TLF are located spectrally close to the experimental temperature. The presented fits are performed using the python library SciPy. Orthogonal distance regression (scipy.odr) proved to be robust and reliable. Handling errors in x and y is beneficial, considering the the large range of the noise spectrum $S(\Delta\omega_\mathrm{q})$ and possible errors introduced by the masking procedure.

For the PSD analysis we use Welch's method [169]. It achieves a reduction of noise by segmenting the data into smaller sets and sampling these with an overlapping window function in the time domain. The average squared magnitude of the discrete Fourier transforms of these samples, gives the power spectrum. This method reduces the frequency resolution but enhances the SNR of noise power measurements. Some details of the extracted PSD will, however depend on the window function and its size. In Fig. 6.6 a 'Kaiser' ($\alpha = 4$) window [170], with a segment size of 2844 points, corresponding to dividing the data into 10 samples, with 50 % overlap was used. Overall this set of data contained 14222 Ramsey measurements. All data processing has also been verified with random data, to exclude analysis artifacts from being identified as signal. The effective frequency limit and SNR of this measurement could be improved significantly, using a quantum-limited amplifier.

6.1.3 Other Decoherence Mechanisms

Our interpretation in terms of the interacting defect model attributes the observed parameter fluctuations to TLS. This is possible, because our sample is insensitive to other possible sources for discrete fluctuations. Those are: non-equilibrium quasiparticles (qp), the movement of Abriskosov vortices and temperature fluctuations. As shown in section 2.8.1, the transmon qubit's transition energy is exponentially insensitive to charge fluctuations with respect to $\sqrt{E_J/E_C}$ [23]. In our sample, the change in qubit frequency due to a single qp, switching the charge parity of the capacitance [171, 172], is about 2 Hz and thus not observable. This can be calculated, using Eq. (2.68) with different values for the offset charge.

A large number of non-equilibrium qp may contribute to relaxation [173] but can not account for discrete fluctuations in ω_q or abrupt changes in dynamics. A small amount of trapped qp, could explain discrete jumps in coherence related to the number of qp. In

this scenario however, relaxation and dephasing rates would be recurrent, which is not observed. Variations in qubit frequency remain unexplained by quasiparticles, for our $\sqrt{E_J/E_C}$ ratio.

High magnetic fields may induce field dependent loss in a single junction qubit, as shown by Schneider *et al.* [174]. To verify the intrinsic insensitivity of this experiment to flux noise, we measured the sample with roughly in-plane magnetic fields up to $\pm 1\,\mathrm{mT}$, and observed no changes in either coherence or frequency stability. Possible residual fields e.g. due to adsorbates [175] are many orders of magnitude smaller and can be excluded.

Significant correlation of the absolute fluctuation strength and the relaxation rate [Fig. 6.2(b)]

$$[|\frac{\mathrm{d}}{\mathrm{d}t}\Delta\omega_\mathrm{q}| \star \Gamma_1](\tau = 0) \approx 1, \tag{6.8}$$

during periods of low dephasing times require transversal coupling. This renders direct influence of far detuned (thermal) TLF and critical current fluctuations unlikely. For high detuning, the matrix element for energy exchange is negligible. Critical current fluctuations only affect the qubit frequency and can not account for correlation of Γ_1 with the fluctuation strength.

Temperature fluctuations are known to induce low-frequency critical current noise [176]. This effect is exponentially temperature dependent and found to be relevant at $T \gtrsim T_\mathrm{c}/3$ in Al-AlO_x-Al junctions. At our experimental temperature of $T = 20\,\mathrm{mK}$ its effect is several orders of magnitude below the observed noise level and can be excluded. A summary of the results presented in this chapter can also be found in our related publication [22].

6.2 Voltage Tuning of Nanowire Junctions

The design and fabrication of gatemon circuits in CPW geometry has been discussed in sections 5.3 and 4.2. After the last metallization step, the samples are packaged in the specifically built combination of sample box and PCB (see Sec 5.3.2). Wire bonding is used to connect the feedline and gate contacts on the chip, and to suppress slotline modes.

To evaluate the samples, the resonance frequencies of the four resonators are determined by a spectroscopic measurement. At this point, the dependence of the critical current on the gate voltage $I_c(V_g)$ is not yet known. Thus in a first test, the gate voltage V_g is varied while the resonance frequency of the resonators is monitored. For this spectroscopic measurement, the microwave drive power needs to be close to the single photon limit. The drive power is estimated using the known attenuation (see section 5.2.2). The gate current was monitored and limited to 1 µA, to prevent changing V_g due to parasitic resistance. For high gate voltages, avalanche breakdown of the silicon substrate is possible. The critical voltage was highly dependent on the sample. We observed drastically increased current for voltages above $\sim$ 3–8 V for bottom gate samples. Thus, limiting the current is crucial to avoid excessive heating and damaging the sample or the measurement electronics. For side gate samples, increased current was observed above $\approx$ 30 V.

The result of two typical spectroscopic measurements, monitoring the transmission close to the center frequency of a single resonator during voltage sweeps, are shown in Fig. 6.7. The upper color-plot (a) shows the sweep from low to high gate voltage, and the lower one (b) vice versa. In (a), a distinct shift in resonator frequency occurs between approximately 2.5 V and 4 V. For higher voltages the resonance frequency stays constant and lowered about 2 MHz compared to the value at $V_g = 0$ V. Subsequent lowering of the gate voltage, depicted in Fig. 6.7(b), also shows a shift of $\sim$ 5 MHz at $V_g = 4$ V. The initial resonance frequency is slowly recovered towards a voltage of $V_g = -8$ V. This hysteretic behavior is reproducible and indicates charging effects that bias the nanowire analogous to a floating gate. A possible microscopic explanation is the charging of surface states, as discussed in chapter 4. The data shown in Fig. 6.7 corresponds to a sample with bottom gates, side gate samples also showed similar hysteretic behavior at consistently higher voltages, see appendix Fig. A.3.

For bottom gates, the distance between gate electrode and nanowire is defined by the dielectric buffer layer, of 15 nm HfO_2 in this case. For side gates, the corresponding distance depends on the exact positioning of the nanowire, as shown in Ch. 4. Here the distance is approximately 500 nm. As expected, qualitatively similar behavior corresponds to lower voltages for bottom gates.

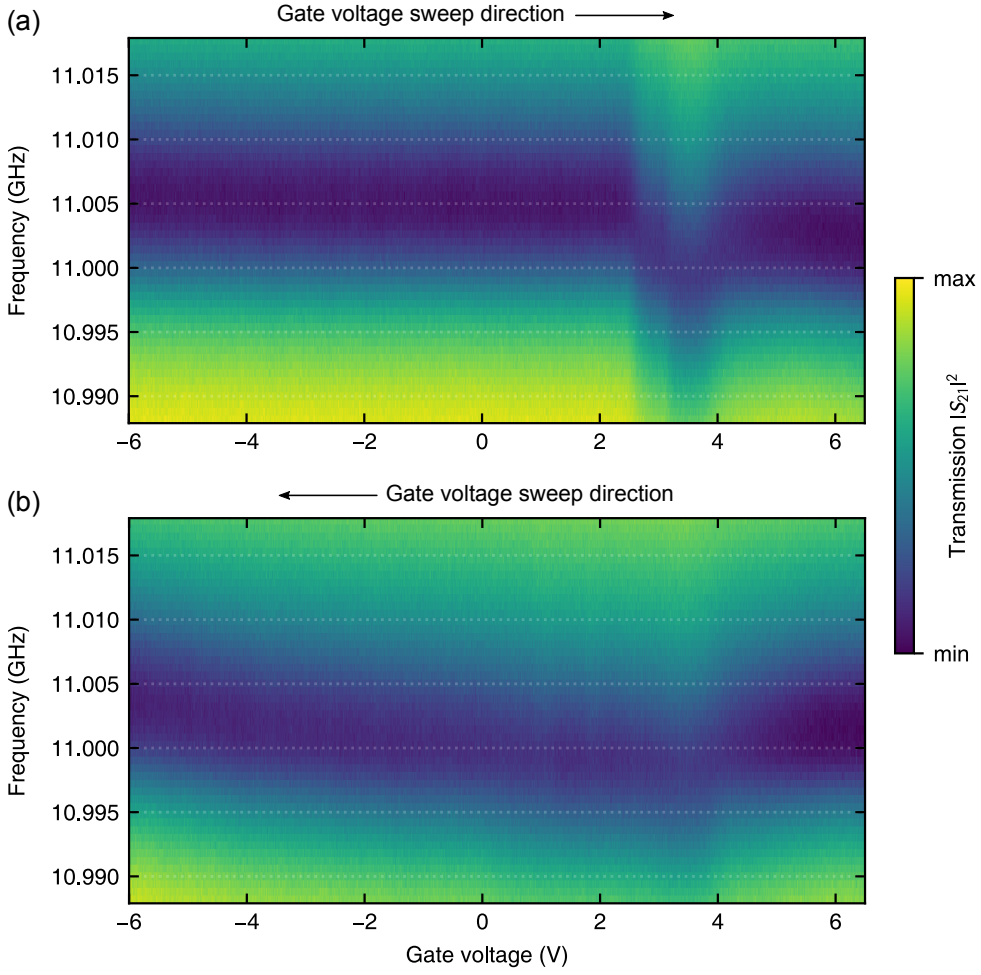

Figure 6.7: Color plots of the transmitted signal $|S_{21}|^2$ in the vicinity of a single resonator, coupled to a gatemon qubit. The amplitude is color coded and plotted depending on the frequency (y-axis) and gate voltage (x-axis). For the sweep in the positive voltage direction (a), a clear variation in resonance frequency between approximately 2.5 V and 4 V can be seen. For the subsequent downward sweep (b), the shift around 4 V is also present, however the initial resonance minimum of approximately 11.005 GHz is reached at −8 V. This hysteretic behavior can be explained by charging effects in close vicinity to the nanowire. Similar results with slightly different voltages were obtained for all of the working nanowire junctions and their respective resonators.

Interleaved time domain measurements were hindered by the comparatively high losses of the gatemon samples. The time-resolved results of driving the gatemon samples at high power, can be found in appendix A.4. Short Rabi-like oscillations at a frequency of 35 MHz and a decay time of approximately 60 ns can be seen. However, attempts to reduce the drive power to a level where the frequency broadening allows distinct qubit transitions to be addressed, resulted in unusable, noisy signals. In spectroscopy, no avoided crossing with the resonator could be observed in the accessible voltage range. Therefore, a clear extrapolation of the critical current was not possible. For the bottom gate samples, the qubit capacitance is approximately 60 fF, which results in an estimated qubit transition frequency of 11 GHz for a critical current of 100 nA. Continuous current measurements by Patrick Zellekens at Jülich Research Centre showed critical currents of approximately 130 nA at a gate voltage of 7 V. So the critical current range is expected to be large enough to cause an avoided crossing in the range of applied gate voltages.

7 Conclusion and Outlook

In order to investigate decoherence in transmon qubits, we developed a time-multiplexed measurement protocol. This enabled us to extract temporally correlated relaxation and dephasing rates, as well as the related qubit frequencies. We applied this technique in long-term measurements of a highly coherent non-tunable transmon qubit based on an Al/AlOx/Al junction, and exposed telegraphic noise in the qubits transition frequency correlated with strong variations in its dephasing and relaxation rates. Telegraphic noise with multiple stationary points prompts our interpretation of the data in terms of an ensemble of two-level systems (TLS) interacting with the qubit. Noise originating in defects is highly dependent on the used materials, their interfaces and the used fabrication techniques. Therefore we investigated a second type of transmon qubit, based in a semiconducting weak link. This so called gatemon is described by the same fundamental Hamiltonian, but represents a different material system.

We designed and fabricated gatemon structures, based on semiconducting InAs nanowire junctions. We observed gate dependent shifts in the coupled readout resonators and increased the gate effect by using bottom gates. The pronounced hysteresis in gate voltage observed in gatemon samples indicates significant charging effects. In the presented experiments, these are a interfering with gate control. However, this effect also shows the possibility to locally maintain the gate potential by trapped charge. Different kinds of Josephson field-effect transistors (JoFETs) have already been demonstrated [177, 178]. A similar device, including a floating gate, might be utilized to build a floating gate tunable qubit or a latching type of JoFET switch.

Despite careful design and fabrication, we did not observe a clear qubit signature in the gatemon samples. We attribute this to strong dielectric losses, which are presumably caused by the dielectric layer separating gate and nanowire. A design that is independent of a dielectric buffer layer could solve this problem. In this regard, side gate structures are inherently superior, but require a relatively large distance between electrodes to be effective.

The analysis of correlated long-term measurements of our conventional transmon qubit, showed positive and negative correlation between dephasing and fluctuations in qubit

frequency on the timescale of seconds to days. We attribute these to the influence of individual dominant TLS, which may couple to the qubit by their electric dipole moments. Longitudinal coupling between TLS and thermal fluctuators causes telegraphic fluctuation or spectral diffusion of the TLS' resonance frequencies. We infer that the observed parameter fluctuations of superconducting qubits is caused by the time-dependent frequency fluctuation of near-resonant TLS. Cross-correlation and PSD analysis confirm this interpretation and ascribe the source of fluctuation to interactions between thermal fluctuators and TLS near resonance with the qubit.

By comparing the fluctuation amplitude with electric field simulations, we locate the dominant defects close to conductor edges. We hope that our findings motivate the search of structures or fabrication techniques overcoming the limitations caused by TLS. For this process, our estimation of their location on film edges provides an important first step.

Our data evidences a small number of TLS, which dominate dephasing if near-resonant. The $1/f$ noise background we observed, may emerge from a bath of more weakly coupled TLS. We attribute switching of a single TLS to the strong changes in dephasing and relaxation times in our data. We conclude that even single TLS on the edges of the superconducting films can dominate decoherence and cause random parameter fluctuations in superconducting qubits. We find that other sources of fluctuation, like temperature variations, critical current fluctuations, quasiparticle tunneling, or flux vortices play secondary roles in the presented experiment.

Finding specific materials or fabrication steps that result in a reduction or even avoidance of TLS in the relevant spectral range is challenging. We propose to use the presented analysis as a tool, to find variations due to fabrication or materials in larger batches of qubits. Because the interaction is assumed to be local, samples with frequency multiplexed qubits may be used, where possible, to reduce fabrication costs and time. In addition, the premise of local noise can be tested with the developed methods, by correlating simultaneously acquired parameters of several qubits from a multi-qubit chip.

Finally, we conclude that the influence of surface TLS constitutes an up to now unavoidable source of random fluctuation for any microscopic device operating in the low-power microwave regime. Critical reduction of relaxation and dephasing times by single material defects constitutes a major challenge for future quantum computers, especially for scaled-up devices, as the probability for parameter fluctuations in a given time scales exponentially with the number of qubits. Our findings underline the necessity of continuous re-calibration in today's solid-state qubits. Implementing new materials or fabrication methods may mitigate this problem. However, the random nature of TLS fluctuations imply that fundamental improvements to qubit parameter stability are necessary in order to realize useful many-qubit systems.

A potential solution could lie in continuous monitoring of qubit parameters and conditional reconfiguration of qubit couplings. Analogous techniques are already used in solid-state flash memory (bad block management). The counterpart in a quantum processor could rely on sorting out qubits with temporary low coherence. A type of qubit devoid of defects would of course be preferable. I am convinced, that quantum computing will become a useful tool in the future. Possibly not in the way we expect today. I hope that this work constitutes a small step in that direction.

Appendix

A Quality Factor Calculation

The squared amplitude of the resonators complex S-matrix element has a Lorentzian line shape in the frequency domain. This is a direct result of the exponential decay of energy in a dissipative harmonic oscillator, as the Fourier transform of an exponential is Lorentzian. The line shape also known as Cauchy distribution is defined as

$$L(\omega;\omega_0,\Gamma) = \frac{1}{\pi\Gamma}\left(\frac{\Gamma^2}{(\omega-\omega_0)^2+\Gamma^2}\right), \tag{A.1}$$

the resonance frequency ω_0 and the half-width at half-maximum (HWHM) Γ. We can define the loaded quality factor Q_L of a resonator coupled to a transmission line, by the characteristic decay time of its resonance. The corresponding characteristic function or Fourier transform of Eq. A.1 is

$$\mathscr{F}[L(\omega;\omega_0,\Gamma)] = \int_{-\infty}^{\infty} L(\omega;\omega_0,\Gamma)e^{-i\omega t}d\omega = e^{i\omega_0 t}\cdot e^{-\Gamma t} \tag{A.2}$$

decaying with the rate Γ. If we consider the full-width at half-maximum, as usually measured in spectroscopy experiments, we have to include a factor of $1/2$, such that $\Gamma \to \Gamma/2$. The squared amplitude of the S-parameter of a resonator also resembles a Lorentzian

$$|S_{21}|^2 = \frac{\left(\frac{1}{1+\kappa}\right)^2}{1+4Q_L^2\left(\frac{\omega-\omega_0}{\omega_0}\right)^2}. \tag{A.3}$$

If we compare the terms in Eq. A.3 to Eq. A.1, we can extract

$$\Gamma = \frac{\omega_0}{2Q_L}. \tag{A.4}$$

The decay time τ is defined by the time it takes the energy of the damped oscillation to drop to $1/e$ of the initial value, thus, the decay time is

$$e^{-}1 = e^{-\Gamma\tau} \qquad \to \qquad \tau = \frac{1}{\Gamma}. \tag{A.5}$$

Together with Eq. A.4 we can express the decay time by the quality factor

$$\tau = \frac{2Q_L}{\omega_0} = \frac{1}{\alpha}, \tag{A.6}$$

associating the quality factor to the damped oscillation of a resonator. Sometimes, the attenuation rate α or the damping ratio $\zeta = \alpha/\omega_0$ are used to define the damping of a resonator.

B Details on Chip Mounting

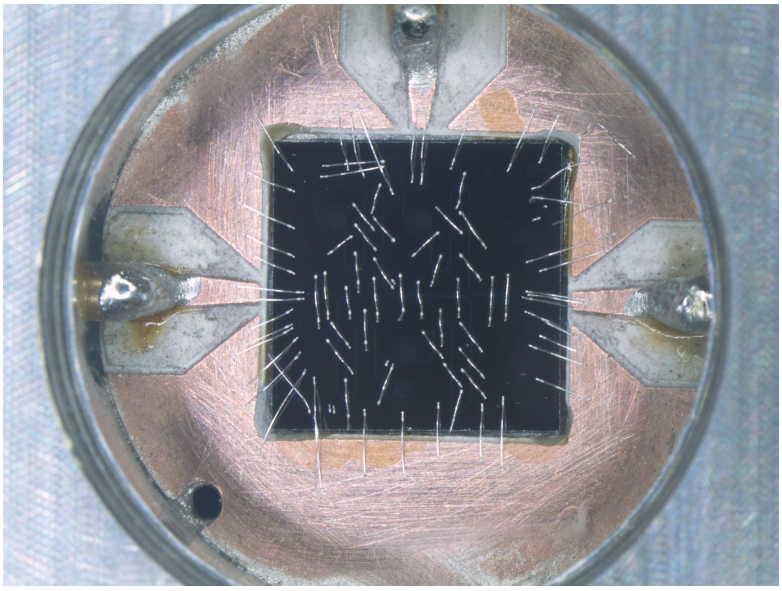

Figure A.1: Micrograph of a four-qubit chip, glued onto a copper-plated TMM10 sample-holder inside an aluminum sample box. Conductive silver varnish is used to ensure electrical contact between the box and the copper sample holder. The soldered connections contact the inner conductors of the SMA plugs. The feedline is contacted on the left and right, the gate on top. The bond wires on the chip are used to prevent parasitic resonances by connecting the ground plane across resonators and feedline (explained in detail in Sec. 5.3.1). The tapered connections on the chip-carrier are coplanar and matched to 50 Ω, with an outer diameter matching the cutout in the box. The hole in the lower left is used to define the orientation of the chip carrier and to vent the enclosed space inside the sample box, rendering it suitable for high vacuum.

C Fabrication Details

Fabrication parameters for gatemon samples, prior to nanowire positioning. Substrate: intrinsic silicon(100) with a bulk resistivity of $\rho > 80\,\mathrm{k}\Omega\,\mathrm{cm}$

1. Clean

   Dip in acetone (ACE) (5 min) and isopropanol (IPA) (5 min) at RT

   Dry with nitrogen gas (N_2)

   Heat to 100 °C for H_2O evaporation

   Dip in hexamethyldisilazane (HMDS) at 130 °C
2. Spin coat with UV6.06 950K at 4000 rpm for 60 s
3. Bake for 30/60/30 seconds at 80/130/80°C
4. Ebeam lithography of etch markers
   beam current 0.5 nA, dose 28 $\mu C/cm^2$, step size 5 nm
5. RIE etching flow rates 55/5 s cm^3 of CHF_3/O_2
   RF power 25 W, ICP power 100 W, for 13 min
6. Resist solving in ACE 16 h, dip in ACE (5 min), IPA (5 min), N_2 dry
7. Spin coat with PMMA 950K at 4000 rpm for 60 s
8. Bake for 60/600 seconds at 80/180°C
9. Ebeam lithography of bottom gates, gate lines
   beam current 1 nA, dose 2350 $\mu C/cm^2$, step size 2.5 nm
10. Development with IPA for 2 min, bake for 5 min at 100 °C
11. Deposition of 10/10nm of Ti/Pt
12. Lift-off, ACE 16 h, dip in ACE (5 min), IPA (5 min), N_2 dry
13. Spin coat with UV 6.06:AR-P 600-09, 2:1 at 4000 rpm for 60 s
14. Bake for 30/60/30 seconds at 80/130/80°C
15. Ebeam lithography of bond pads, NW positioning markers, large markers
    fine – beam current 1 nA, dose 28 $\mu C/cm^2$, step size 2.5 nm
    coarse – beam current 150 nA, dose 28 $\mu C/cm^2$, step size 25 nm

16. Post bake for 5 min at 140 °C, dip in DI water for 10 min
17. Pre-metalization treatment, O_2 plasma 200 s cm^3, 100 W, 20 s
18. Deposition of 30/130nm of Ti/Pt
19. Lift-off in dimethyl sulfoxide (DSMO) for 16 h, dip in ACE (5 min), IPA (5 min), N_2 dry
20. Dielectric deposition (Nanocluster ALD) 3 nm Al_2O_3, 15 nm HfO_2
21. Spin coat with UV 6.06:AR-P 600-09, 2:1 at 4000 rpm for 60 s
22. Bake for 30/60/30 seconds at 80/130/80°C
23. Ebeam lithography of feedline, resonators, ground plane
    fine – beam current 1 nA, dose 28 μC/cm^2, step size 2.5 nm
    coarse – beam current 150 nA, dose 28 μC/cm^2, step size 25 nm
24. Post bake for 5 min at 140 °C, dip in DI water for 10 min
25. Pre-metalization treatment, O_2 plasma 200 s cm^3, 100 W, 20 s
26. Deposition of 90 nm of TiN
27. Lift-off in DSMO for 16 h, dip in ACE (5 min), IPA (5 min), N_2 dry

D Voltage Tuning of Nanowire Junctions

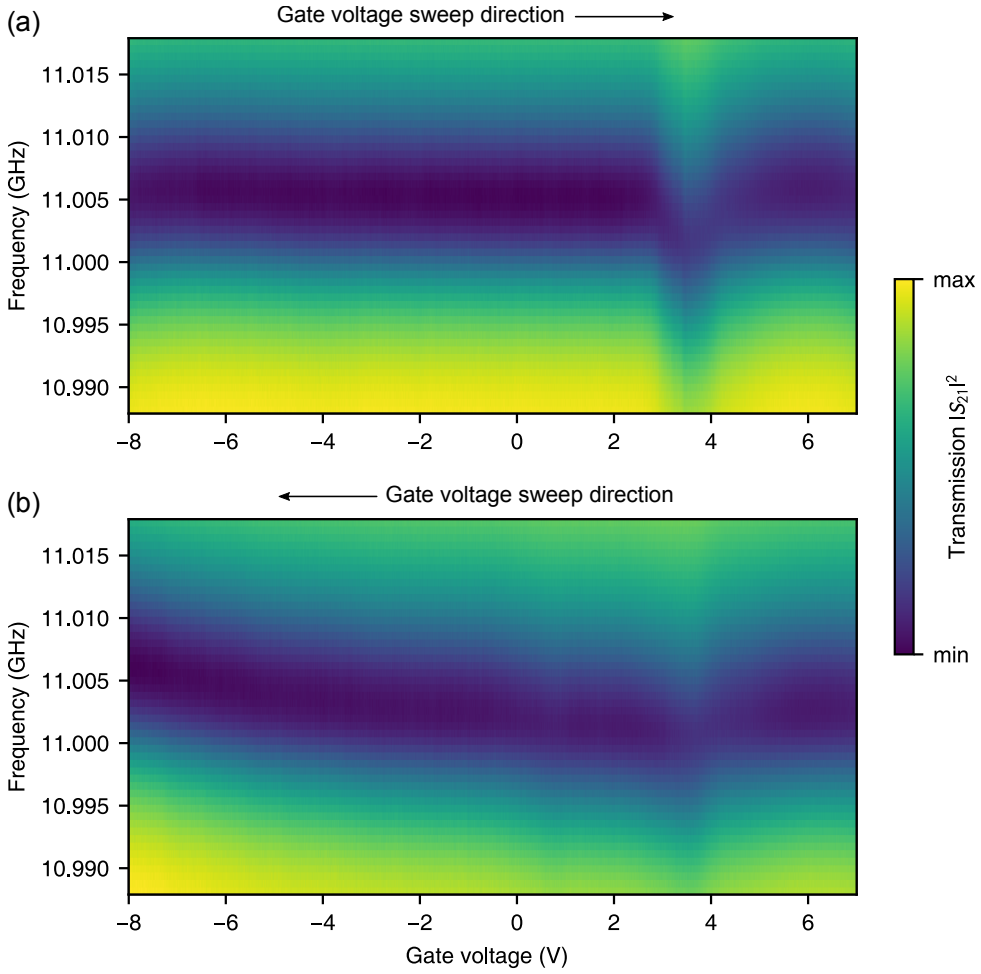

Figure A.2: Color plots of the transmitted signal $|S_{21}|^2$ in the vicinity of a single resonator, coupled to a gatemon qubit. This measurement was performed analogous to Fig. 6.7, but at 25 dB higher input signal power. The amplitude is color coded and plotted depending on the frequency (y-axis) and gate voltage (x-axis). The same voltage dependence and hysteretic behavior as for the low-power measurement can be seen, ruling out the dispersive shift due to a single excitation in the qubit.

Additional spectroscopic measurements with higher readout power are depicted in Fig. A.2. A typical measurement of a gatemon sample with side gate can be seen in Fig. A.3. Hysteretic shift in resonator frequency for approximately $\pm 20\,\mathrm{V}$ can be seen.

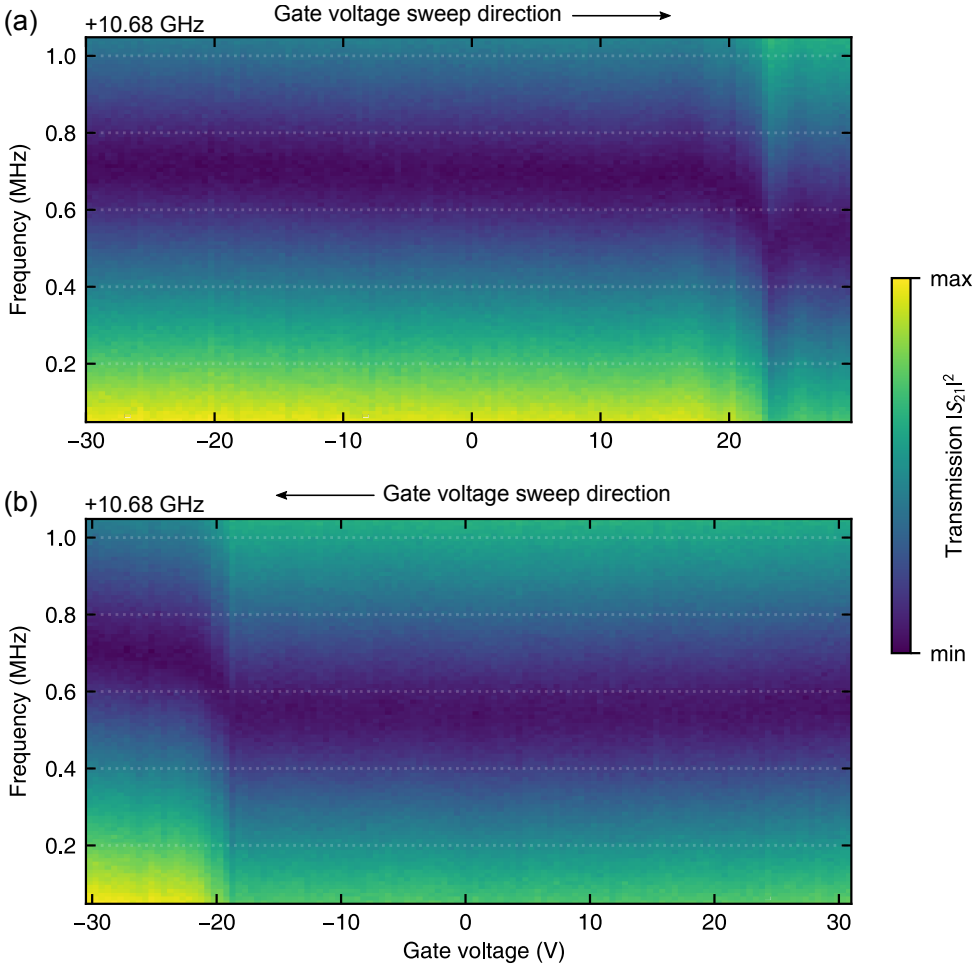

Figure A.3: Spectroscopic gate-sweep measurement analogous to Figs. 6.7 and A.2, but instead of a bottom gate, this sample uses a side gate with larger spacing between the gate electrode and the nanowire junction. The response to variation in the gate voltage is qualitatively similar to the samples with bottom-gate, but at approximately 10 times larger voltages and 10 times smaller frequency variations.

E Additional Data and Analysis

To minimize the effect of fit inaccuracy on our statistical analysis, e.g. due to fluctuations occurring during data acquisition for a single trace, or strong noise, unreliable fits with uncertainties larger than ten times the average are masked in the data sets. In the presented measurements, between 2 and 10% of the single slices had inaccurate fitting and are not shown, the presented results are insensitive to the masking. We have verified that the detuning of pulses due to the measured shifts in qubit frequency does not lead to a systematic bias in the extracted parameters. For the observed fluctuation strength in frequency, the maximum change in signal amplitude of the decay curves is 0.8 %. The extraction of pure dephasing time T_Φ associated with the rate Γ_Φ implies a simple exponential decay in Ramsey measurements. While this is not necessarily the case [179], the corresponding deviation compared to e.g. Gaussian decay is smaller than the fitting error.

The maximum data acquisition rate is limited by the smallest number of points which still yield confident fits. The number of points required to characterize Ramsey oscillations depends on their frequency and decay time. A higher Ramsey frequency leads to improved SNR for the frequency shift but requires a higher sampling rate. For a given number of points this implies a shorter interval of free evolution times, reducing the SNR of T_2^{R}, leading to a tradeoff between good fits to the frequency shift and Ramsey decay time for a given number of measurements. A high SNR is crucial for a conclusive PSD analysis, as statistical noise due to fit uncertainty raises the noise floor. We balance the distribution and number of points to achieve a tradeoff for the signal in different parameters. For example, the measurement depicted in Fig. 6.6 was optimized for accurate frequency fitting and achieves a mean error of 0.7 kHz, but the mean dephasing-time error is $\pm 10\,\mu$s. For comparison, the mean errors in Fig. 6.1 are $\pm 2.7\,\mu\mathrm{s}\,(T_1), \pm 5.4\,\mu\mathrm{s}\,(T_2^{\mathrm{R}})$, and $\pm 0.9\,\mathrm{kHz}\,(\Delta\omega_{\mathrm{q}})$.
Potential fluctuations of the readout resonator frequency f_r only affect the SNR of our measurements but have no influence on the extracted parameters.

For comparatively strong microwave drive power far above the single photon regime, Rabi-like oscillations could be observed in a gatemon sample. It was however not possible to observe Rabi oscillations for lower powers, necessary to address a single qubit transition. We ascribe this observation to a very high decay rate Γ_1. Further, no avoided crossing with the resonator could be achieved by gate-tuning, and the qubit frequency could not clearly be identified. Therefore we can not deduce the critical current of the Nanowire. Abrupt changes in contrast may result from variable surface charge on the NW.

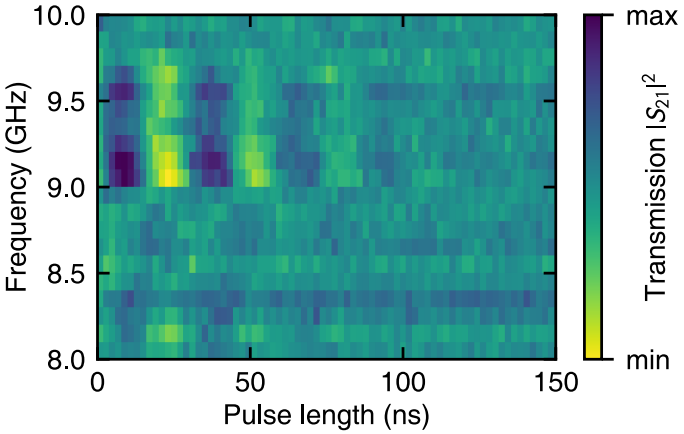

Figure A.4: For a high power drive, fast decaying Rabi-like oscillations could be observed in a gatemon sample at a gate voltage of 30 V. The expected chevron pattern is too broad in frequency, to be caused by a single qubit transition. Broadening and strong overlap of higher qubit transitions is expected for strong drive power [180]. The decay time is approximately 60 ns, and the oscillation frequency is 35 MHz.

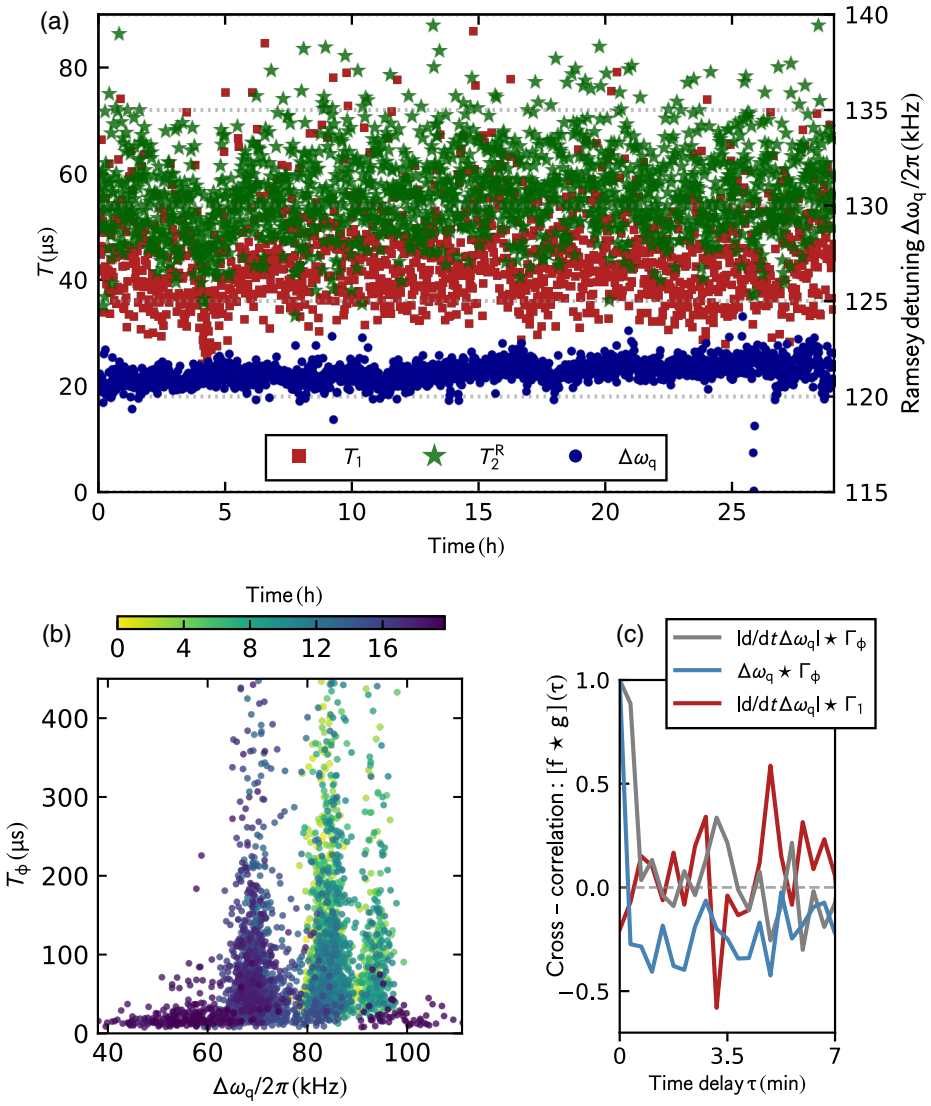

Figure A.5: (a) Subsequent cooldown with respect to Fig. 6.2 (no changes to the setup). The qubit frequency is relatively stable (mean frequency noise of 2kHz) and shows consistently high relaxation and dephasing times. A slow drift in frequency can be seen. (b) shows a scatterplot of the pure dephasing against the shift in qubit frequency of the data shown in fig. 6.1. Several metastable points in frequency and larger variation towards lower pure dephasing times can be seen. (c) At zero time delay τ, only Γ_Φ shows a small correlation (compared to the noise-level) with the absolute fluctuation strength (gray) and the qubit frequency (light blue). No correlation with the relaxation rate was observed.

Bibliography

[1] Clemens Müller and Jared H.Cole and Jurgen Lisenfeld: *Towards understanding two-level-systems in amorphous solids - insights from quantum circuits*, Reports on Progress in Physics, (2019), DOI: 10.1088/1361-6633/ab3a7e (cit. on pp. i, 10, 11, 29, 75, 77).

[2] A. M. Turing: *On Computable Numbers, with an Application to the Entscheidungsproblem*, Proceedings of the London Mathematical Society **s2-42**, 230–265 (1937), DOI: 10.1112/plms/s2-42.1.230 (cit. on p. 1).

[3] B. Lojek, *History of Semiconductor Engineering*. Springer-Verlag GmbH, 2007, [Online]. Available: https://www.ebook.de/de/product/8900126/bo_lojek_history_of_semiconductor_engineering.html (cit. on p. 1).

[4] K.Y.Sanbonmatsu and C-S.Tung: *Large-scale simulations of the ribosome: a new landmark in computational biology*, Journal of Physics: Conference Series **46**, 334–342 (2006), DOI: 10.1088/1742-6596/46/1/047 (cit. on p. 1).

[5] S. d'Ascoli, S. C. Noble, D. B. Bowen, M. Campanelli, J. H. Krolik, and V. Mewes: *Electromagnetic Emission from Supermassive Binary Black Holes Approaching Merger*, The Astrophysical Journal **865**, 140 (2018), DOI: 10.3847/1538-4357/aad8b4 (cit. on p. 1).

[6] B. P. Lanyon, J. D. Whitfield, G. G. Gillett, M. E. Goggin, M. P. Almeida, I. Kassal, J. D. Biamonte, M. Mohseni, B. J. Powell, M. Barbieri, A. Aspuru-Guzik, and A. G. White: *Towards quantum chemistry on a quantum computer*, Nature Chemistry **2**, 106–111 (2010), DOI: 10.1038/nchem.483 (cit. on p. 1).

[7] R. P. Feynman: *Simulating physics with computers*, International Journal of Theoretical Physics **21**, 467–488 (1982), DOI: 10.1007/bf02650179 (cit. on p. 1).

[8] D. Deutsch: *Quantum Theory, the Church-Turing Principle and the Universal Quantum Computer*, Proceedings of the Royal Society A: Mathematical, Physical and Engineering Sciences **400**, 97–117 (1985), DOI: 10.1098/rspa.1985.0070 (cit. on p. 1).

[9] Jonathan Romero and Ryan Babbush and Jarrod R McClean and Cornelius Hempel and Peter J Love and Alán Aspuru-Guzik: *Strategies for quantum computing molecular energies using the unitary coupled cluster ansatz*, Quantum Science and Technology **4**, 014008 (2018), DOI: 10.1088/2058-9565/aad3e4 (cit. on pp. 1, 6).

[10] P.W.Shor, *Algorithms for quantum computation: discrete logarithms and factoring*, *Proceedings 35th Annual Symposium on Foundations of Computer Science*, IEEE Comput. Soc. Press, DOI: 10.1109/sfcs.1994.365700 (cit. on p. 1).

[11] L. K. Grover: *A fast quantum mechanical algorithm for database search*, arXiv, (1996) (cit. on p. 1).

[12] A. G. Fowler, M. Mariantoni, J. M. Martinis, and A. N. Cleland: *Surface codes: Towards practical large-scale quantum computation*, Physical Review A **86**, (2012), DOI: 10.1103/physreva.86.032324 (cit. on p. 2).

[13] R. Barends, J. Kelly, A. Megrant, A. Veitia, D. Sank, E. Jeffrey, T. C. White, J. Mutus, A. G. Fowler, B. Campbell, Y. Chen, Z. Chen, B. Chiaro, A. Dunsworth, C. Neill, P. O'Malley, P. Roushan, A. Vainsencher, J. Wenner, A. N. Korotkov, A. N. Cleland, and J. M. Martinis: *Superconducting quantum circuits at the surface code threshold for fault tolerance*, Nature **508**, 500–503 (2014), DOI: 10.1038/nature13171 (cit. on pp. 2, 15).

[14] K. Wright and K. M. Beck and S. Debnath and J. M. Amini and Y. Nam and N. Grzesiak and J. -S. Chen and N. C. Pisenti and M. Chmielewski and C. Collins and K. M. Hudek and J. Mizrahi and J. D. Wong-Campos and S. Allen and J. Apisdorf and P. Solomon and M. Williams and A. M. Ducore and A. Blinov and S. M. Kreikemeier and V. Chaplin and M. Keesan and C. Monroe and J. Kim: *Benchmarking an 11-qubit quantum computer*, arXiv, (2019), [Online]. Available: https://ionq.com/ (cit. on p. 2).

[15] Y. Wu, Y. Wang, X. Qin, X. Rong, and J. Du: *A programmable two-qubit solid-state quantum processor under ambient conditions*, npj Quantum Information **5**, (2019), DOI: 10.1038/s41534-019-0129-z (cit. on p. 2).

[16] P. Krantz, M. Kjaergaard, F. Yan, T. P. Orlando, S. Gustavsson, and W. D. Oliver: *A quantum engineer's guide to superconducting qubits*, Applied Physics Reviews **6**, 021318 (2019), DOI: 10.1063/1.5089550 (cit. on p. 2).

[17] J. Preskill: *Quantum Computing in the NISQ era and beyond*, Quantum **2**, 79 (2018), DOI: 10.22331/q-2018-08-06-79 (cit. on p. 2).

[18] K.Kakuyanagi, T.Baba, Y.Matsuzaki, H.Nakano, S.Saito, and K.Semba: *Observation of quantum Zeno effect in a superconducting flux qubit*, New Journal of Physics **17**, 063035 (2015), DOI: 10.1088/1367-2630/17/6/063035 (cit. on pp. 2, 44).

[19] F. Arute, K. Arya, *et al.*: *Quantum supremacy using a programmable superconducting processor*, Nature **574**, 505–510 (2019), DOI: 10.1038/s41586-019-1666-5 (cit. on pp. 2, 26).

[20] P. Klimov, J. Kelly, *et al.*: *Fluctuations of Energy-Relaxation Times in Superconducting Qubits*, Physical Review Letters **121**, (2018), DOI: 10.1103/physrevlett.121.090502 (cit. on pp. 2, 77).

[21] J. J. Burnett, A. Bengtsson, M. Scigliuzzo, D. Niepce, M. Kudra, P. Delsing, and J. Bylander: *Decoherence benchmarking of superconducting qubits*, npj Quantum Information **5**, (2019), DOI: 10.1038/s41534-019-0168-5 (cit. on pp. 2, 67).

[22] S. Schlör, J. Lisenfeld, C. Müller, A. Bilmes, A. Schneider, D. P. Pappas, A. V. Ustinov, and M. Weides: *Correlating Decoherence in Transmon Qubits: Low Frequency Noise by Single Fluctuators*, Physical Review Letters **123**, (2019), DOI: 10.1103/physrevlett.123.190502 (cit. on pp. 2, 76, 78, 81, 86, 88).

[23] J. Koch, T. M. Yu, J. Gambetta, A. A. Houck, D. I. Schuster, J. Majer, A. Blais, M. H. Devoret, S. M. Girvin, and R. J. Schoelkopf: *Charge-insensitive qubit design derived from the Cooper pair box*, Physical Review A **76**, (2007), DOI: 10.1103/physreva.76.042319 (cit. on pp. 2, 26, 27, 29, 44, 87).

[24] A. Kandala, A. Mezzacapo, K. Temme, M. Takita, M. Brink, J. M. Chow, and J. M. Gambetta: *Hardware-efficient variational quantum eigensolver for small molecules and quantum magnets*, Nature **549**, 242–246 (2017), DOI: 10.1038/nature23879 (cit. on p. 2).

[25] G. M. Church, Y. Gao, and S. Kosuri: *Next-Generation Digital Information Storage in DNA*, Science **337**, 1628–1628 (2012), DOI: 10.1126/science.1226355 (cit. on p. 5).

[26] S. Lloyd: *Universal Quantum Simulators*, Science **273**, 1073–1078 (1996), DOI: 10.1126/science.273.5278.1073 (cit. on p. 6).

[27] F. Bloch: *Nuclear Induction*, Physical Review **70**, 460–474 (1946), DOI: 10.1103/physrev.70.460 (cit. on p. 6).

[28] E. M. L. L. D. Landau, *Mechanics 1*. Elsevier LTD, Oxford, 1995, 224 pp., [Online]. Available: https://www.ebook.de/de/product/3240399/l_d_landau_e_m_lifshitz_mechanics_1.html (cit. on p. 6).

[29] J. J. Sakurai and J. Napolitano, *Modern Quantum Mechanics*. Cambridge University Press, 2017, DOI: 10.1017/9781108499996 (cit. on p. 7).

[30] G. Lindblad: *On the generators of quantum dynamical semigroups*, Communications in Mathematical Physics **48**, 119–130 (1976), DOI: 10.1007/bf01608499 (cit. on p. 8).

[31] C. Brif, R. Chakrabarti, and H. Rabitz, "Control of Quantum Phenomena", *Advances in Chemical Physics*, John Wiley & Sons, Inc., 2011, pp. 1–76, DOI: 10.1002/9781118158715.ch1 (cit. on p. 8).

[32] D. Manzano: *A short introduction to the Lindblad Master Equation*, arXiv, (2019) (cit. on p. 8).

[33] W. A. Phillips: *Tunneling states in amorphous solids*, Journal of Low Temperature Physics **7**, 351–360 (1972), DOI: 10.1007/bf00660072 (cit. on p. 10).

[34] P. W. Anderson, B. I. Halperin, and C. M. Varma: *Anomalous low-temperature thermal properties of glasses and spin glasses*, Philosophical Magazine **25**, 1–9 (1972), DOI: 10.1080/14786437208229210 (cit. on p. 10).

[35] W. A. Phillips: *Two-level states in glasses*, Reports on Progress in Physics **50**, 1657–1708 (1987), DOI: 10.1088/0034-4885/50/12/003 (cit. on pp. 10, 11).

[36] J. M. Martinis, K. B. Cooper, R. McDermott, M. Steffen, M. Ansmann, K. D. Osborn, K. Cicak, S. Oh, D. P. Pappas, R. W. Simmonds, and C. C. Yu: *Decoherence in Josephson Qubits from Dielectric Loss*, Physical Review Letters **95**, (2005), DOI: 10.1103/physrevlett.95.210503 (cit. on pp. 10, 77, 83, 85).

[37] M. B. Weissman: *1fnoise and other slow, nonexponential kinetics in condensed matter*, Reviews of Modern Physics **60**, 537–571 (1988), DOI: 10.1103/revmodphys.60.537 (cit. on p. 12).

[38] A. Shnirman, G. Schön, I. Martin, and Y. Makhlin: *Low- and High-Frequency Noise from Coherent Two-Level Systems*, Physical Review Letters **94**, (2005), DOI: 10.1103/physrevlett.94.127002 (cit. on pp. 12, 13, 77, 86).

[39] G. J. Grabovskij, T. Peichl, J. Lisenfeld, G. Weiss, and A. V. Ustinov: *Strain Tuning of Individual Atomic Tunneling Systems Detected by a Superconducting Qubit*, Science **338**, 232–234 (2012), DOI: 10.1126/science.1226487 (cit. on pp. 13, 77).

[40] J. Lisenfeld, G. J. Grabovskij, C. Müller, J. H. Cole, G. Weiss, and A. V. Ustinov: *Observation of directly interacting coherent two-level systems in an amorphous material*, Nature Communications **6**, 6182 (2015), DOI: 10.1038/ncomms7182 (cit. on pp. 13, 75, 77).

[41] R. Fazio, G. M. Palma, and J. Siewert: *Fidelity and Leakage of Josephson Qubits*, Physical Review Letters **83**, 5385–5388 (1999), DOI: 10.1103/physrevlett.83.5385 (cit. on p. 15).

[42] F. Motzoi, J. M. Gambetta, P. Rebentrost, and F. K. Wilhelm: *Simple Pulses for Elimination of Leakage in Weakly Nonlinear Qubits*, Physical Review Letters **103**, (2009), DOI: 10.1103/physrevlett.103.110501 (cit. on p. 15).

[43] Z. Chen, J. Kelly, C. Quintana, R. Barends, B. Campbell, Y. Chen, B. Chiaro, A. Dunsworth, A. Fowler, E. Lucero, E. Jeffrey, A. Megrant, J. Mutus, M. Neeley, C. Neill, P. O'Malley, P. Roushan, D. Sank, A. Vainsencher, J. Wenner, T. White, A. Korotkov, and J. M. Martinis: *Measuring and Suppressing Quantum State Leakage in a Superconducting Qubit*, Physical Review Letters **116**, (2016), DOI: 10.1103/physrevlett.116.020501 (cit. on p. 15).

[44] R. Roloff, M. Wenin, and W. Pötz: *Optimal Control for Open Quantum Systems: Qubits and Quantum Gates*, Journal of Computational and Theoretical Nanoscience **6**, 1837–1863 (2009), DOI: 10.1166/jctn.2009.1246 (cit. on p. 15).

[45] N. Khaneja, T. Reiss, C. Kehlet, T. Schulte-Herbrüggen, and S. J. Glaser: *Optimal control of coupled spin dynamics: design of NMR pulse sequences by gradient ascent algorithms*, Journal of Magnetic Resonance **172**, 296–305 (2005), DOI: 10.1016/j.jmr.2004.11.004 (cit. on p. 15).

[46] A. Spörl, T. Schulte-Herbrüggen, S. J. Glaser, V. Bergholm, M. J. Storcz, J. Ferber, and F. K. Wilhelm: *Optimal control of coupled Josephson qubits*, Physical Review A **75**, (2007), DOI: 10.1103/physreva.75.012302 (cit. on p. 15).

[47] M. Jerger, A. Kulikov, Z. Vasseli, and A. Fedorov: *In situ characterization of qubit control lines: a qubit as a vector network analyzer*, arXiv, (2017) (cit. on p. 15).

[48] E. L. Hahn: *Spin Echoes*, Physical Review **80**, 580–594 (1950), DOI: 10.1103/physrev.80.580 (cit. on p. 17).

[49] S. Meiboom and D. Gill: *Modified Spin-Echo Method for Measuring Nuclear Relaxation Times*, Review of Scientific Instruments **29**, 688–691 (1958), DOI: 10.1063/1.1716296 (cit. on p. 17).

[50] D. van Delft and P. Kes: *The discovery of superconductivity*, Physics Today **63**, 38–43 (2010), DOI: 10.1063/1.3490499 (cit. on p. 18).

[51] F. Yen, X. Chen, R.-B. Wang, J.-M. Zhu, J. Li, and G.-T. Ma: *Induced Currents in Close-Ended Type-II Superconducting Coils*, IEEE Transactions on Applied Superconductivity **23**, 86–89 (2013), DOI: 10.1109/tasc.2013.2273534 (cit. on p. 18).

[52] S. Sarangi, S. P. Chockalingam, R. G. Mavinkurve, and S. V. Bhat: *Experimental Evidence for Zero DC Resistance of Superconductors*, arXiv, (2005) (cit. on p. 18).

[53] W. Meissner and R. Ochsenfeld: *Ein neuer Effekt bei Eintritt der Supraleitfähigkeit*, Die Naturwissenschaften **21**, 787–788 (1933), DOI: 10.1007/bf01504252 (cit. on p. 18).

[54] A.A.Abrikosov: *The magnetic properties of superconducting alloys*, Journal of Physics and Chemistry of Solids **2**, 199–208 (1957), DOI: 10.1016/0022-3697(57)90083-5 (cit. on p. 18).

[55] J. N. Rjabinin and L. W. Shubnikov: *Magnetic Properties and Critical Currents of Supra-conducting Alloys*, Nature **135**, 581–582 (1935), DOI: 10.1038/135581a0 (cit. on p. 18).

[56] F.London and H.London: *The electromagnetic equations of the supraconductor*, Proceedings of the Royal Society of London. Series A - Mathematical and Physical Sciences **149**, 71–88 (1935), DOI: 10.1098/rspa.1935.0048 (cit. on p. 19).

[57] J. Bardeen, L. N. Cooper, and J. R. Schrieffer: *Microscopic Theory of Superconductivity*, Physical Review **106**, 162–164 (1957), DOI: 10.1103/physrev.106.162 (cit. on pp. 19, 21).

[58] L.P.Gorkov: *Microscopic derivation of the Ginzburg–Landau equations in the theory of superconductivity*, Sov. Phys. - JETP (Engl. Transl.); (United States) **9:6**, (1959) (cit. on p. 19).

[59] C. S. Ludwig Bergmann, *Lehrbuch der Experimentalphysik 6. Festkörper*. Gruyter, Walter de GmbH, 2005, [Online]. Available: https://www.ebook.de/de/product/2517630/ludwig_bergmann_clemens_schaefer_lehrbuch_der_experimentalphysik_6_festkoerper.html (cit. on pp. 20, 21).

[60] M. Tinkham, *Introduction to Superconductivity: v. 1*. Dover Publications Inc., 2004, 480 pp., [Online]. Available: https://www.ebook.de/de/product/3429695/michael_tinkham_introduction_to_superconductivity_v_1.html (cit. on pp. 20, 25).

[61] H. E. Bömmel: *Ultrasonic Attenuation in Superconducting Lead*, Physical Review **96**, 220–221 (1954), DOI: 10.1103/physrev.96.220 (cit. on p. 21).

[62] M. Tinkham: *Spectroscopy of Solids in the Far-Infrared: Studies of superconductors, magnetic materials, and ferroelectrics in this spectral region are rewarding*, Science **145**, 240–247 (1964), DOI: 10.1126/science.145.3629.240 (cit. on p. 21).

[63] C. A. Reynolds, B. Serin, W. H. Wright, and L. B. Nesbitt: *Superconductivity of Isotopes of Mercury*, Physical Review **78**, 487–487 (1950), DOI: 10.1103/physrev.78.487 (cit. on p. 21).

[64] W. A. Little and R. D. Parks: *Observation of Quantum Periodicity in the Transition Temperature of a Superconducting Cylinder*, Physical Review Letters **9**, 9–12 (1962), DOI: 10.1103/physrevlett.9.9 (cit. on p. 22).

[65] R. Doll and M. Näbauer: *Experimental Proof of Magnetic Flux Quantization in a Superconducting Ring*, Physical Review Letters **7**, 51–52 (1961), DOI: 10.1103/physrevlett.7.51 (cit. on p. 22).

[66] B. S. Deaver and W. M. Fairbank: *Experimental Evidence for Quantized Flux in Superconducting Cylinders*, Physical Review Letters **7**, 43–46 (1961), DOI: 10.1103/physrevlett.7.43 (cit. on p. 22).

[67] B.D.Josephson: *Possible new effects in superconductive tunnelling*, Physics Letters **1**, 251–253 (1962), DOI: 10.1016/0031-9163(62)91369-0 (cit. on p. 23).

[68] C.A.Hamilton, F.L.Lloyd, K.Chieh, and W.C.Goeke: *A 10-V Josephson voltage standard*, IEEE Transactions on Instrumentation and Measurement **38**, 314–316 (1989), DOI: 10.1109/19.192296 (cit. on p. 24).

[69] D. E. McCumber: *Tunneling and Weak-Link Superconductor Phenomena Having Potential Device Applications*, Journal of Applied Physics **39**, 2503–2508 (1968), DOI: 10.1063/1.1656597 (cit. on p. 25).

[70] D. P. DiVincenzo: *Topics in Quantum Computers*, arXiv, (1996) (cit. on p. 26).

[71] D. G. Cory, A. F. Fahmy, and T. F. Havel: *Ensemble quantum computing by NMR spectroscopy*, Proceedings of the National Academy of Sciences **94**, 1634–1639 (1997), DOI: 10.1073/pnas.94.5.1634 (cit. on p. 26).

[72] J. L. O'Brien: *Optical Quantum Computing*, Science **318**, 1567–1570 (2007), DOI: 10.1126/science.1142892 (cit. on p. 26).

[73] N. Friis, O. Marty, C. Maier, C. Hempel, M. Holzäpfel, P. Jurcevic, M. B. Plenio, M. Huber, C. Roos, R. Blatt, and B. Lanyon: *Observation of Entangled States of a Fully Controlled 20-Qubit System*, Physical Review X **8**, (2018), DOI: 10.1103/physrevx.8.021012 (cit. on p. 26).

[74] D. Kielpinski, C. Monroe, and D. J. Wineland: *Architecture for a large-scale ion-trap quantum computer*, Nature **417**, 709–711 (2002), DOI: 10.1038/nature00784 (cit. on p. 26).

[75] Y. Wang, M. Um, J. Zhang, S. An, M. Lyu, J.-N. Zhang, L.-M. Duan, D. Yum, and K. Kim: *Single-qubit quantum memory exceeding ten-minute coherence time*, Nature Photonics **11**, 646–650 (2017), DOI: 10.1038/s41566-017-0007-1 (cit. on p. 26).

[76] J. J. L. Morton, A. M. Tyryshkin, R. M. Brown, S. Shankar, B. W. Lovett, A. Ardavan, T. Schenkel, E. E. Haller, J. W. Ager, and S. A. Lyon: *Solid-state quantum memory using the 31P nuclear spin*, Nature **455**, 1085–1088 (2008), DOI: 10.1038/nature07295 (cit. on p. 26).

[77] D. D. Awschalom, R. Hanson, J. Wrachtrup, and B. B. Zhou: *Quantum technologies with optically interfaced solid-state spins*, Nature Photonics **12**, 516–527 (2018), DOI: 10.1038/s41566-018-0232-2 (cit. on p. 26).

[78] E. D. Herbschleb, H. Kato, Y. Maruyama, T. Danjo, T. Makino, S. Yamasaki, I. Ohki, K. Hayashi, H. Morishita, M. Fujiwara, and N. Mizuochi: *Ultra-long coherence times amongst room-temperature solid-state spins*, Nature Communications **10**, (2019), DOI: 10.1038/s41467-019-11776-8 (cit. on p. 26).

[79] V. Bouchiat, D. Vion, P. Joyez, D. Esteve, and M. H. Devoret: *Quantum Coherence with a Single Cooper Pair*, Physica Scripta **T76**, 165 (1998), DOI: 10.1238/physica.topical.076a00165 (cit. on p. 26).

[80] P. A. M. Dirac: *The Quantum Theory of the Emission and Absorption of Radiation*, Proceedings of the Royal Society A: Mathematical, Physical and Engineering Sciences **114**, 243–265 (1927), DOI: 10.1098/rspa.1927.0039 (cit. on p. 27).

[81] D. V. Averin and K. K. Likharev: *Coulomb blockade of single-electron tunneling, and coherent oscillations in small tunnel junctions*, Journal of Low Temperature Physics **62**, 345–373 (1986), DOI: 10.1007/bf00683469 (cit. on p. 28).

[82] M. H. Devoret, A. Wallraff, and J. M. Martinis: *Superconducting Qubits: A Short Review*, arXiv, (2004) (cit. on p. 28).

[83] H. Meissner: *Superconductivity of Contacts with Interposed Barriers*, Physical Review **117**, 672–680 (1960), DOI: 10.1103/physrev.117.672 (cit. on pp. 30, 49).

[84] P.G.DeGennes: *Boundary Effects in Superconductors*, Reviews of Modern Physics **36**, 225–237 (1964), DOI: 10.1103/revmodphys.36.225 (cit. on p. 30).

[85] T. Nishino, E. Yamada, and U. Kawabe: *Carrier-concentration dependence of critical superconducting current induced by the proximity effect in silicon*, Physical Review B **33**, 2042–2045 (1986), DOI: 10.1103/physrevb.33.2042 (cit. on p. 30).

[86] Y.-J. Doh, J. A. van Dam, A. L. Roest, E. P. A. M. Bakkers, L. P. Kouwenhoven, and S. De Franceschi: *Tunable Supercurrent Through Semiconductor Nanowires*, Science **309**, 272–275 (2005), DOI: 10.1126/science.1113523 (cit. on pp. 30, 49).

[87] L. Casparis, T. Larsen, M. Olsen, F. Kuemmeth, P. Krogstrup, J. Nygård, K. Petersson, and C. Marcus: *Gatemon Benchmarking and Two-Qubit Operations*, Physical Review Letters **116**, (2016), DOI: 10.1103/physrevlett.116.150505 (cit. on pp. 30, 52).

[88] C.-T. Sah, *Fundamentals Of Solid State Electronics*. World Scientific Publishing Co Pte Ltd, 1991, 1040 pp., [Online]. Available: https://www.ebook.de/de/product/3737802/chih_tang_sah_fundamentals_of_solid_state_electronics.html (cit. on p. 31).

[89] T. Larsen, K. Petersson, F. Kuemmeth, T. Jespersen, P. Krogstrup, J. Nygård, and C. Marcus: *Semiconductor-Nanowire-Based Superconducting Qubit*, Physical Review Letters **115**, (2015), DOI: 10.1103/physrevlett.115.127001 (cit. on pp. 31, 52).

[90] L. Casparis, M. R. Connolly, M. Kjaergaard, N. J. Pearson, A. Kringhøj, T. W. Larsen, F. Kuemmeth, T. Wang, C. Thomas, S. Gronin, G. C. Gardner, M. J. Manfra, C. M. Marcus, and K. D. Petersson: *Superconducting gatemon qubit based on a proximitized two-dimensional electron gas*, Nature Nanotechnology **13**, 915–919 (2018), DOI: 10.1038/s41565-018-0207-y (cit. on p. 31).

[91] D. Gottesman: *An Introduction to Quantum Error Correction and Fault-Tolerant Quantum Computation*, (2009) (cit. on p. 33).

[92] E. A. Sete, J. M. Martinis, and A. N. Korotkov: *Quantum theory of a bandpass Purcell filter for qubit readout*, Physical Review A **92**, (2015), DOI: 10.1103/physreva.92.012325 (cit. on p. 33).

[93] H. Hertz: *Ueber sehr schnelle electrische Schwingungen*, Annalen der Physik und Chemie **267**, 421–448 (1887), DOI: 10.1002/andp.18872670707 (cit. on p. 33).

[94] D. M. Pozar, *Microwave Engineering*. John Wiley and Sons Ltd, 2011, 752 pp., [Online]. Available: https://www.ebook.de/de/product/14948033/david_m_pozar_microwave_engineering.html (cit. on pp. 34, 36, 37).

[95] Simons, *Coplanar Waveguide Circuits*. John Wiley & Sons, 2001, 464 pp., [Online]. Available: https://www.ebook.de/de/product/3601709/simons_coplanar_waveguide_circuits.html (cit. on p. 36).

[96] R. Corporation, *Ceramic thermoset microwave material datasheet*, [Online]. Available: https://www.rogerscorp.com/documents/728/acs/TMM-Thermoset-Laminate-Data-Sheet-TMM3-TMM4-TMM6-TMM10-TMM10i-TMM13i.pdf (cit. on p. 36).

[97] J. M. Raimond, M. Brune, and S. Haroche: *Manipulating quantum entanglement with atoms and photons in a cavity*, Reviews of Modern Physics **73**, 565–582 (2001), DOI: 10.1103/revmodphys.73.565 (cit. on p. 39).

[98] A. Blais, R.-S. Huang, A. Wallraff, S. M. Girvin, and R. J. Schoelkopf: *Cavity quantum electrodynamics for superconducting electrical circuits: An architecture for quantum computation*, Physical Review A **69**, (2004), DOI: 10.1103/physreva.69.062320 (cit. on pp. 39–42).

[99] A.Wallraff, D.I.Schuster, A.Blais, L.Frunzio, R.-S.Huang, J.Majer, S.Kumar, S.M.Girvin, and R.J.Schoelkopf: *Strong coupling of a single photon to a superconducting qubit using circuit quantum electrodynamics*, Nature **431**, 162–167 (2004), DOI: 10.1038/nature02851 (cit. on p. 39).

[100] S.Haroche and J.M.Raimond, "Radiative Properties of Rydberg States in Resonant Cavities", *Advances in Atomic and Molecular Physics*, Elsevier, 1985, pp. 347–411, DOI: 10.1016/s0065-2199(08)60271-7 (cit. on p. 39).

[101] S. Haroche: *Nobel Lecture: Controlling photons in a box and exploring the quantum to classical boundary*, Reviews of Modern Physics **85**, 1083–1102 (2013), DOI: 10.1103/revmodphys.85.1083 (cit. on p. 39).

[102] S. Marlan O. Scully Muhammad Suhail Zubairy, *Quantum Optics*. Cambridge University Press, 2010, 656 pp., [Online]. Available: https://www.ebook.de/de/product/3303733/marlan_o_scully_muhammad_suhail_zubairy_scully_quantum_optics.html (cit. on p. 40).

[103] E.T.Jaynes and F.W.Cummings: *Comparison of quantum and semiclassical radiation theories with application to the beam maser*, Proceedings of the IEEE **51**, 89–109 (1963), DOI: 10.1109/proc.1963.1664 (cit. on p. 40).

[104] D. Schuster, PhD thesis, Yale University, 2007 (cit. on p. 42).

[105] M. S. Khalil, M. J. A. Stoutimore, F. C. Wellstood, and K. D. Osborn: *An analysis method for asymmetric resonator transmission applied to superconducting devices*, Journal of Applied Physics **111**, 054510 (2012), DOI: 10.1063/1.3692073 (cit. on p. 43).

[106] J. Gambetta, A. Blais, M. Boissonneault, A. A. Houck, D. I. Schuster, and S. M. Girvin: *Quantum trajectory approach to circuit QED: Quantum jumps and the Zeno effect*, Physical Review A **77**, (2008), DOI: 10.1103/physreva.77.012112 (cit. on pp. 43, 44).

[107] B. D'Anjou and G. Burkard: *Optimal Dispersive Readout of a Spin Qubit with a Microwave Cavity*, (2019) (cit. on p. 43).

[108] V. B. Braginsky and F. Y. Khalili: *Quantum nondemolition measurements: the route from toys to tools*, Reviews of Modern Physics **68**, 1–11 (1996), DOI: 10.1103/revmodphys.68.1 (cit. on p. 44).

[109] J. Gambetta, W. A. Braff, A. Wallraff, S. M. Girvin, and R. J. Schoelkopf: *Protocols for optimal readout of qubits using a continuous quantum nondemolition measurement*, Physical Review A **76**, (2007), DOI: 10.1103/physreva.76.012325 (cit. on p. 44).

[110] B. Misra and E. C. G. Sudarshan: *The Zeno's paradox in quantum theory*, Journal of Mathematical Physics **18**, 756–763 (1977), DOI: 10.1063/1.523304 (cit. on p. 44).

[111] U. Vool, I. Pop, K. Sliwa, B. Abdo, C. Wang, T. Brecht, Y. Gao, S. Shankar, M. Hatridge, G. Catelani, M. Mirrahimi, L. Frunzio, R. Schoelkopf, L. Glazman, and M. Devoret: *Non-Poissonian Quantum Jumps of a Fluxonium Qubit due to Quasiparticle Excitations*, Physical Review Letters **113**, (2014), DOI: 10.1103/physrevlett.113.247001 (cit. on p. 44).

[112] P. Winkel, I. Takmakov, D. Rieger, L. Planat, W. Hasch-Guichard, L. Grünhaupt, N. Maleeva, F. Foroughi, F. Henriques, K. Borisov, J. Ferrero, A. V. Ustinov, W. Wernsdorfer, N. Roch, and I. M. Pop: *Non-degenerate parametric amplifiers based on dispersion engineered Josephson junction arrays*, arXiv, (2019) (cit. on p. 44).

[113] E. M.Purcell: *Spontaneous Emission Probabilities at Radio Frequencies*, Physical Review **69**, 674–674 (1946), DOI: 10.1103/physrev.69.674 (cit. on p. 44).

[114] D. Kleppner: *Inhibited Spontaneous Emission*, Physical Review Letters **47**, 233–236 (1981), DOI: 10.1103/physrevlett.47.233 (cit. on p. 44).

[115] V. W. Schottky, "Abweichungen vom Ohmschen Gesetz in Halbleitern", *Perspectives in Condensed Matter Physics*, Springer Netherlands, 1940, pp. 59–62, DOI: 10.1007/978-94-009-0657-0_6 (cit. on p. 47).

[116] W. Shockley: *On the Surface States Associated with a Periodic Potential*, Physical Review **56**, 317–323 (1939), DOI: 10.1103/physrev.56.317 (cit. on p. 48).

[117] C. Kittel, *Introduction to solid state physics*. Wiley, 1971 (cit. on p. 48).

[118] L. Ö. Olsson, C. B. M. Andersson, M. C. Håkansson, J. Kanski, L. Ilver, and U. O. Karlsson: *Charge Accumulation at InAs Surfaces*, Physical Review Letters **76**, 3626–3629 (1996), DOI: 10.1103/physrevlett.76.3626 (cit. on p. 49).

[119] G. de Lange, B. van Heck, A. Bruno, D. J. van Woerkom, A. Geresdi, S. R. Plissard, E. P. A. M. Bakkers, A. R. Akhmerov, and L. DiCarlo: *Realization of Microwave Quantum Circuits Using Hybrid Superconducting-Semiconducting Nanowire Josephson Elements*, Phys. Rev. Lett. **115**, 127002 (2015), DOI: 10.1103/PhysRevLett.115.127002 (cit. on p. 49).

[120] J. Knoch, J. Appenzeller, and B. Lengeler: *Preparation of highly transparent superconductor-semiconductor contacts*, Journal of Applied Physics **88**, 3522–3526 (2000), DOI: 10.1063/1.1288504 (cit. on p. 49).

[121] P.Krogstrup, N.L.B.Ziino, W.Chang, S.M.Albrecht, M.H.Madsen, E.Johnson, J.Nygård, C.M.Marcus, and T.S.Jespersen: *Epitaxy of semiconductor–superconductor nanowires*, Nature Materials **14**, 400–406 (2015), DOI: 10.1038/nmat4176 (cit. on p. 49).

[122] R. Holm and W. Meissner: *Messungen mit Hilfe von flüssigem Helium*, Zeitschrift für Physik **74**, 715–735 (1932), DOI: 10.1007/bf01340420 (cit. on p. 49).

[123] A. Furusaki: *Josephson current carried by Andreev levels in superconducting quantum point contacts*, Superlattices and Microstructures **25**, 809–818 (1999), DOI: 10.1006/spmi.1999.0730 (cit. on pp. 49, 50).

[124] C. W. J. Beenakker, "Three "Universal" Mesoscopic Josephson Effects", *Springer Series in Solid-State Sciences*, Springer Berlin Heidelberg, 1992, pp. 235–253, DOI: 10.1007/978-3-642-84818-6_22 (cit. on pp. 49, 50).

[125] G. E. Blonder, M. Tinkham, and T. M. Klapwijk: *Transition from metallic to tunneling regimes in superconducting microconstrictions: Excess current, charge imbalance, and supercurrent conversion*, Physical Review B **25**, 4515–4532 (1982), DOI: 10.1103/physrevb.25.4515 (cit. on p. 50).

[126] T. Schäpers, *Superconductor/Semiconductor Junctions*. Springer Berlin Heidelberg, 2001, DOI: 10.1007/3-540-45525-6 (cit. on p. 50).

[127] V. Ambegaokar and A. Baratoff: *Tunneling Between Superconductors*, Physical Review Letters **10**, 486–489 (1963), DOI: 10.1103/physrevlett.10.486 (cit. on p. 51).

[128] L. Bretheau, J. I.-J. Wang, R. Pisoni, K. Watanabe, T. Taniguchi, and P. Jarillo-Herrero: *Tunnelling spectroscopy of Andreev states in graphene*, Nature Physics **13**, 756–760 (2017), DOI: 10.1038/nphys4110 (cit. on p. 52).

[129] F. Luthi, T. Stavenga, O. Enzing, A. Bruno, C. Dickel, N. Langford, M. Rol, T. Jespersen, J. Nygård, P. Krogstrup, and L. DiCarlo: *Evolution of Nanowire Transmon Qubits and Their Coherence in a Magnetic Field*, Physical Review Letters **120**, (2018), DOI: 10.1103/physrevlett.120.100502 (cit. on p. 52).

[130] Y. Xia, P. Yang, Y. Sun, Y. Wu, B. Mayers, B. Gates, Y. Yin, F. Kim, and H. Yan: *One-Dimensional Nanostructures: Synthesis, Characterization, and Applications*, Advanced Materials **15**, 353–389 (2003), DOI: 10.1002/adma.200390087 (cit. on p. 52).

[131] K. Mølhave, T. Wich, A. Kortschack, and P. Bøggild: *Pick-and-place nanomanipulation using microfabricated grippers*, Nanotechnology **17**, 2434–2441 (2006), DOI: 10.1088/0957-4484/17/10/002 (cit. on p. 53).

[132] P.Zellekens, *Towards Semiconductor-Superconductor hybrid quantum circuits: Gatemon and Andreev qubits based on InAs/Al and GaAs/InSb core/shell nanowires (in preparation)*, PhD thesis, Forschungszentrum Juelich (FZJ), 2020 (cit. on pp. 55, 68).

[133] H. Nyquist: *Thermal Agitation of Electric Charge in Conductors*, Physical Review **32**, 110–113 (1928), DOI: 10.1103/physrev.32.110 (cit. on p. 60).

[134] G. Czycholl, *Theoretische Festkörperphysik*. Springer Berlin Heidelberg, 2008, DOI: 10.1007/978-3-540-74790-1 (cit. on p. 62).

[135] S. Krinner, S. Storz, P. Kurpiers, P. Magnard, J. Heinsoo, R. Keller, J. Lütolf, C. Eichler, and A. Wallraff: *Engineering cryogenic setups for 100-qubit scale superconducting circuit systems*, EPJ Quantum Technology **6**, (2019), DOI: 10.1140/epjqt/s40507-019-0072-0 (cit. on p. 62).

[136] H. Friis: *Noise Figures of Radio Receivers*, Proceedings of the IRE **32**, 419–422 (1944), DOI: 10.1109/jrproc.1944.232049 (cit. on p. 62).

[137] A. Roy and M. Devoret: *Introduction to parametric amplification of quantum signals with Josephson circuits*, Comptes Rendus Physique **17**, 740–755 (2016), DOI: 10.1016/j.crhy.2016.07.012 (cit. on p. 62).

[138] D. Allan: *Statistics of atomic frequency standards*, Proceedings of the IEEE **54**, 221–230 (1966), DOI: 10.1109/proc.1966.4634 (cit. on p. 67).

[139] S. S. Inc., *3D Planar High-Frequency Electromagnetic Software Version 16.5*, [Online]. Available: http://www.sonnetsoftware.com (cit. on p. 70).

[140] D. Systèmes, *CST Studio Suite - Electromagnetic field simulation software ver. 12*, [Online]. Available: https://www.3ds.com/products-services/simulia/products/cst-studio-suite (cit. on p. 73).

[141] K. Fujisawa: *General Treatment of Klystron Resonant Cavities*, IEEE Transactions on Microwave Theory and Techniques **6**, 344–358 (1958), DOI: 10.1109/tmtt.1958.1125205 (cit. on p. 73).

[142] S. P. Software, *Solid Edge ST8 - 3D CAD, ver.8-2015*, [Online]. Available: https://solidedge.siemens.com (cit. on p. 74).

[143] Luxion, *KeyShot Standalone Renderer ver. 8.2*, [Online]. Available: https://www.keyshot.com/ (cit. on p. 74).

[144] L. Faoro and L. B. Ioffe: *Interacting tunneling model for two-level systems in amorphous materials and its predictions for their dephasing and noise in superconducting microresonators*, Physical Review B **91**, (2015), DOI: 10.1103/physrevb.91.014201 (cit. on p. 75).

[145] C. Müller, J. Lisenfeld, A. Shnirman, and S. Poletto: *Interacting two-level defects as sources of fluctuating high-frequency noise in superconducting circuits*, Physical Review B **92**, (2015), DOI: 10.1103/physrevb.92.035442 (cit. on pp. 75, 77).

[146] S. M. Meißner, A. Seiler, J. Lisenfeld, A. V. Ustinov, and G. Weiss: *Probing individual tunneling fluctuators with coherently controlled tunneling systems*, Physical Review B **97**, (2018), DOI: 10.1103/physrevb.97.180505 (cit. on p. 76).

[147] J. L. Black and B. I. Halperin: *Spectral Diffusion, Phonon Echoes, and Saturation Recovery in Glasses at Low-Temperatures*, Physical Review B **16**, 2879–2895 (1977) (cit. on p. 77).

[148] L. Faoro and L. B. Ioffe: *Internal Loss of Superconducting Resonators Induced by Interacting Two-Level Systems*, Physical Review Letters **109**, 157005 (2012), DOI: 10.1103/PhysRevLett.109.157005 (cit. on p. 77).

[149] M. Steffen, M. Ansmann, R. McDermott, N. Katz, R. Bialczak, E. Lucero, M. Neeley, E. Weig, a. Cleland, and J. Martinis: *State Tomography of Capacitively Shunted Phase Qubits with High Fidelity*, Physical Review Letters **97**, 050502 (2006), DOI: 10.1103/PhysRevLett.97.050502 (cit. on p. 77).

[150] C. Wang, C. Axline, Y. Y. Gao, T. Brecht, Y. Chu, L. Frunzio, M. H. Devoret, and R. J. Schoelkopf: *Surface participation and dielectric loss in superconducting qubits*, Appl. Phys. Lett. **107**, (2015) (cit. on p. 77).

[151] J. H. Cole, C. Müller, P. Bushev, G. J. Grabovskij, J. Lisenfeld, A. Lukashenko, A. V. Ustinov, and A. Shnirman: *Quantitative evaluation of defect-models in superconducting phase qubits*, Applied Physics Letters **97**, 252501 (2010), DOI: 10.1063/1.3529457 (cit. on p. 77).

[152] B. Sarabi, A. Ramanayaka, A. Burin, F. Wellstood, and K. Osborn: *Projected Dipole Moments of Individual Two-Level Defects Extracted Using Circuit Quantum Electrodynamics*, Physical Review Letters **116**, (2016), DOI: 10.1103/physrevlett.116.167002 (cit. on pp. 77, 83).

[153] J. D. Brehm, A. Bilmes, G. Weiss, A. V. Ustinov, and J. Lisenfeld: *Transmission-line resonators for the study of individual two-level tunneling systems*, Applied Physics Letters **111**, 112601 (2017), DOI: 10.1063/1.5001920 (cit. on pp. 77, 83).

[154] J. Lisenfeld, A. Bilmes, S. Matityahu, S. Zanker, M. Marthaler, M. Schechter, G. Schön, A. Shnirman, G. Weiss, and A. V. Ustinov: *Decoherence spectroscopy with individual two-level tunneling defects*, Scientific Reports **6**, (2016), DOI: 10.1038/srep23786 (cit. on pp. 77, 80, 83).

[155] Y. Shalibo, Y. Rofe, D. Shwa, F. Zeides, M. Neeley, J. M. Martinis, and N. Katz: *Lifetime and Coherence of Two-Level Defects in a Josephson Junction*, Physical Review Letters **105**, (2010), DOI: 10.1103/physrevlett.105.177001 (cit. on p. 80).

[156] H. Wang, M. Hofheinz, J. Wenner, M. Ansmann, R. C. Bialczak, M. Lenander, E. Lucero, M. Neeley, A. D. O'Connell, D. Sank, M. Weides, A. N. Cleland, and J. M. Martinis: *Improving the coherence time of superconducting coplanar resonators*, Applied Physics Letters **95**, 233508 (2009), DOI: 10.1063/1.3273372 (cit. on p. 80).

[157] J. B. Chang, M. R. Vissers, A. D. Córcoles, M. Sandberg, J. Gao, D. W. Abraham, J. M. Chow, J. M. Gambetta, M. B. Rothwell, G. A. Keefe, M. Steffen, and D. P. Pappas: *Improved superconducting qubit coherence using titanium nitride*, Applied Physics Letters **103**, 012602 (2013), DOI: 10.1063/1.4813269 (cit. on p. 80).

[158] G. Calusine, A. Melville, W. Woods, R. Das, C. Stull, V. Bolkhovsky, D. Braje, D. Hover, D. K. Kim, X. Miloshi, D. Rosenberg, A. Sevi, J. L. Yoder, E. Dauler, and W. D. Oliver: *Analysis and mitigation of interface losses in trenched superconducting coplanar waveguide resonators*, Applied Physics Letters **112**, 062601 (2018), DOI: 10.1063/1.5006888 (cit. on pp. 80, 84).

[159] D. H. Slichter and C. Müller and R. Vijay and S. J. Weber and A. Blais and I. Siddiqi: *Quantum Zeno effect in the strong measurement regime of circuit quantum electrodynamics*, New Journal of Physics **18**, 053031 (2016), DOI: 10.1088/1367-2630/18/5/053031 (cit. on p. 81).

[160] O. Asban, A. Amir, Y. Imry, and M. Schechter: *Effect of interactions and disorder on the relaxation of two-level systems in amorphous solids*, Physical Review B **95**, (2017), DOI: 10.1103/physrevb.95.144207 (cit. on p. 83).

[161] L. J. Zeng, S. Nik, T. Greibe, P. Krantz, C. M. Wilson, P. Delsing, and E. Olsson: *Direct observation of the thickness distribution of ultra thin AlOxbarriers in Al/AlOx/Al Josephson junctions*, Journal of Physics D: Applied Physics **48**, 395308 (2015), DOI: 10.1088/0022-3727/48/39/395308 (cit. on p. 83).

[162] A. Bilmes, PhD thesis, Karlsruher Instituts für Technologie (KIT), 2019 (cit. on pp. 84, 85).

[163] C. Neill, A. Megrant, R. Barends, Y. Chen, B. Chiaro, J. Kelly, J. Y. Mutus, P. J. J. O'Malley, D. Sank, J. Wenner, T. C. White, Y. Yin, A. N. Cleland, and J. M. Martinis: *Fluctuations from edge defects in superconducting resonators*, Applied Physics Letters **103**, 072601 (2013), DOI: 10.1063/1.4818710 (cit. on p. 84).

[164] I. ANSYS, *Electromagnetic finite element analysis software ver. 2015.2*, [Online]. Available: https://www.ansys.com/products/electronics/ansys-maxwell (cit. on p. 85).

[165] J. Lisenfeld, A. Bilmes, A. Megrant, R. Barends, J. Kelly, P. Klimov, G. Weiss, J. M. Martinis, and A. V. Ustinov: *Electric field spectroscopy of material defects in transmon qubits*, (2019) (cit. on p. 85).

[166] D. Gunnarsson, J.-M. Pirkkalainen, J. Li, G. S. Paraoanu, P. Hakonen, M. Sillanpää, and M. Prunnila: *Dielectric losses in multi-layer Josephson junction qubits*, Superconductor Science and Technology **26**, 085010 (2013), DOI: 10.1088/0953-2048/26/8/085010 (cit. on p. 85).

[167] M. S. Khalil, S. Gladchenko, M. J. A. Stoutimore, F. C. Wellstood, A. L. Burin, and K. D. Osborn: *Landau-Zener population control and dipole measurement of a two-level-system bath*, Physical Review B **90**, (2014), DOI: 10.1103/physrevb.90.100201 (cit. on p. 85).

[168] P. Dutta and P. M. Horn: *Low-frequency fluctuations in solids:1/fnoise*, Reviews of Modern Physics **53**, 497–516 (1981), DOI: 10.1103/revmodphys.53.497 (cit. on p. 86).

[169] P. Welch: *The use of fast Fourier transform for the estimation of power spectra: A method based on time averaging over short, modified periodograms*, IEEE Transactions on Audio and Electroacoustics **15**, 70–73 (1967), DOI: 10.1109/tau.1967.1161901 (cit. on p. 87).

[170] F. J. Harris: *On the use of windows for harmonic analysis with the discrete Fourier transform*, Proceedings of the IEEE **66**, 51–83 (1978), DOI: 10.1109/proc.1978.10837 (cit. on p. 87).

[171] G. Catelani: *Parity switching and decoherence by quasiparticles in single-junction transmons*, Physical Review B **89**, (2014), DOI: 10.1103/physrevb.89.094522 (cit. on p. 87).

[172] D. Ristè, C. C. Bultink, M. J. Tiggelman, R. N. Schouten, K. W. Lehnert, and L. DiCarlo: *Millisecond charge-parity fluctuations and induced decoherence in a superconducting transmon qubit*, Nature Communications **4**, 1913 (2013), DOI: 10.1038/ncomms2936 (cit. on p. 87).

[173] S. Gustavsson, F. Yan, G. Catelani, J. Bylander, A. Kamal, J. Birenbaum, D. Hover, D. Rosenberg, G. Samach, A. P. Sears, S. J. Weber, J. L. Yoder, J. Clarke, A. J. Kerman, F. Yoshihara, Y. Nakamura, T. P. Orlando, and W. D. Oliver: *Suppressing relaxation in superconducting qubits by quasiparticle pumping*, Science **354**, 1573–1577 (2016), DOI: 10.1126/science.aah5844 (cit. on p. 87).

[174] A. Schneider, T. Wolz, M. Pfirrmann, M. Spiecker, H. Rotzinger, A. V. Ustinov, and M. Weides: *Transmon qubit in a magnetic field: Evolution of coherence and transition frequency*, Physical Review Research **1**, (2019), DOI: 10.1103/physrevresearch.1.023003 (cit. on p. 88).

[175] P. Kumar, S. Sendelbach, M. Beck, J. Freeland, Z. Wang, H. Wang, C. C. Yu, R. Wu, D. Pappas, and R. McDermott: *Origin and Reduction of 1/f Magnetic Flux Noise in Superconducting Devices*, Physical Review Applied **6**, (2016), DOI: 10.1103/physrevapplied.6.041001 (cit. on p. 88).

[176] S. M. Anton, C. D. Nugroho, J. S. Birenbaum, S. R. O'Kelley, V. Orlyanchik, A. F. Dove, G. A. Olson, Z. R. Yoscovits, J. N. Eckstein, D. J. V. Harlingen, and J. Clarke: *Low-frequency critical current noise in Josephson junctions induced by temperature fluctuations*, Applied Physics Letters **101**, 092601 (2012), DOI: 10.1063/1.4749282 (cit. on p. 88).

[177] T. Akazaki, H. Takayanagi, J. Nitta, and T. Enoki: *A Josephson field effect transistor using an InAs-inserted-channel In0.52Al0.48As/In0.53Ga0.47As inverted modulation-doped structure*, Applied Physics Letters **68**, 418–420 (1996), DOI: 10.1063/1.116704 (cit. on p. 93).

[178] G. D. Simoni, F. Paolucci, C. Puglia, and F. Giazotto: *Josephson Field-Effect Transistors Based on All-Metallic Al/Cu/Al Proximity Nanojunctions*, ACS Nano **13**, 7871–7876 (2019), DOI: 10.1021/acsnano.9b02209 (cit. on p. 93).

[179] G. Ithier, E. Collin, P. Joyez, P. J. Meeson, D. Vion, D. Esteve, F. Chiarello, A. Shnirman, Y. Makhlin, J. Schriefl, and G. Schön: *Decoherence in a superconducting quantum bit circuit*, Physical Review B **72**, (2005), DOI: 10.1103/physrevb.72.134519 (cit. on p. 104).

[180] J. Braumüller, J. Cramer, S. Schlör, H. Rotzinger, L. Radtke, A. Lukashenko, P. Yang, S. T. Skacel, S. Probst, M. Marthaler, L. Guo, A. V. Ustinov, and M. Weides: *Multiphoton dressing of an anharmonic superconducting many-level quantum circuit*, Physical Review B **91**, (2015), DOI: 10.1103/physrevb.91.054523 (cit. on p. 105).

List of Publications

1. **S. Schlör**, J. Lisenfeld, C. Müller, A. Bilmes, A. Schneider, D. P. Pappas, A. V. Ustinov, and M. Weides: *Correlating Decoherence in Transmon Qubits: Low Frequency Noise by Single Fluctuators*, Physical Review Letters **123**, (2019), DOI: 10.1103/physrevlett.123.190502.
2. L. Grünhaupt, U. von Lüpke, D. Gusenkova, S. T. Skacel, N. Maleeva, **S. Schlör**, A. Bilmes, H. Rotzinger, A. V. Ustinov, M. Weides, and I. M. Pop: *An argon ion beam milling process for native AlOx layers enabling coherent superconducting contacts*, Applied Physics Letters **111**, 072601 (2017), DOI: 10.1063/1.4990491.
3. J. Braumüller, M. Sandberg, M. R. Vissers, A. Schneider, **S. Schlör**, L. Grünhaupt, H. Rotzinger, M. Marthaler, A. Lukashenko, A. Dieter, A. V. Ustinov, M. Weides, and D. P. Pappas: *Concentric transmon qubit featuring fast tunability and an anisotropic magnetic dipole moment*, Applied Physics Letters **108**, 032601 (2016), DOI: 10.1063/1.4940230.
4. J. Braumüller, J. Cramer, **S. Schlör**, H. Rotzinger, L. Radtke, A. Lukashenko, P. Yang, S. T. Skacel, S. Probst, M. Marthaler, L. Guo, A. V. Ustinov, and M. Weides: *Multiphoton dressing of an anharmonic superconducting many-level quantum circuit*, Physical Review B **91**, (2015), DOI: 10.1103/physrevb.91.054523.
5. T. Beck, **S. Schloer**, T. Grossmann, T. Mappes, and H. Kalt: *Flexible coupling of high-Q goblet resonators for formation of tunable photonic molecules*, Optics Express **20**, 22012 (2012), DOI: 10.1364/oe.20.022012.